DISSERTATION

CHARACTERIZATION OF THE COMBUSTION PROCESS OF LIQUIFIED PETROLEUM GAS AND DIMETHYL ETHER BLENDS FOR USE IN SPARK IGNITED INTERNAL COMBUSTION ENGINES

Submitted by

Reece Alan Churchill

Department of Mechanical Engineering

In partial fulfillment of the requirements

For the Degree of Doctor of Philosophy

Colorado State University

Fort Collins, Colorado

Spring 2026

Doctoral Committee:

Advisor: Bret C. Windom

Daniel B. Olsen
Jeremey Daily
Dan Wise

ABSTRACT

CHARACTERIZATION OF THE COMBUSTION PROPERTIES OF LIQUIFIED PETROLEUM GAS AND DIMETHYL ETHER BLENDS FOR USE IN SPARK IGNITED INTERNAL COMBUSTION ENGINES

To meet the increasing demand for carbon intensity reduction in the heavy-duty transportation sector, this dissertation investigates the development of high-efficiency combustion strategies utilizing both liquefied petroleum gas (LPG) and renewable dimethyl ether (rDME). LPG serves as a viable alternative fuel primarily due to its ability to reduce emissions and its favorable physical and chemical properties, which allow for efficient transport and storage in a liquid state at moderate pressures. The research begins by establishing a numerical foundation for baseline LPG combustion, utilizing an extreme flash KH-RT spray model coupled with the ALPINE 153 chemical kinetic mechanism. This framework was validated against experimental High Pressure Spray Chamber (HPSC) data using Schlieren and Mie-scattering imaging techniques to ensure the phase change and flash-boiling plume expansion of LPG were resolved before moving to engine scale simulations. With the spray physics validated, a numerical investigation into mixture formation for pure LPG was conducted to characterize the fluid dynamic drivers of stable Direct Injection (DI) operation compared to Port Fuel Injection (PFI) benchmarks. These 3D CFD studies identified that Direct Injection LPG operation is exclusively sensitive to Start of Injection (SOI) timing due to in-cylinder charge cooling and turbulent decay. Specifically, the work identified that a late-cycle recovery of Turbulent Kinetic Energy (TKE) at SOI 120° bTDC provides the necessary aerodynamic shear to overcome reduced residence times, identifying

the piston-top velocity profile as a potential universal design parameter for stable DI operation across varying compression ratios. To further reduce the carbon intensity of LPG operation, this work explores the potential of blending LPG with more reactive, renewably produced fuels such as DME. The inherently high MON and RON of LPG allow it to be utilized in higher compression ratio engines due to its strong resistance to autoignition compared to traditional petroleum fuels. This characteristic places LPG in a unique position where it can be blended with highly reactive fuels while maintaining favorable and controllable combustion. Utilizing rDME blends leverages LPG's favorable combustion properties to reduce carbon intensity on two fronts, through tailpipe emissions and cleaner fuel production. To understand the properties of these novel LPG/DME blends, octane characterization was experimentally determined using a modified Cooperative Fuels Research (CFR) engine. This testing identified a non-linear promoting effect of rDME on autoignition and established a 30% DME blend as a viable 89-octane gasoline surrogate. Additionally, high-speed Schlieren spray imaging confirmed that rDME addition up to 30% does not fundamentally alter macroscopic spray morphology, ensuring compatibility with existing LPG hardware. The final phase of the work involved experimental testing on a heavy-duty single-cylinder Cummins X15 engine and the development of the ALPINE-DME 158 chemical kinetic mechanism. The mechanism was rigorously validated across 0D ignition delay times and 1D laminar flame speeds before being implemented in a 3D CONVERGE environment to predict engine performance of LPG/DME blends. Experimental results demonstrated a significant departure from natural gas performance limits, achieving a peak brake thermal efficiency (BTE) of 41.1% at low loads and 42.9% BTE at high load conditions by leveraging an increase of end gas autoignition (EGAI). The ALPINE-DME 158 mechanism successfully captured the experimental heat release rates and autoignition events by resolving radical bottlenecks

specifically premature HO2 and H2O2 accumulation observed in legacy chemical kinetic models. Collectively, this work provides a validated, predictive roadmap for leveraging high-reactivity oxygenated fuels to narrow the efficiency gap between spark-ignited and diesel heavy-duty architectures.

ACKNOWLEDGMENTS

SI must begin my acknowledgments by expressing my profound gratitude to my advisor, Dr. Bret Windom, for providing me with what has truly been a life-altering opportunity. I am forever grateful that Dr. Windom offered to take me in as a student. Over the course of this program, he has evolved from an advisor into a trusted mentor and a true friend someone I hold in the highest regard both professionally and personally. His infectious enthusiasm for research and his tireless commitment to technical excellence have fundamentally shaped my approach to science. Beyond the laboratory, his steady encouragement during the most challenging phases of my research and his genuine support through life's various hurdles have been instrumental to my success. I can say with certainty that reaching this milestone would not have been possible without his unwavering guidance.

I also would like to thank all of my Powerhouse friends for providing their time and knowledge with me. In particular, I would like to thank Stephen Lucas, Toluwalase Fosudo, Siddesh Bhoite, Miguel Valles, and Manav Sharma for always being willing to teach me new things and their openness in discussing research ideas.

I acknowledge the U.S. Department of Energy's Office of Energy Efficiency and Renewable Energy (EERE) who provided funding for this research under the award number DE-EE0009198. I would also like to thank the Colorado State University Energy Institute and its Powerhouse Energy Campus for providing the research facility and resources.

Finally, I am deeply grateful to my mother and sister, Stacie and Paige Churchill. This journey would have been extremely challenging without their unwavering support, continued encouragement, and the constant push to pursue this degree.

TABLE OF CONTENTS

LIST OF TABLES

LIST OF FIGURES

LIST OF DEFINITIONS

AFR - Air-Fuel Ratio

AHRR - Apparent Heat Release Rate

aTDC - After Top Dead Center

bTDC - Before Top Dead Center

BDC- Bottom Dead Center

BMEP - Brake Mean Effective Pressure

BSEC - Brake Specific Energy Consumption

BTE - Brake Thermal Efficiency

CA50 - 50% Burn Crank Angle

CAD - Crank Angle Degrees

CFR - Cooperative Fuel Research

CH2O - Formaldehyde

CI- Carbon Intensity

CO - Carbon Monoxide

CO2 - Carbon Dioxide

COV - Coefficient of Variation

CR - Compression Ratio

CSU – Colorado State University

DI - Direct Injection

DME – Dimethyl Ether

EGAI - End-Gas Auto-Ignition

EVC - Exhaust Valve Closing

EVO - Exhaust Valve Opening

f-EGAI - Fraction of End-Gas Auto-Ignition

FFT - Fast Fourier Transform

GDI - Gasoline Direct Injector

H2O2 – Hydrogen Peroxide

HC- Hydrocarbons

HO2 - Hydroperoxyl Radical

HPSC- High Pressure Spray Chamber

ICE- Internal Combustion Engines

IMAP - Intake Manifold Air Pressure

IMEP - Indicated Mean Effective Pressure

IMAT- Intake Manifold Air Temperature

IVC - Intake Valve Closing

IVO - Intake Valve Opening

KI - Knock Integral

KOCA - Knock Onset Crank Angle

LECM - Large Engine Control Module

LFS - Laminar Flame Speed

LHV - Lower Heating Value

LLNL – Lawerence Livermore National Laboratory

LPG - Liquefied Petroleum Gas

MBT - Maximum Brake Torque timing

MFB - Mass Fraction Burned

MON – Motor Octane Number

NG – Natural Gas

NOx - Oxides of Nitrogen

OH - Hydroxide

ON - Octane Number

PFI - Port Fuel Injection

PM - Particulate Matter

ppm - parts per million

PRF – Primary Reference Fuels

rDME – Renewable Dimethyl Ether

RON - Research Octane Number

SCE - Single Cylinder Engine

SI - Spark Ignited

SOI - Start of Injection

TDC - Top Dead Center

THC - Total Hydrocarbons

TSF – Toluene Standardization Fuels

UCSD – University of California San Diego

USC – University of Southern California

CHAPTER 1 – INTRODUCTION

1.1 Backgrounds

1.1.1 Liquefied Petroleum Gas (LPG)

Fossil fuels have contributed to the growth and development of our world while advances in technology coupled with increased understanding of combustion science have supported this progress and allowed for continued advancement. Fossil fuels such as petroleum, coal, and natural gas accounted for 82% of the total energy consumption of the United States in 2024, shown in Figure 1.1 [1]. While fossil fuels will likely remain essential for meeting energy demands through 2050, during recent years concerns about their environmental and health impacts have driven global efforts to find sustainable alternatives.

Higher energy demands combined with the need to improve engine efficiency and emissions have influenced the development of new fuels and the understanding of their properties. Liquified Petroleum Gas (LPG) has seen increased use as an alternative fuel in spark ignited engines, especially in heavy duty applications due to its high knock resistance and ability to reduce emissions [2]. For example, Walls et al. [3] performed engine experiments to quantify the brake thermal efficiency differences observed with LPG and gasoline finding that at low and medium loads LPG kept the same efficiency as gasoline but improved efficiency at higher loads while also reducing HC, CO and soot emissions [3]. Utilizing LPG as an alternative fuel offers a good compromise between combustion/fuel properties and reduced emissions. The vapor pressure of LPG allows it to be easily stored as a liquid when under moderate pressures facilitating easier transportation of tanks thus offering advantages over conventional storage methods for other fuels such as natural gas which utilizes gas compression or cryogenics to achieve a liquid form.

Furthermore, LPG has faster flame speeds than natural gas [4], providing a comparable performance to those of gasoline but with the capability of higher knock resistance [5].

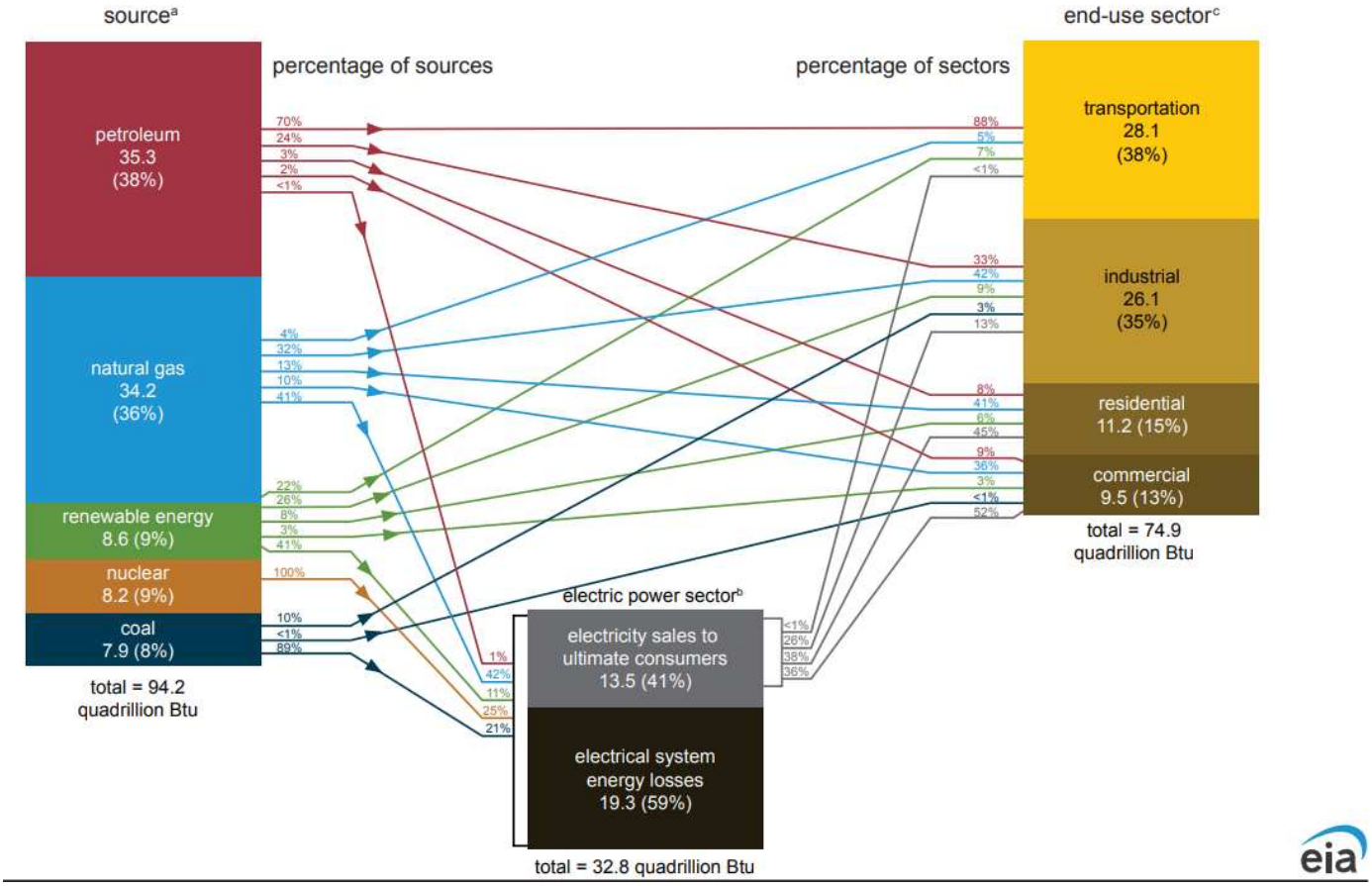

Figure 1.1. United States Energy Consumption by both the source and the end-use sector for the year of 2024.

LPG can be utilized to displace traditional fossil fuels like diesel and gasoline providing vast benefits for both the environment and economy [6]. Using LPG as a fuel source offers reductions in emissions but it also diversifies the U.S. fuel supply through the implementation of domestically produced fuels which can help reduce the reliance on imported petroleum. The primary constituent of LPG is propane, which can be produced from both renewable and fossil-based sources. However, the majority of LPG is derived from fossil fuels through crude oil refining

or natural gas processing. This fossil-derived LPG is available domestically in large quantities as over 2.2 million barrels per day of propane were produced at natural gas processing plants in December 2024, but over 1.9 million barrels are exported daily [7]. This does not include the renewable propane that is produced at approximately 4 million gallons per year [8]. If the United States were to slow exportation of LPG and allow for the widespread use of domestically produced LPG, it would allow the country to reduce its reliance on imported petroleum while contributing to emission reductions [9, 10].

To fully capitalize on the benefits of LPG, modern fuel injection strategies, such as port fuel injection (PFI) and direct injection (DI), can be adapted to optimize performance. These advanced injection techniques are crucial for improving fuel efficiency and emissions, confirmed through experiments conducted by Fosudo et al. [11] finding 34% efficiency with a naturally aspirated PFI system. While PFI developments show promising results due to their inherent mixture stability, recent advancements in DI technologies have positioned LPG DI as a superior option for heavy-duty applications. DI allows for the exploitation of LPG's high latent heat of vaporization, providing an in-cylinder cooling effect that suppresses knock and enables the use of higher compression ratios.

Characterizing the fuel injection systems, as well as the fuel vaporization and dispersion processes in the combustion chamber, is crucial for investigating and improving the combustion process ultimately leading to efficiency and emissions improvements [12]. Due to its unique physical properties and tendency to flash boil, LPG will require modifications to injection hardware and combustion chamber designs, as well as adjustments to operational strategies to achieve efficiencies surpassing those of current gasoline direct injection (DI) systems. Consequently, further research is needed to study LPG and characterize its mixing processes before

it can be integrated into current DI engines [13]. Schlieren and Mie imaging techniques are common options to provide a visualization of the spray development and the ability to provide deeper understanding of the mechanisms governing fuel spray behavior. The imaging results are used to further validate an LPG spray model leading to facilitate the development of accurate, high-fidelity simulations that can support the design of fuel injection systems tailored for high-efficiency LPG engines.

1.1.2 Dimethyl Ether (DME)

Dimethyl Ether (DME) has been extensively studied as an alternative fuel for automotive applications, primarily as a drop-in replacement for diesel fuel in compression ignition applications. For example, Boehman et al. conducted various studies examining the challenges and feasibility of utilizing DME for engine operation finding that DME can function well in compression ignition engines operating alone or in a mixed mode system with little modification required to the diesel fueling [14, 15]. Boehman et al. also demonstrated the application of DME in dual-fuel engines through experiments where DME was mixed with propane and fumigated into the intake air of a diesel engine. The results showed significant increases in brake thermal efficiency (BTE) and reductions in brake specific energy consumption (BSEC) compared to baseline diesel operation [16]. Engine testing additionally revealed the NOx emissions decreasing although an increase in total hydrocarbon emissions was captured with the results of this study shown in Figure 1.2 [16]. In addition, researchers at Oak Ridge National Laboratory further compared diesel and DME for a heavy-duty truck, finding that DME produced the same engine efficiency while vastly reducing all types of emissions [17]. The lack of carbon-to-carbon bonds present in DME promotes its use as an alternative compression ignition fuel because of its ability

to vastly reduce particulate emissions, negating the requirements of diesel particulate filters [17-x(18)].

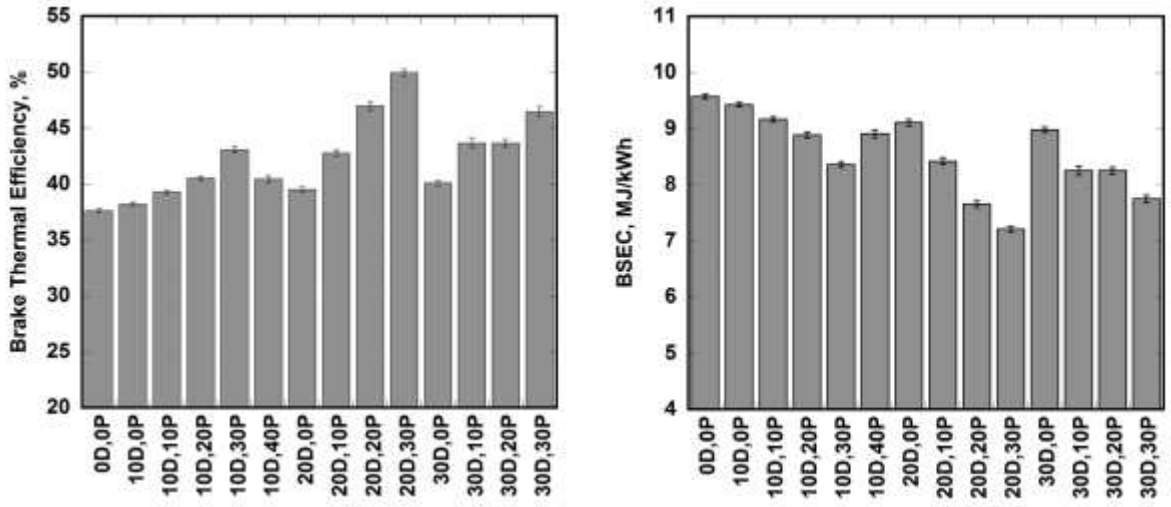

Figure 1.2. Results from Boehman et al [16] showing the increase of brake thermal efficiency and the decrease of the brake specific energy consumption at varying DME and propane substitution levels compared to the diesel baseline

rDME has shown promising success in reducing overall carbon intensity of DME, primarily through production techniques that effectively utilize captured carbon dioxide [19, 20]. For example, a study integrating separation enhancement by membranes or sorption enhancement (SEDMES) for the production of CO_2 derived DME suggests that, with the use of renewable energy for CO_2 capture and effective heat integration, the process could result in a reduction of approximately 90% in carbon emissions from transportation compared to the use of current fossil fuels [21]. Utilizing rDME blends leverages LPG's favorable combustion properties to reduce carbon intensity on two fronts, through tailpipe emissions and cleaner fuel production.

DME can reduce the overall carbon intensity of the fuel by reducing combustion emissions and by utilizing production methods that lower the carbon footprint. Furthermore, for industrial

applications, DME is produced from syngas through either direct or indirect processes. For the one step approach, DME is produced directly from syngas through a single reactor that utilizes a bifunctional catalyst to support both the formation and dehydration of methanol [22]. The indirect approach shown in Figure 1.3, separates the reactions to take place in two reactors each using a specific catalyst to support either methanol formation from syngas or methanol dehydration to produce DME. The syngas and other reactants that feed the reactions to produce DME are made from renewable sources either through an electrochemical approach or by way of organic wastes ranging from biomass, agriculture, municipal, and cellulosic (Figure 1.4) [23]. Examining the organic waste approach, syngas can be generated from biomass via a gasification process, which is then fed to either an indirect or direct process to produce DME, or alternatively, if organic wastes are utilized, syngas is generated through anaerobic digestion coupled with a pyrolysis system. The electrochemical approach utilizes an electrolyzer powered with renewable energy, such as solar or wind, to create hydrogen which is mixed into the syngas stream to feed DME synthesis [22].

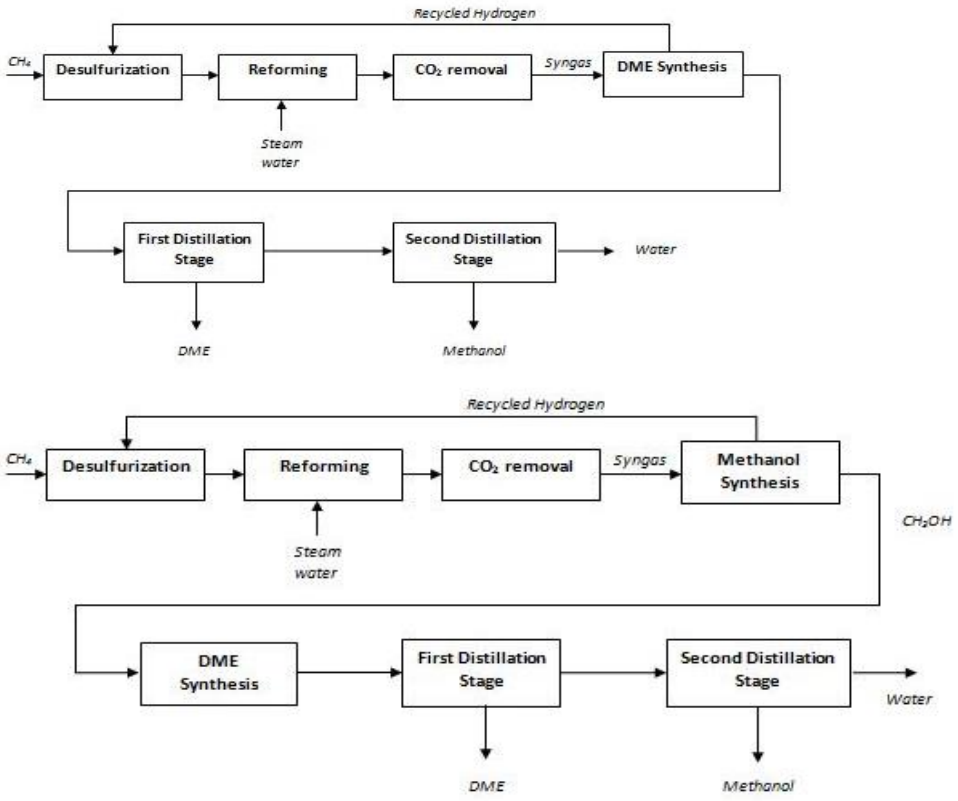

Figure 1.3 Direct vs Indirect DME production processes

Recent efforts have examined the ability to use CO_2 or captured carbon instead of syngas coupled with renewable feedstocks to enable either a negative or close to net zero carbon intensity for the production of DME. To enable industry scale production of DME from CO_2 further refinements are required and are currently being worked on in the field through demonstration plants for CO_2-to-DME conversion. Recently, a pilot plant for CO_2-based DME was developed as part of the European Project ALIGN-CCUS. The process captures 180 kg of CO_2 per day from a lignite-fired power plant and converts it into DME producing 50 kg of crude DME a day [20, 21]. In the United States Oberon fuels has created a large-scale renewable plant where their process can produce rDME fuel with low or even negative carbon intensity (CI), depending on the feedstock. The California Air Resources Board (CARB) has estimated that Oberon's process could

produce renewable DME with a CI of –278 [23] when compared to renewable propane with a CI ranging between 7 and 43 [24]. To produce renewable propane, biomass-derived compounds, typically fatty acids or triglycerides from oils, undergo conversion into hydrocarbons through processes such as hydrocracking or hydrogenation. These processes often necessitate the addition of hydrogen to break down larger molecules, refining them into shorter-chain hydrocarbons, such as propane. The production of renewable propane thus requires additional hydrogenation or hydrocracking steps, which are energy-intensive and necessitate specialized equipment. As a result, the production of renewable propane is inherently more complex and resource-demanding than conventional propane and rDME production methods [25].

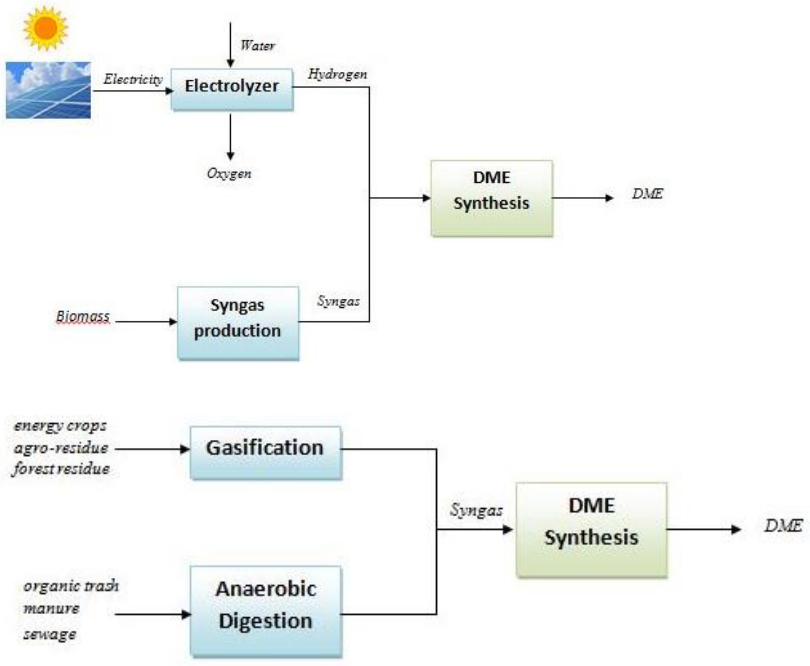

Figure 1.4. Renewable pathway process diagram for DME production

The use of DME is hindered by its lower energy density, having a lower heating value (LHV) of about 28.9 MJ/kg compared to approximately 42.7 MJ/kg for diesel [26]. This lower energy density requires an increased mass flow rate to deliver the same energy requirements and demanding more onboard storage of DME. DME alone has not been studied in spark ignition

applications but due to its vapor pressure of 5.928 bar at 25°C being close to the vapor pressure of propane of 9.533 bar at 25°C, DME has been shown to blend and mix uniformly with LPG. Renewable DME blended with LPG has the potential to obtain the desired combustion characteristics to reduce the overall lifecycle carbon intensity of LPG while performing better than existing automotive fuels.

DME is a highly reactive fuel, so while its combustion properties have seen DME thrive in compression ignition applications, it creates limitations and challenges that need to be overcome to allow DME to be used in a spark ignition engine. The ignition chemistry of DME results in more chain branching pathways that produce the pool of OH radicals promoting a faster heat release and ignition when compared to other conventional fuels such as propane. The oxidation of DME results in a two-stage heat release process which poses risks in spark ignition applications due to the higher tendency of knock. Knock or end-gas autoignition is a phenomenon observed in spark ignited applications whereas the unburned mixture ahead of the flame front experiences a rise in both pressure and temperature causing autoignition of the remaining unburned mixture. The autoignition event can release energy at a higher rate than normal combustion causing high frequency pressure oscillations inside the cylinder potentially damaging engine components. The knock resistance of a fuel used for a spark ignited engine is characterized primarily by two octane numbers, a research and motor octane number. The tendency of DME to auto-ignite limits the suitable operating conditions for spark ignition applications, but DME blended with fuels that already have a high resistance to knock such as LPG could function as a viable alternative to gasoline while improving engine performance and reducing emissions.

1.1.3 Potential of LPG/DME Blends

The production of LPG being primarily from fossil fuels highlights the need for new approaches that reduce the overall carbon intensity of the fuel. One promising solution lies in blending LPG with alternative, renewable fuels like (renewable) dimethyl ether (rDME). Figure 1.5 views some of the potential carbon intensity reduction benefits that are obtainable by blending renewable DME (rDME) with LPG, where 20% rDME blend ratios can provide up to a 60% decrease of the overall CI for the generation of the blended fuel as reported by Oberon Fuels. Previous studies have demonstrated the significant impact of dimethyl ether (DME) on fuel combustion. Chen et al. [27] found that DME enhances the ignition of methane-air mixtures more effectively than equivalent hydrogen and linearly increases their flame speed. Complementing this, Zhang et al. [28] utilized DME as a radical initiator to investigate its influence on toluene ignition using both rapid compression machines and shock tubes. Collectively, these works show that DME addition substantially improves ignition characteristics and can increase flame speeds, aiding in the combustion of less reactive fuels relevant to engine applications [27, 28]. Previously, the work of Boehman et al [16] with propane and DME fumigation substitution shown in Figure 1.2 indicates some of the possible benefits that can be obtained with fuel mixing.

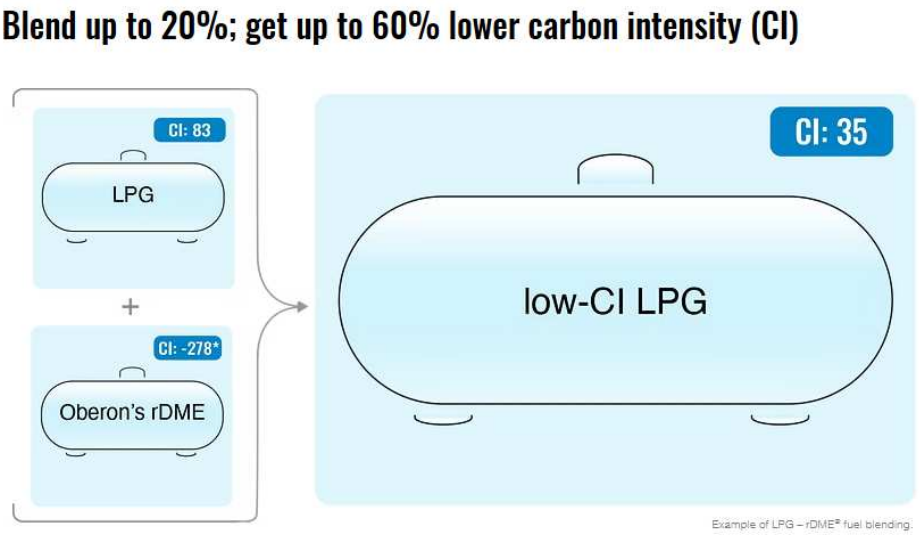

Figure 1.5. Obtainable carbon intensity (CI) reduction possible for blending LPG with renewably produced DME calculated by Oberon fuels.

Soto et al. [29] investigated the effects of DME and propane blends in a boosted SI engine utilizing two parameters, the intake pressure and the fuel composition to examine the impact of knocking behavior with respect to the combustion phasing, engine efficiency, and emissions (Figure 1.6). From their engine testing, Soto et al. determined that the knock intensity of blends up to 20% DME performed similar to LPG, being able to maintain MBT and engine operation while the 30% blend was knock-limited in all the experimental conditions. The results from Soto's experiments highlight the need to understand how the addition of DME changes the fuel blend's reactivity. The behavior of premixed combustion is well understood by examining the fuel's reactivity through the characterization of the octane number but for fuels that utilize direct injection the mixing behavior could vastly differentiate itself from the established behavior determined with premixed combustion. Fosudo et al. [30] has found that utilizing direct injection of LPG can achieve diesel-like efficiency while reducing emissions. DI LPG has the potential to offset traditional fuel usage while obtaining better engine performance, the benefits of DI LPG could

also be realized with LPG/DME blends while the presence of DME could further reduce emissions and increase combustion efficiency. The potential benefits of utilizing both PFI and DI LPG/DME blends have been largely unexplored and further analysis into the spray dynamics needs to be conducted to understand the mixing effects of LPG and DME blended fuels.

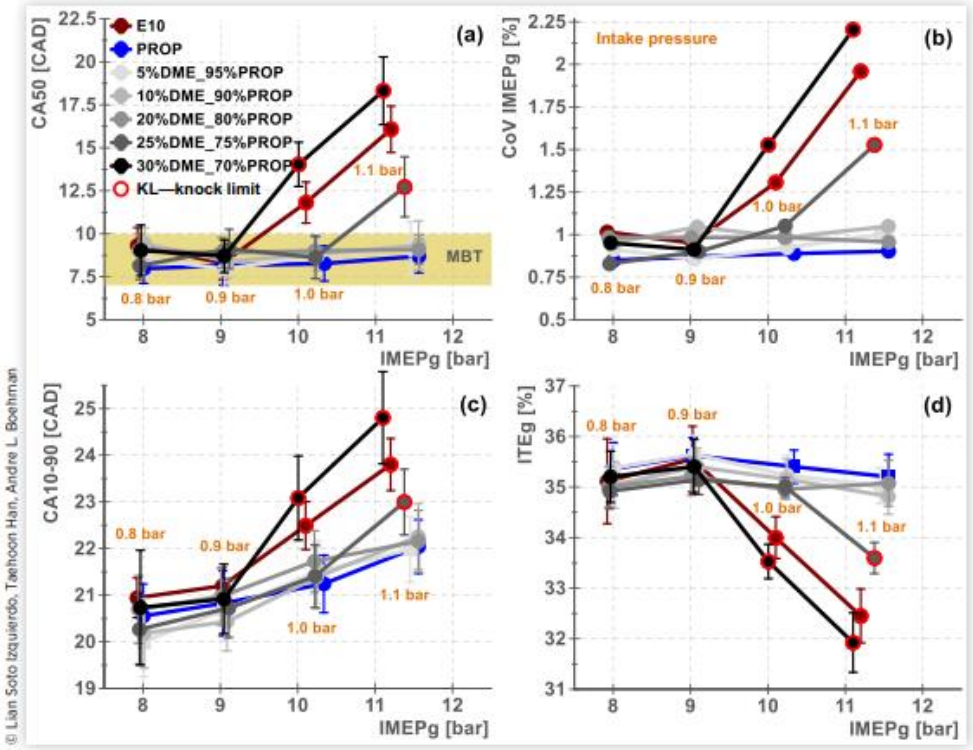

Figure 1.6. Experimental results obtained from Soto et al. [29] highlighting the combustion and performance effects of DME addition on boosted spark ignited engine operation.

1.1.4 LPG/DME Chemical Kinetic Mechanisms

A survey of currently published literature reveals a significant deficiency in chemical kinetic mechanisms specifically optimized for LPG/DME mixtures. While comprehensive models exist, their implementation in 3D engine simulations is often restricted by computational overhead. For instance, the C3MechV3.5 developed by the Computational Chemistry Consortium (C3) is highly detailed, containing 3,768 species and 16,575 reactions [31]. The sheer scale of this

mechanism exponentially increases simulation run times, thereby reducing its utility for complex 3D engine modeling. Even when utilizing the C3 framework's capability for reduction by carbon number—reducing the model to hydrocarbons up to C5—the resulting mechanism remains substantial, consisting of 794 species and 4,179 reactions.

Similarly, the Aramco 3.0 mechanism [32] presents comparable challenges; with 581 species and 3,037 reactions, its size impedes its application in computationally intensive internal combustion engine simulations. While alternative mechanisms exist that incorporate both LPG and DME pathways, they are often limited in scope or validation. The Mod Mech C5, developed by Hu et al. [33], was primarily validated using shock tube experiments. This model, consisting of 295 species and 1,584 reactions, was constructed by integrating the DME chemistry developed by Zhao et al. [34] (55 species, 290 reactions) into the NUI Mech C5 base framework. Hu et al. [33] utilized this model to highlight performance differences between blended and pure DME, while concurrently employing the USC mechanism [35] (111 species, 784 reactions) as a benchmark for pure propane simulations.

Beyond comprehensive hydrocarbon frameworks, several specialized pure-DME mechanisms have been developed with varying degrees of complexity. The Lawrence Livermore National Laboratory (LLNL) [36-38] developed a DME mechanism consisting of 79 species and 351 reactions, while the University of California San Diego (UCSD) [39] offers a highly compact DME sub-mechanism. The UCSD DME chemistry consists of only five species and 14 reactions, designed to be integrated into their broader framework of 59 species and 271 reactions. Additionally, the DME mechanism developed by Zhao et al. [34] has been recognized in literature for its superior ability to capture experimental oxidation behavior.

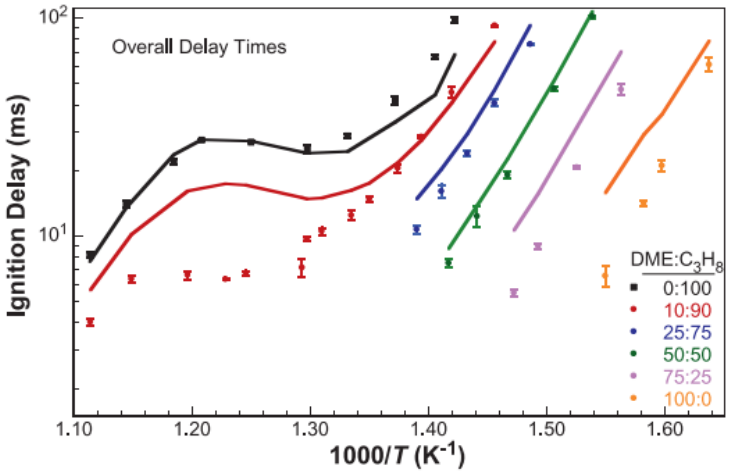

Figure 1.7. Dames et al. [40] comparison of RCM ignition delay simulations to experimental data for LPG/DME blends and their pure constituents.

Despite these individual advancements, there remains a notable lack of research into chemical mechanisms capable of accurately modeling the full spectrum of LPG, DME, and their intermediate blends. Currently, Dames et al. [40] provides the only published experimental data regarding these blends at low-to-intermediate temperatures using rapid compression machine (RCM) experiments. Utilizing this data, Dames et al. [40] developed a specialized kinetic mechanism comprising 120 species and 711 reactions. However, as illustrated in Figure 1.7, while their mechanism demonstrates strong predictive performance for 100% LPG and 50% DME blend remaining within experimental uncertainty, it diverges significantly from experimental results at other blend ratios. This divergence, which falls vastly outside the bounds of uncertainty, underscores the existing deficiency in kinetic modeling. These disparities in mechanism scale and validation environments underscore the need for a reduced, high-fidelity framework capable of resolving the interactions of LPG/DME blends within the constraints of 3D computational fluid dynamics (CFD).

1.2 Research Questions

Examining the published literature regarding LPG, DME, and LPG/DME mixtures there are certain gaps in understanding that need to be addressed for mixtures of LPG/DME to be a viable alternative fuel. LPG and DME both offer pathways to decrease emissions from traditional fuels while their mixtures can provide the same benefits observed in previous published literature. LPG's physical and chemical properties have been studied through previous engine testing and modeling efforts to capture the performance benefits of LPG highlighted in the literature review above. There have been efforts by CSU and Argonne national lab to capture the flashing effects observed with LPG, defining constants to be used in modeling that represent different levels of flashing but there is more work that needs to be done to accurately model this behavior and ensure that it is valid to capture and predict engine performance of DI systems. If the spray model is not accurate, then the extrapolated conclusions are not valid and cannot be used to predict the performance changes when adapting different load conditions or other engine hardware.

The main goal of this work is to characterize the combustion process for both LPG and LPG/DME blends, as there is a vast interest in the implementation of these fuels into heavy-duty engine operation. By filling critical gaps in the currently sparse knowledge regarding the chemical and physical behavior of these alternative fuels, this research seeks to define the operational boundaries of high-reactivity LPG/DME blends. The inability of existing kinetic models to maintain fidelity across the full spectrum of LPG/DME blends represents a critical barrier to the optimization of heavy-duty alternative fuel engines. To address this deficiency, it is necessary to move beyond standard hydrocarbon frameworks and develop a coupled numerical and physical approach. This research, therefore, utilizes a multi-phase methodology involving fuel characterization, mechanism hybridization, and high-fidelity 3D-CFD to provide knowledge to the

industry to allow for the implementation of these fuels. To add to the lack of knowledge of LPG and LPG/DME blends this work aims to answer the following fundamental research questions:

1. Can we develop a modeling approach to investigate LPG performance differences between PFI and DI operation?
    a) What governs the non-linear relationship between start of injection (SOI) and combustion stability in DI operation, and why is this sensitivity absent in PFI configurations?
    b) Can the integration of a reduced chemical kinetic mechanism (ALPINE 153) with a liquid spray model accurately predict in-cylinder mixture formation?
    c) Why do specific DI SOI timings result in a performance decline followed by recovery observed in experimental engine operation?
2. What is the feasibility of reducing the CI by adding DME to LPG for SI engines?
    a) How does the addition of high reactivity DME to LPG alter the chemical sensitivity (RON/MON)?
    b) How does DME addition alter the macroscopic spray morphology and atomization characteristics of an LPG base?
3. Does the integration of DME into LPG provide a viable pathway for heavy-duty SI operation, when compared to natural gas and LPG benchmarks?
4. Can we construct a modeling approach that can explore using LPG/DME blends in large bore engines?
    a) Can a reduced kinetic chemical mechanism capture the flame speeds and ignition tendencies of these blended fuels?

b) Given highly limited established kinetic framework that exists for LPG/DME blends, how can a C1–C4 hydrocarbon base mechanism be expanded to resolve the coupled effects of varying reactivity across the full spectrum of blend ratios?

The following chapters are structured to systematically address these inquiries through a combination of experimental characterization and high-fidelity numerical simulations.

1.3 Dissertation Overview

1. Chapter 1 presents a background on both LPG and the potential benefits of LPG/DME blends while framing the current gaps in literature that this work is trying to answer through the research questions provided.
2. This chapter establishes the technical framework for the dissertation by detailing the experimental and numerical methodologies employed across all conducted studies. It provides a comprehensive description of the experimental platforms, including the High-Pressure Spray Chamber (HPSC), the Cooperative Fuel Research (CFR) octane engine, and the single-cylinder Cummins X15 platform. Additionally, the chapter defines the numerical setup for the 3D CFD simulations, covering mesh sensitivity studies, boundary condition configurations, and the selection of physical sub-models within the CONVERGE environment
3. This chapter establishes the foundational reliability of the research by detailing the validation of the "Extreme Flash" KH-RT spray model against High-Pressure Spray Chamber (HPSC) data. The work explores the sensitivity of engine performance to atomization sub-models across varying injection timings. Furthermore, 3D CFD simulations are utilized to investigate the role of Turbulent Kinetic Energy (TKE) and piston-top velocity profiles in stabilizing late-cycle DI strategies.

4. Transitioning from physics to chemistry, Chapter 4 details the experimental characterization of rDME/LPG blends using a Cooperative Fuel Research (CFR) engine. This phase focuses on quantifying the Research Octane Number (RON) and Motor Octane Number (MON) for blends up to 30% DME. The objective is to define the operational boundaries and Anti-Knock Index (AKI) of these blends to determine their viability as drop-in fuel surrogates.
5. Chapter 5 evaluates the hardware compatibility of LPG/DME blends. Using high-speed spray visualization, the research examines the impact of DME addition on macroscopic spray structure, penetration, and cone angles. This study determines whether the physical properties of the blended fuel necessitate modifications to existing high-pressure DI hardware or if existing systems can accommodate high-reactivity fuels without mechanical adjustment.
6. Chapter 6 details the application of LPG/DME blends on a heavy-duty single-cylinder Cummins X15 platform. This phase of the research focuses on experimental performance mapping across low and high-load regimes to evaluate the efficiency potential of various blend ratios. In parallel, the chapter details the development and implementation of the ALPINE-DME 158 chemical kinetic mechanism. The work focuses on validating this mechanism's ability to operate within a 3D CFD environment, specifically benchmarking its predictive accuracy against experimental in-cylinder pressure, heat release rates, and the onset of end-gas autoignition events. This dual approach provides a methodology for using high-fidelity simulations to interpret the complex combustion characteristics observed during the experimental testing of high-reactivity oxygenated fuels.

7. This final chapter synthesizes the results from the various experimental and numerical studies to provide a unified perspective on LPG and LPG/DME combustion. It identifies the consistent themes connecting spray physics, fuel chemistry, and engine performance, highlighting the primary contributions of this work to the field of alternative fuel research. The dissertation concludes with an analysis of potential future research directions, focusing on further improving efficiency and reducing emissions in heavy-duty platforms.

CHAPTER 2 – EXPERIMENTAL AND NUMERICAL MODELING METHODS

2.1 LPG Medium to Heavy Duty Engine Experimental Setup

The experimental section of this work was conducted on a single cylinder Cummins ISX15L research engine. The baseline engine was a 15L-displacement 6-cylinder diesel engine modified for spark ignition operation with direct injection LPG. The modification involved deactivating cylinders #1-5 and allowing combustion only in cylinder #6 with its componentry adapted for spark ignition combustion. The firing cylinder, cylinder #6, in this single cylinder ISX15L spark ignition engine configuration also involved the installation of several new components including ring sets, pistons, bearings, cylinder liner etc. A spark plug adaptor was included in the machined cylinder head to accommodate the spark plug required for spark ignited operation. Several other parts were eliminated during the process of converting the 6-cylinder engine for single cylinder engine (SCE) operation including the turbocharger, the diesel fuel pump and high-pressure rail, and parts of the EGR system (cooler and valve) amongst others. A more complete description of the modification process can be found in [41-43]. A picture of the SCE in the operation and a CAD model is shown in Figure 2.1.

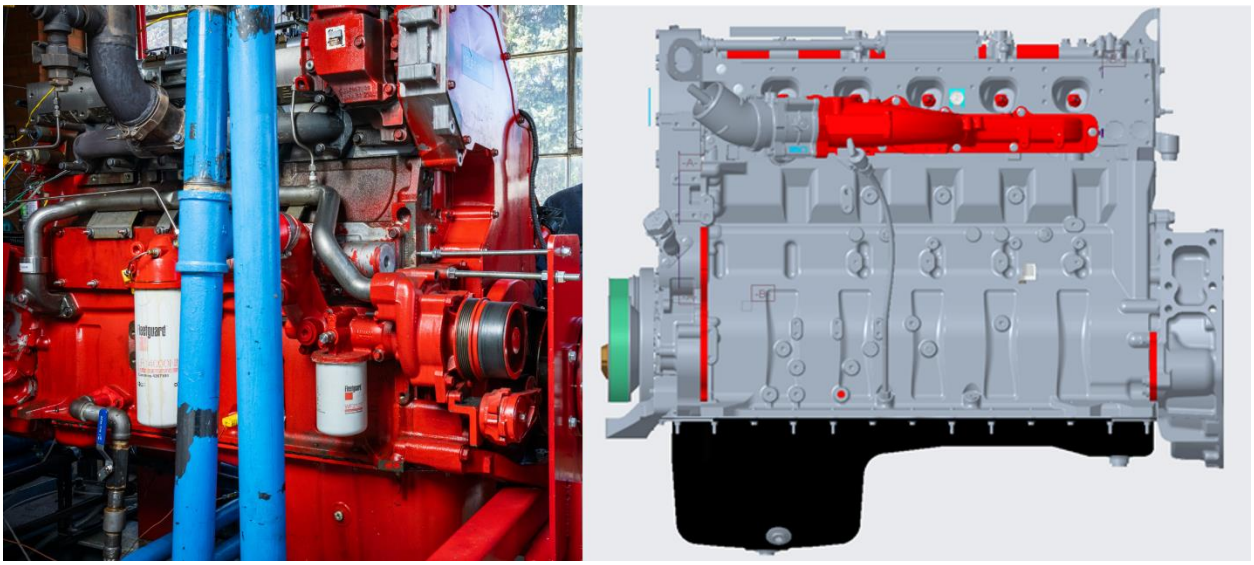

Figure 2.1. Left: Picture of the exhaust side of the engine showing the oil and coolant pipes. Right: CAD model showing the intake side of the engine.

The SCE was instrumented during its conversion and afterwards to provide reliable performance, combustion and emissions data. In-cylinder pressure was measured with a 0 – 300bar AVL GH14DK pressure transducer installed in the modified cylinder head. Cylinder pressure, intake manifold pressure (IMP), exhaust manifold pressure (EMP) are crank angle synchronized to facilitate combustion analysis and also provide high fidelity boundary information for computational modeling of the engine combustion. The IMP was measured with a high speed Kistler 4007D transducer and the EMP measurements were made with a water-cooled Kistler transducer (4049B). Both transducers were piezoresistive and required modification to their respective manifolds for their installation. Crank angle data was provided by a BEI H25 series encoder with 0.1 resolution. An Eaton SVX variable drive (VFD) controlled the engine speed, and a Bronkhorst M15 Coriolis flow meter measured fuel flow rate into the engine. Using the fuel flow controls, equivalence ratio in the cylinder was controlled with feedback from an LSU 4.9 wide-band lambda sensor installed downstream of the active cylinder, in the exhaust stream. The spark

ignition configuration experiments involved providing consistent ignition in the cylinder with a massive 3-prong Altronic L1863B nickel spark plug designed for large bore stoichiometric engines and switching the piston hardware between two pistons with different compression ratios and bowl designs, a baseline 9.3:1 piston and a 12:1 piston. Comprehensive descriptions of the spark plugs, pistons and engine instrumentation can be found in [30]. Engine data was monitored and logged with LabView, while a Woodward large engine control module (LECM) maintained control over the spark and injection timings and the equivalence ratio while also providing real-time feedback on the in-cylinder conditions during engine operation. Table 2.1 contains a detailed specification of the heavy-duty SCE configuration used in this study.

Table 2.1: Single Cylinder Engine (SCE) details

Manufacturer	Cummins
Model	ISX15L
Displacement volume (m^3)	0.0025
Stroke (m)	0.169
Bore (m)	0.137
Connecting rod (m)	0.2615
Number of valves	4
Exhaust valve open and close	19^0 BBDC and 2^0 BTDC
Intake valve open and close	11^0 BTDC and 155^0 BTDC
Compression ratio	9.3, 12:1
Injection details	PFI: Siemens DEKA Injector DI: Modified 5-hole Delphi Injector

2.1.2 PFI/DI Injection Configuration

The research engine was operated using two injection configurations: a port-fuel injection (PFI) mode and a direct injection (DI) mode. The PFI configuration was designated as the baseline injection configuration with liquid LPG to replicate the operation of current LPG engines on the

market on the single cylinder heavy-duty research engine. The Power Solutions International 8.8L-V8 engine and the Roush Cleantech Ford 6.8L-V10 engine, used in the Navistar 44 CE Series and the Blue Bird school buses, respectively, are two of such LPG engines currently on the market. Both engines make use of the liquid fuel port injection strategy and have compression ratios between 9 and 10:1. The port injector used in this study was the Siemens DEKA injector found in the Blue Bird Ford 6.8L-V10 engines. The PFI injector delivered liquid LPG consistently at 1.6MPa at all engine operating conditions. A nitrogen gas-on-propane system was used to pressurize the liquid propane to the required injection pressure and while the fuel delivery systems for both the PFI and DI configurations had certain similarities, both modes required specific hardware for their integration and operation with liquid LPG on the heavy-duty SCE. The PFI fuel delivery set-up included a Coriolis flow meter for fuel flow measurement and control, a continuous sampling line connected to a gas chromatograph for fuel composition details, several absolute pressure transducers and K-type thermocouples for pressure and temperature measurements, a pressure relief valve, and a high-pressure nitrogen gas supply cylinder fitted with a pressure regulator. Comprehensive details of the integration and operation of these instruments on the liquid LPG PFI fuel delivery system can be found in [11]. Figure 2.2 shows the picture of the installed Siemens DEKA PF injector as well as the modified direct injectors and their installation location on the spark ignited engine.

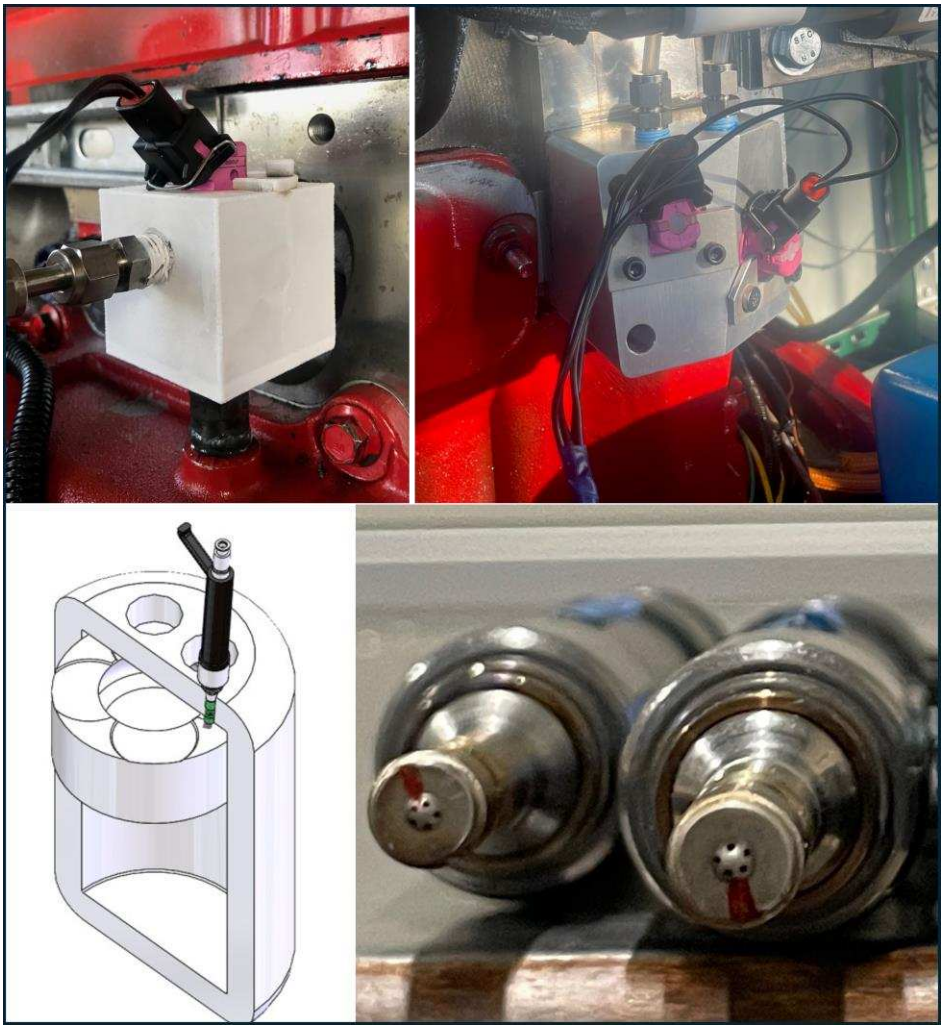

Figure 2.2. L-R A picture of the Siemens DEKA port-fuel injector installed in the baseline configuration of the engine, the double-injector valve-targeting PFI set-up for the higher compression ratio engine configuration, a CAD model of the direct injector imposed in the cylinder, and the modified direct injectors.

For the DI configuration, there were more complex design requirements for the fuel delivery system and injector design due to the higher operating pressures compared to PFI and the requirement for the injector to be installed directly in the cylinder. The DI fuel delivery system involved a double nitrogen gas-on-propane set-up with the first half moving all the propane into an intermediate high-pressure cylinder at pressures around 1.6MPa in a similar operation to the

PFI set-up. Then the second high pressure half of the double nitrogen gas-on-propane kicks in and pressurizes the liquid propane in the intermediate cylinder up to the required injection pressure. The DI system also had a double filtration system and a higher rated pressure relief valve than the PFI fuel delivery set-up. Another key design consideration was the installation location of the injector. As the engine was converted to a spark ignited engine, there had to be a spark source considered for the engine. The source, a 3-prong Altronic L1863B spark plug, was centrally installed, and to accommodate this the direct injector had to be installed in an off-center location as shown in Figure 2.2. Therefore, to achieve high pressure liquid LPG injection and prevent significant wall wetting with the LPG spray, a Volkswagen Delphi gasoline direct injector (GDI) was selected for the experiments and modified for LPG operation on the heavy-duty SCE. The modification parameters involved increasing the fuel flow rate through the injector and redesigning the nozzle pattern from a symmetric 7-hole design to an asymmetric 5-hole pattern shown in Figure 2.2. Previous works provide details of the injector modification [44] and the high-pressure fuel delivery system [30,45].

The experiments were designed to study the effect of start of injection timing on the heavy-duty LPG engine combustion in both the DI and the PFI configurations in order to optimize the LPG engine performance with each injection strategy. To achieve this, the start of injection (SOI) timing was varied using the baseline engine configuration of 9.3:1 compression ratio and port-fuel injection and then the engine was operated in direct injection mode with the same baseline piston and at the same tested SOI timings. For the baseline PFI and DI configurations, there were two SOI regions of interest. First, the late SOI region (120 deg bTDC and 150 deg bTDC), occurring after the intake valve has closed (155^{o} bTDC from Table 2.1) and all the required combustion air has been inducted into the cylinder. Next, the early SOI region (360 deg bTDC and 330 deg bTDC),

which occurs just after the exhaust valve closes, thus avoiding the short-circuiting of the LPG fuel. After the baseline studies, the compression ratio was increased to 12:1 with a new piston design and another SOI timing study conducted. For the higher compression ratio tests, the SOI was swept from 360 deg bTDC in the early SOI region through decrements of 30 degrees to 120 deg bTDC in the late region. These experiments were conducted to capture the effects of the SOI timing on mixture formation and homogeneity in the heavy-duty LPG engine and investigate its effect on engine combustion and performance for SOI timings in the early, late, and intermediate regions. Table 2.2 contains details of the test matrix and engine conditions. The LPG used in the study was sourced from a local gas supplier with consistent composition measured over the test days. The average LPG composition is also presented in Table 2.2.

Engine control and monitoring was achieved with the Woodward LECM and the NI PXIe 6363, a high-speed national instruments hardware. In-cylinder and high-speed intake and exhaust manifold data were logged using the LabView hardware for 1000 cycles at each engine operating condition and provided the basis for engine combustion analysis. The LECM also had the capacity to log data but with coarser resolution than the NI hardware. Both injectors (DI and PFI) were controlled using the LECM. Other engine parameters such as the fuel flow rate, engine speed, exhaust temperatures, and intake air pressures were monitored and logged in a separate LabView program for performance calculations. The single zone method [46] in Equation 1 was used to provide heat release history with crank angle using the in-cylinder pressure data.

$$\frac{dQ}{d\theta} = \frac{\gamma}{\gamma-1} P \frac{dV}{d\theta} + \frac{1}{\gamma-1} V \frac{dP}{d\theta}$$

(1)

Where:

P is the in-cylinder pressure,

Q is the heat release,

V is the cylinder volume, and γ is the ratio of specific heats.

In this study, the COV of IMEP captured in Equation 2 was used as a measure of engine combustion stability. COV_{imep} values below 3% denoted stable engine operation.

$$COV_{imep} = \frac{IMEP_{st.deviation}}{IMEP_{mean}} \cdot 100$$

(2)

Repeat tests were carried out at a nominal engine operating condition to provide a measure of the random uncertainty of the experimental set-up. This uncertainty was then propagated using the root of summation of squares method [47] in Equation 3.

$$W_R = \left(\sum_{i=1}^{n} \left[w_{x_i} \frac{\partial R}{\partial x_i} \right]^2 \right)^{\frac{1}{2}}$$

(3)

Where:

w_R is the total uncertainty of the result, and

w_{xi} is the uncertainty of the independent variable x_i

Table 2.2. Experimental operating conditions

Engine operating parameters. All engine tests were conducted at 1200RPM engine speed.				
Compression Ratio	9.3		12	
Injection Strategy	PFI	DI	PFI	DI
Start of Injection (deg bTDC)	120, 150, 330, 360		120 – 360	
Injection Pressure (MPa)	1.6		17	
CA50 (deg aTDC)	11	9.5	12	
Equivalence Ratio	1			
IMAP (kPa)	101.3 kPa			
MAT (ºC)	38 degree C			
LPG composition (%vol)	98.5% - C_3H8, 1% - C2H6, 0.5% - iC_4H_{10}			

2.2 3D CFD Modeling Methods

2.2.1 LPG Converge Setup

A three-dimensional numerical model of the X15 engine was developed using the CONVERGE CFD [48] software in collaboration with Cummins. The base geometry provided by the manufacturer was modified to incorporate specific variations observed during engine test cell operations. A base computational grid of 4 mm was employed, with local resolution enhanced through Adaptive Mesh Refinement (AMR) and fixed embedding.

Within the cylinder, AMR was implemented to refine the mesh based on local temperature and velocity gradients using a sub-grid scale (SGS) approach. A maximum embedding level of 3 was utilized, governed by SGS criteria of 2.5 K and 1 m/s, respectively. In contrast, the intake and manifold regions were restricted to velocity-based AMR with a maximum embedding level of 1. To resolve boundary layer effects, three levels of fixed embedding with a two-layer count were applied to the cylinder head, piston crown, and valve face boundaries. Furthermore, two concentric spherical fixed embeddings were centered at the spark plug to resolve the spark kernel and

subsequent flame propagation. This dual-resolution strategy utilized a coarse scale of 4 (8 mm radius) and a fine scale of 5 (4 mm radius).

In-cylinder turbulence was modeled via the Reynolds-Averaged Navier-Stokes (RANS) equations using the Renormalized Group (RNG) k-ε turbulence model [49]. The minimum grid size achieved through refinement has been validated in prior literature to be sufficient for capturing both nominal and knocking combustion regimes [9,12,]. Wall heat transfer was calculated using the Han and Reitz model [50], while combustion chemistry was solved using the SAGE detailed kinetics solver with adaptive zoning for computational efficiency. The spark ignition process was represented as a volumetric source term through the spark-arc and spark-breakdown models, utilizing a defined scalar to govern energy dissipation.

The combustion chemistry was simulated using the ALPINE 153 reduced chemical kinetic mechanism, developed at Colorado State University by Sluneca et al. [51,52]. This mechanism was derived from the detailed NUIGMech 1.1 framework through targeted reduction, resulting in a scheme consisting of 153 species and 1,227 reactions. The ALPINE 153 mechanism was specifically designed to balance chemical fidelity with computational economy, making it well-suited for high-fidelity 3D internal combustion engine simulations while remaining efficient enough for rapid 0D and 1D parametric studies. This reduced mechanism was integrated with the SAGE detailed chemistry solver to calculate the local species concentrations and reaction rates within the turbulent flow field.

2.2.2 LPG Spray Modeling

The direct injection (DI) spray was simulated using a coupled Lagrangian-Eulerian approach, with the liquid phase characterized by the Discrete Droplet Model (DDM) [53]. The

gaseous phase transport equations were solved within the Unsteady Reynolds-Averaged Navier-Stokes (URANS) framework utilizing the RNG k-ε turbulence model. To accurately capture the spray dynamics, several Lagrangian sub-models were integrated into the framework. Atomization and breakup were governed by the Kelvin-Helmholtz and Rayleigh-Taylor (KH-RT) models [54], which predict primary and secondary breakup without the requirement of a predefined breakup length. Droplet phase change was accounted for using the Frössling correlation, while turbulent dispersion and droplet interactions specifically collision and coalescence were managed by the O'Rourke model [55] and the No-Time-Counter (NTC) algorithm [56], respectively.

$$\boldsymbol{Superheat\ degree} = \frac{\boldsymbol{P_{amb}}}{\boldsymbol{P_{sat}(T_{inj})}} \qquad (4)$$

To account for phase change induced by flash boiling, the model proposed by Adachi et al. [57] was implemented within the computational code. This model evaluates the instantaneous superheat degree of the fuel relative to the ambient chamber conditions, defined as the difference between the local fuel temperature and the saturation temperature at the local pressure, as expressed in Equation 1. The Rayleigh-Taylor breakup parameters, summarized in Table 2.3, were adopted from previous work by the author where the model was validated for its ability to capture both extreme and non-extreme flashing conditions using a SprayG research injector [58, 59]. The correlation between the superheat degree and the observed spray collapse trends for propane informed the selection of the model parameters necessary to capture this strong thermal dependence. These validated extreme flash parameters served as the numerical baseline for the present study and were applied to a commercially available Volkswagen GDI fuel injector, which was modified for operation with LPG. Figure 2.3 shows the spray pattern for the DI injector in the 3D CONVERGE model.

Table 2.3. RT breakup model parameters for the Lagrangian spray simulations developed for LPG.

RT Breakup Model	Time Constant	Model Size Constant
Non-extreme flashing	1	0.6
Extreme flashing	0.1	0.25

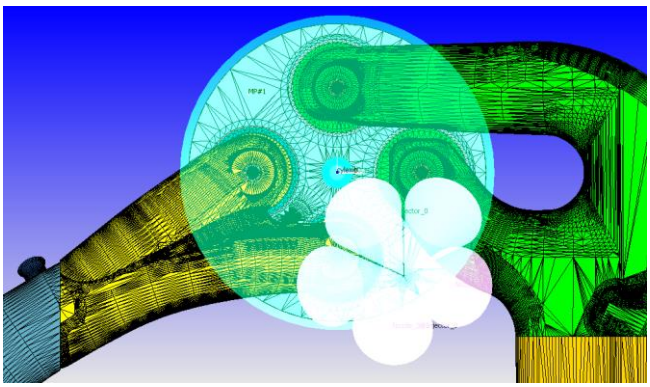

Figure 2.3. Delphi spray pattern and injector location on 3D CFD model

The integration of the ALPINE 153 kinetic mechanism with the SAGE solver, coupled with the high-resolution Lagrangian-Eulerian spray framework, establishes a robust numerical platform for evaluating the X15 engine's performance. By utilizing a refined mesh strategy specifically, the dual-resolution spherical embeddings and temperature-velocity AMR the model is capable of capturing the critical interactions between the high-pressure LPG spray, the turbulent in-cylinder flow, and the resulting flame propagation. This holistic modeling approach ensures that the governing physical phenomena, from the onset of flash boiling to the detailed chemical kinetics of combustion, are resolved with the precision necessary for a rigorous analysis of engine efficiency

and emissions. Consequently, this validated framework provides the necessary fidelity to explore the parametric variations presented in the subsequent sections of this study.

To evaluate the influence of injection timing on fuel preparation and subsequent combustion, a comprehensive start of injection (SOI) sweep was performed across six distinct timings, ranging from 340° to 120° before top dead center (BTDC). This simulation campaign utilized the experimental parameters detailed in Table 2.2 as the foundational initial and boundary conditions for the 3D CONVERGE model. To demonstrate the robustness and scaling of the numerical approach, the model was validated across two distinct compression ratios using the computational geometry illustrated in Figure 2.4. The domain was specifically configured to resolve the momentum exchange at the piston top and cylinder head interfaces. The piston top was designated as the primary diagnostic boundary for evaluating instantaneous turbulent kinetic energy (TKE), as its translational velocity is the governing factor in compression driven tumble intensification. To evaluate the evolution of the fuel-air mixture, a vertical cut-plane (Figure 2.4) was established through the central axis of the spark plug. This enabled the spatial quantification of the equivalence ratio during the ignition window, establishing a mechanistic link between boundary layer turbulence and mixture homogeneity across the studied SOI timings [60-62].

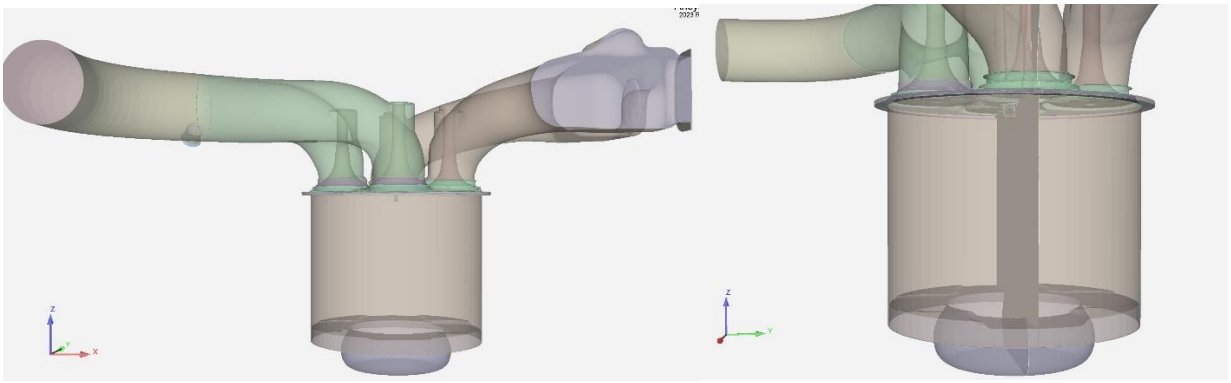

Figure 2.4. 3D Model of the test cylinder and orientation of the cut plane through the cylinder and middle of the spark plug.

2.3 Experimental Set-Up: Cooperative Fuels Engine

For the experiments conducted in this study, the engine that was utilized is a single cylinder, variable compression ratio, four stroke Cooperative Fuels Research (CFR) F-2 engine. The research engine manufactured by Waukesha Motor Company can achieve compression ratios between 4:1 and 18:1. ASTM D2699 and ASTM D2700 are the two standards used for quantifying the Research and Motor octane numbers in a spark ignited engine for liquid fuels [63, 64]. Different engines are used to carry out MON and RON testing where both testing methods use fixed operating conditions to quantify the knocking tendency of a sample fuel; the differences between the RON and MON methods arise from the need to capture the entire range of engine operation where MON tests represent more severe conditions by achieving a higher mixture temperature and speed when compared to RON testing which simulates gasoline performance under less severe conditions.

Table 2.4
Operating Conditions: RON vs MON [63, 64]

Operating Parameter	**Research Method (ASTM D2699)**	**Motor Method (ASTM D2700)**
Engine Speed	600 ± 6 rpm	900 ± 9 rpm
Air Intake Temperature	11 ± 1.0 °C [a]	38 ± 1.0 °C
Mixture Intake Temperature	Not Specified	149 ± 1.0 °C
Air Intake Pressure	Barometric	Barometric
Coolant Temperature	95 ± 1.5 °C	95 ± 1.5 °C
Spark Timing	13° BTDC	14-26° BTDC [b]

a-Variations with barometric pressure
b-Varies based on the compression ratio

The complete differences between test methods are displayed in Table 2.4. In general, the ASTM test methods determine a sample fuel's octane number by comparing the knock tendency

of the sample fuel to the knock tendency of primary reference fuels (PRFs) which have a known octane number defined in the standards guide tables.

The standard implements four different test methods for determining the octane number of sample fuels - for both the RON and MON tests of LPG/rDME blends conducted in this study, the method of Equilibrium Fuel Level Bracketing Procedure A was chosen [63, 64]. For MON testing, the ASTM standard relates the spark timing to the compression ratio with an operating range between 14-26° bTDC. For this study, the spark timing was held constant at 19° bTDC for the testing of both the sample fuel and bracketing PRFs. The ASTM standards 2699 and 2700 for MON and RON testing are not equipped with the hardware to measure the octane numbers of gaseous fuels. Modifications to the intake system hardware were implemented and an additional fuel delivery system was developed for the input of gaseous fuels. The liquid fuel 3-bowl carburetor assembly was modified to accept the input of gaseous fuels by connecting the venturi opening to the tumble mixer. The liquid fuel supply from the 3-bowl carburetor can be separated from the gaseous fuel system allowing for independent operation of both fuel types. Figure 2.5 and Figure 2.6 both show the modification made to the test cell in more detail.

Additional upgrades to the engine instrumentation were required. A National Instruments PCI 6251 high speed data acquisition card was used to collect in-cylinder pressure data. Three Kistler high-speed pressure transducers were utilized for this study, a 6061B water-cooled piezoelectric pressure transducer to provide in-cylinder pressure readings in addition to 4007D and 4049B piezoresistive transducers to take dynamic intake and exhaust pressure measurements. K-type thermocouples were installed at various locations to measure temperature of the fuel, oil, engine coolant, intake air, and exhaust buffer volumes. Absolute pressure transducers provided by Omega Engineering were utilized to measure the fuel rail, air intake and exhaust buffer volume

pressures. The in-cylinder pressure transducer was pegged using the intake dynamic pressure transducer at the intake valve closing (IVC) timing. This dynamic sensor reading was further validated against an intake buffer volume pressure sensor. To precisely determine the TDC position, raw pressure data were processed by an in-house combustion analyzer developed in LabVIEW, which incorporates various inputs including encoder resolution, encoder offset, pegging timing, pegging pressure, and the specific CFR engine geometry.

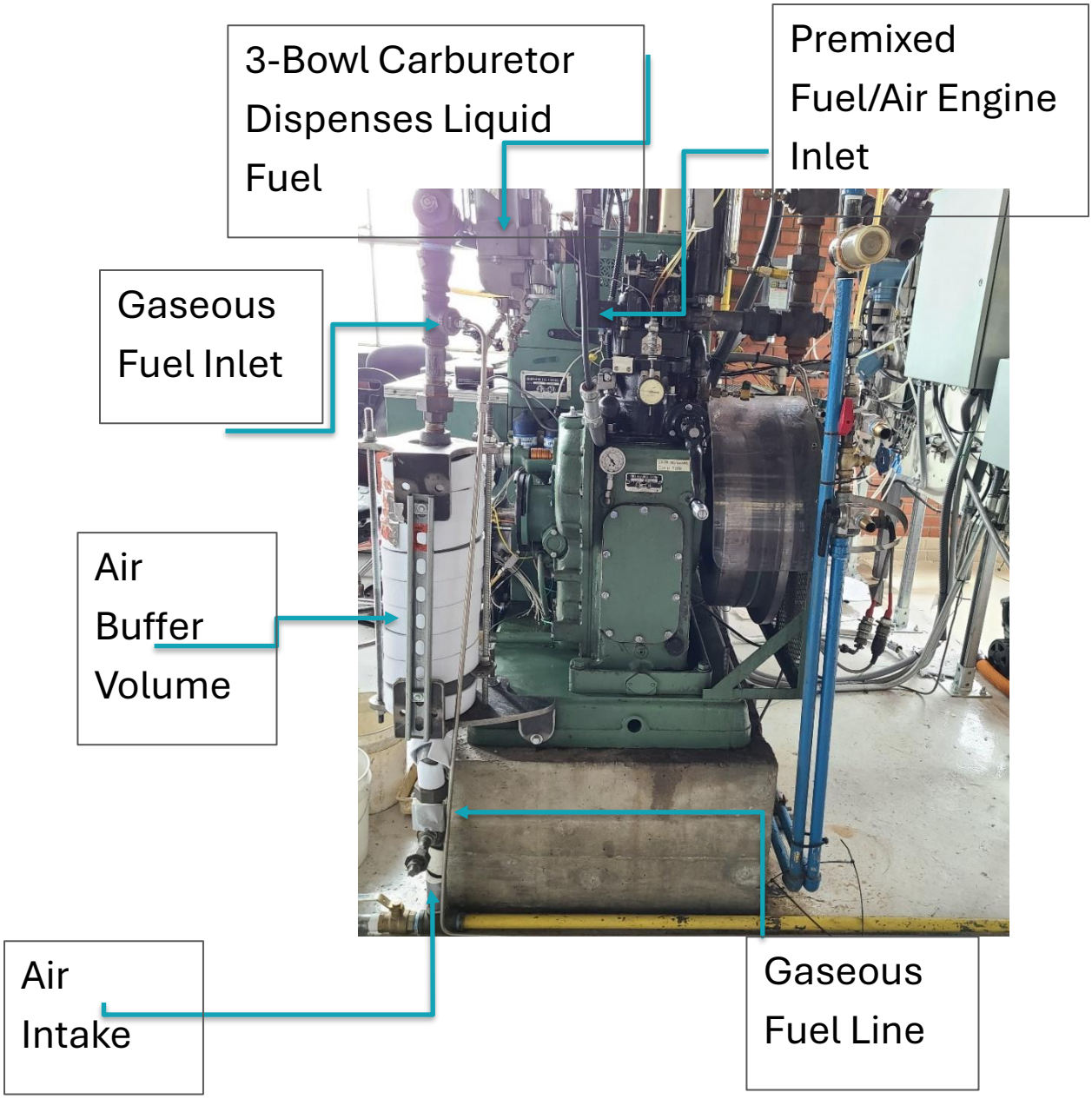

Figure 2.5. A picture showing a side view of the CFR engine cylinder head and hardware modification locations to run both ssssliquid and gaseous fuels.

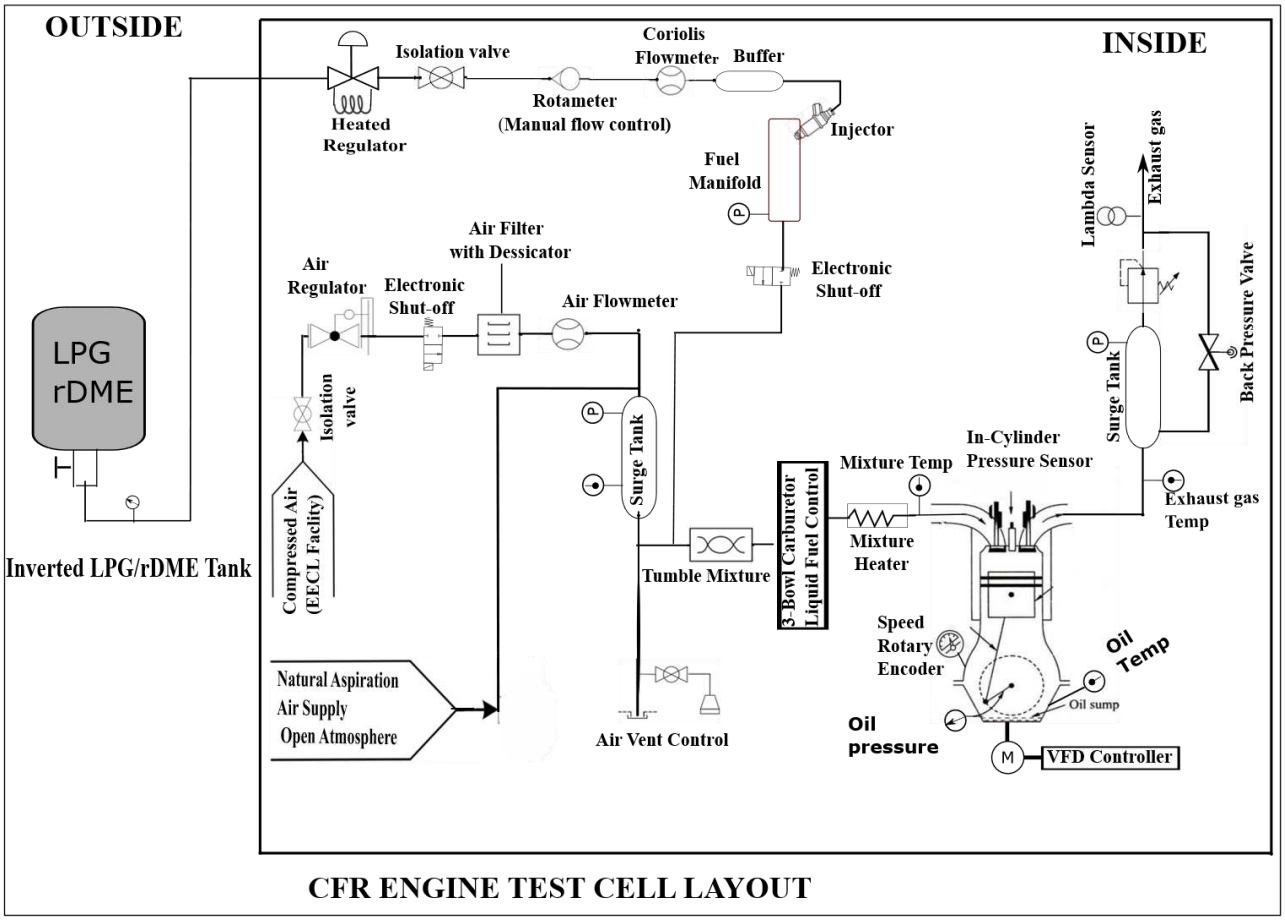

Figure 2.6. Schematic overview of CFR engine test cell

To ensure accurate engine speed controls, a Yaskawa U1000 regenerative variable frequency drive (VFD) was installed. The VFD can maintain engine speeds between 600 and 1200 RPM permitting speed operation of both RON and MON allowing the utilization of the same engine for testing. To capture the position of the crankshaft, a BEI model L25 optical encoder was installed. This digital rotary encoder can provide the crank angle position with a tenth of a degree resolution. To measure the air-fuel ratio present in the engine, a wide-band LSU 4.9 lambda sensor was installed downstream of the exhaust buffer volume. The lambda sensor has an operating range of 0.65 to infinity while working with exhaust temperatures up to 930°C. To monitor the fuel flow

rate, a Micromotion CMF series Coriolis mass flow meter was installed. Combustion phasing was controlled using a Woodward Large Engine Control Module (LECM) working in tandem with developed LabVIEW VIs to achieve real-time CFR engine control, monitoring, and performance analysis.

2.3.1 Knock Classification

For MON or RON tests, ASTM standards stipulate that fuel knock intensity is classified using a detonation meter. This meter receives signals from a magnetostrictive transducer—a detonation pick-up threaded into the engine cylinder—which is exposed to combustion pressures. The transducer functions by converting rapid pressure changes, characteristic of knock oscillations, into a signal proportional to the rate of cylinder pressure change. The resulting knock intensity, ranging from 0-100, is then displayed on a knock meter [63, 64]. In contrast, modern in-cylinder pressure transducers are typically quartz sensors that utilize the piezoelectric effect. By generating an electrical charge when deformed, these sensors directly measure absolute in-cylinder pressure over time, enabling them to accurately detect and record the full waveform of high-frequency pressure oscillations observed during knock. This capability offers higher precision and more detailed pressure data than detonation meters. The ASTM standard has updated the analog hardware used for the detonation meter and introduced a digital detonation meter that can be implemented in its place. The CFR engine utilized for this experimental study was upgraded with a new knock measurement system, deviating from the ASTM standard offering vast upgrades over the detonation meter approach. Here a Kistler 6061B water cooled piezoelectric pressure transducer is utilized instead for in-cylinder pressure measurements with the aid of a rotary encoder to provide high resolution pressure history that is analyzed in real time to obtain insight into the

combustion process while also providing quantification of the knocking event taking place in the cylinder [63, 64].

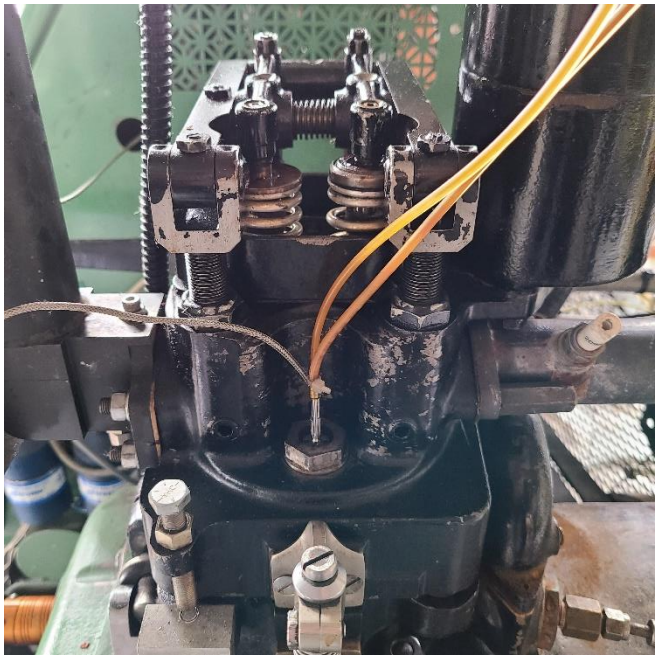

Figure 2.7. Kistler 6061B In-Cylinder Pressure Transducer

To evaluate the knock intensity using dynamic in-cylinder pressure, it is required to know the operating speed and the natural frequency of the engine. Using in-house built LabVIEW code, a bandpass filter is then applied to the pressure data corresponding to the average engine speed to remove the engine operating frequency thus exposing pressure data distortion outside of normal operating parameters allowing for the determination of the high frequencies of pressure oscillations that are caused by end-gas autoignition. A fast Fourier transform (FFT) technique is applied to the bandpass filtered pressure data to obtain the power spectrum of the signal [12, 65-67]. A time-averaged approach is implemented to establish a knock index which provides an objective and repeatable criterion for comparison between the overall knock intensities of different fuels when under the same operating conditions. Bayliff terms a knock integral which can be described as the area under the curve bounded by the FFT power spectrum spike magnitudes over

a set number of combustion cycles [65, 66]. For this study, a 200 consecutive cycle interval was chosen to sum the FFT power spectrum amplitudes (in kPa^2). The FFT power amplitude is displayed in real-time through the LabVIEW software and is logged for post processing. The knock integral provides a useful tool for the determination of the intensity of knock during engine operation.

$$KI = Area_{Bounded} = \sum_{i=0}^{n} \{(i+1)\text{-}i\}\{KL(i+1) + KL(i)\}/2$$

where:

n= number of combustion cycles in a data set
KL(x)= knock level magnitude at a given combustion cycle, x (5)

2.3.2 LPG/rDME and Primary Reference Fuels

For this study, the gaseous fuel blends of LPG and rDME were supplied by Oberon Fuels in standard Manchester tanks. Oberon provided an internal composition analysis utilizing the ASTM D2163 test procedure, these results are displayed in Table 2.5. The blends were formulated to achieve 5% part rDME blend intervals within a commercial LPG. Although the resulting blends did not precisely match the targeted blend concentrations, the intended ratios are retained for consistency and ease of reference throughout the paper. The rDME blends contained residual methanol and water due to the methanol dehydration production process but these trace levels were expected to play little to no role in impacting the fuel reactivity.

2.3.3 Fuel Composition Analysis

The fuel samples compared in this study consisted primarily of rDME and LPG, but contained small amounts of ethane, propylene, butane, methanol, and water. The fuel compositions were evaluated in a HP 5890 series ii gas chromatograph to determine how the samples compared to the certificate of analysis (COA) provided by Oberon. During engine testing, the tanks were

inverted allowing the fuel to be pulled from the liquid phase to prevent preferential evaporation of the constituent species. The fuel samples utilized for gas chromatograph testing were collected using the same inversion method. The fuel sample compositions were measured both before and after engine operation using the same instrument. At both conditions, the fuel sample compositions were verified and showed agreement with the COA ensuring the blend properties remained relatively consistent over testing. The GC results comparing the mass fractions are shared in the chapter 4.

The ASTM standard defines isooctane as the upper limit of PRFs at 100 while n-heptane is used to represent the zero end of the PRF scale. The standard then uses blends of both isooctane and n-heptane to create different octane numbers from 0-100. The isooctane and n-heptane used for this study was HPLC grade and provided by Fisher Scientific and Oakwood Chemical. Gas chromatograph analysis was performed on both isooctane and n-heptane finding that both are greater than 99.75% by volume pure. For octane numbers over 100, a defined mixture of toluene, isooctane, and n-heptane can be implemented as PRFs [63, 64, 68]. To calculate a fuel sample's octane number, the knock intensity of the sample fuel and the knock intensity of both the PRFs that were deployed to bracket the sample fuel are required, then using equation 1 the sample fuel's octane number can be determined [63, 64].

$$O.N._S = O.N._{LRF} + \left(\frac{K.I._{LRF} - K.I._S}{K.I._{LRF} - K.I._{HRF}}\right)(O.N._{HRF} - O.N._{LRF}) \quad (6)$$

Where:

$O.N._S$ = Octane Number of Sample fuel

$O.N._{LRF}$ = Octane Number of Lower Reference fuel

$O.N._{HRF}$ = Octane Number of Higher Reference fuel

$K.I._S$ = Knock Intensity of Sample fuel

$K.I._{LRF}$ = Knock Intensity of Lower Reference fuel

$K.I._{HRF}$ = Knock Intensity of Higher Reference fuel

Table 2.5
Chemical Composition of Test fuels (Mass Fraction %)

Sample Fuel	**Ethane**	**Propane**	**Propene**	**rDME**	**Butane**	**Methanol**	**Water**
100% LPG	0.32	96.99	0.025	0	2.65	0	0
5% rDME	1.197	91.93	.086	5.116	1.653	0.006	0.012
10% rDME	1.481	88.607	0.23	8.294	1.36	0.015	0.013
15% rDME	1.487	82.851	0.35	13.88	1.394	0.025	0.013
20% rDME	1.434	78.159	0.44	18.478	1.455	0.024	0.011
30% rDME	0.837	67.879	0.037	30.081	1.107	0.038	0.021

2.3.4 Engine Standardization

Prior to rating the sample fuels, the engine was found to be under compliance with the ASTM standards – through completion of the timing check procedure, the valve lift check procedure, and cylinder height indexing steps - considering it fit for octane number rating. A "Fit-for-use" procedure that uses Toluene Standardization Fuels (TSFs) of known accepted reference value [63, 64] was completed. A TSF representing 96.6 ± 1.2 was bracketed against PRFs of MON

96 and 98 to verify the engine is rating properly. The TSF blend produced a MON of 97.33 falling within the range of the rating tolerance of the TSF establishing engine compliance. The TSF blend rating was achieved without the requirement for intake air temperature tuning. Figure 2.8 illustrates how the FFT magnitudes vary over the recorded 1000 cycle interval for both the test fuel displayed in black and the known PRFs shown in red and blue.

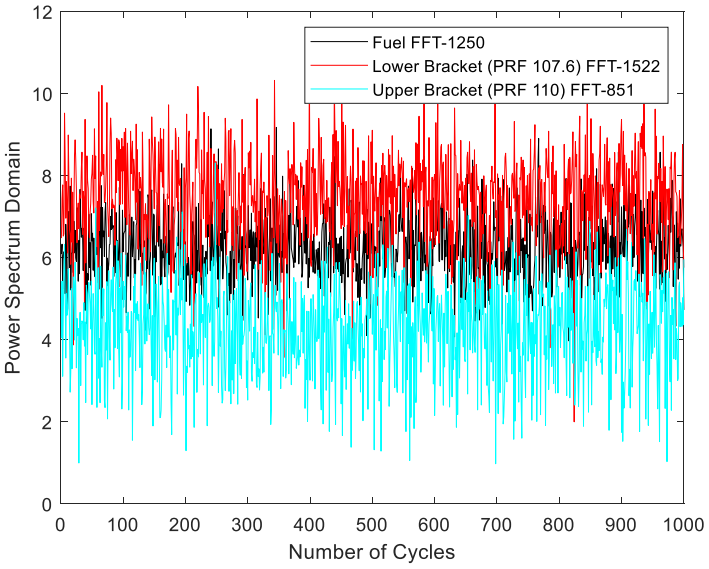

Figure 2.8. FFT magnitudes recorded over 1000 cycles for the three test fuels, rDME/LPG mixture and corresponding PRFs.

2.3.5 Engine Test Procedure

The ASTM standards do not outline a test method for gaseous fuels, thus requiring the development of a new test procedure. The ASTM standards relate their octane number measurements back to a set of guide tables through the dial indicator which reads the cylinder height and has a determined value for different PRFs. For liquid fuels, the ASTM standards classify a standard knock intensity to be replicated when testing other fuel samples. For initial testing, the

guide tables were implemented, and they produced accurate rating results but using the guide tables and their prescribed compression ratios were not producing enough knock to distinguish well between fuels as the FFT method produced a very small scale between test fuels requiring the standard testing method to be modified. For this study, the sample fuels were brought to a medium knock intensity defined by Bayliff [65, 66]. Bayliff determined that FFT values of 150 kPa^2 represent the threshold where light knock occurs, transitioning to medium knock around an FFT value of 310 kPa^2 while heavy knock occurs with an FFT value above 1800 kPa^2.

The gaseous sample fuel is introduced first to the engine, following a method similar to the ASTM standards fuel equilibrium level bracketing procedure, the sample fuel's air-fuel-ratio (AFR) is changed to determine the ratio that produces the maximum knock intensity or a maximum FFT reading. Next, if the AFR and current compression ratio do not produce a medium knock signal, the compression ratio is increased until it is in the prescribed FFT range (310-1800 kPa^2). Once medium knock of the sample fuel is obtained, the combustion and in-cylinder pressure data were logged at 54kHz ($1/10^{th}$ degree resolution) for 1000 cycles (2-3 min). Other parameters were logged at a slower rate for the same 3-minute duration. Keeping the compression ratio constant, the PRFs are evaluated in the engine following the same procedure conducted for the gaseous fuel sample, where the AFR is changed to determine the maximum knock intensity for the PRF. If the PRFs do not bracket the sample fuel, a new PRF is tested until the sample fuel's FFT values are bracketed. Using the FFT values obtained from the test fuel and two corresponding PRFs, the octane number can be calculated following equation 1.

Nominal repeat tests were conducted for every test fuel in order to determine the repeatability of the knock intensity metric (FFT measurements) which is the primary contributing factor to determine the MON and RON. Repeatability is used to assign uncertainty to determine

the range of MON and RON. Only repeatability is considered in the uncertainty calculations as system uncertainty was determined using the root summation of squares (RSS) method producing a small value of ± 0.04 compared to 0.2 determined from the repeatability. The highest determined repeatability of 0.2 is assigned to the MON and RON values, calculated by examining the standard deviation of the FFT reading over three to five repeated measurements of 1000 engine cycles (3000-5000 cycles). The standard deviation is used to calculate the observed FFT range which are then used in equation 1 to determine the range for both MON and RONs.

2.4 High Pressure Spray Chamber Set-up

Further analysis was implemented to evaluate the compatibility of rDME/LPG blends with current GDI systems by studying their spray characteristics through high-speed schlieren imaging. High-speed schlieren imaging experiments were conducted for 100% LPG, 30%DME/70 LPG, and 100% DME. Schlieren imaging is a well-established imaging technique that can provide a global image of both the liquid and vapor regions of the spray allowing us to visualize gradients in the density field created by inhomogeneities in the refractive index.

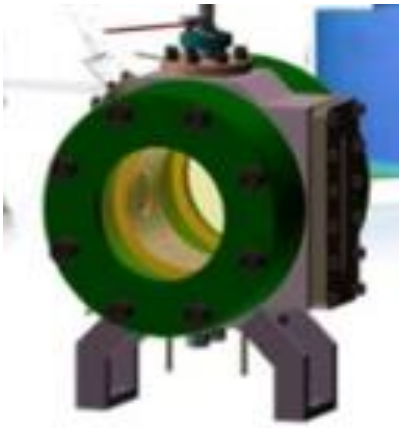

Figure 2.9. Isometric 3D rendering of High pressure spray chamber (HPSC) and fuel injector location

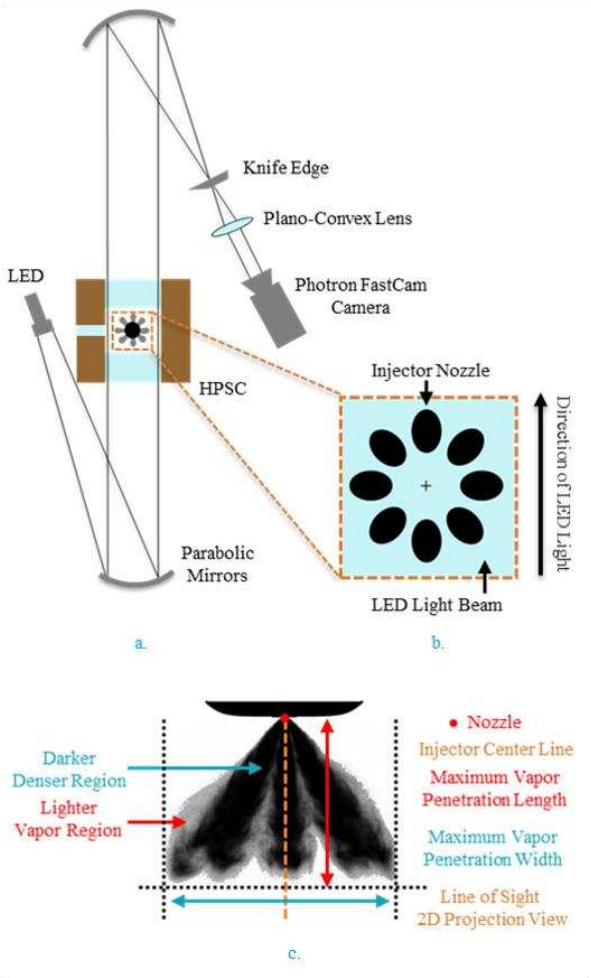

Figure 2.10. (a) Schematic of the top-view of Schlieren imaging setup, (b) Spray-G injector nozzle-alignment relative to the LED light, and (c) resulting Schlieren spray image, features, and nomenclature.

The previous work of author Sharma [58] established the high-pressure spray facility shown in Figures 2.9 and 2.10 while also developing advanced diagnostic techniques to compensate for limitations obtained with Schlieren imaging of multi-phase fuels such as LPG. A detailed system diagram for the set-up of the high-pressure spray chamber can be viewed in Sharma's work [69]. To study the axial vapor-liquid penetration length, width, and the penetration rate of the spray, a chamber pressure sweep from atmospheric to 10 bar gage pressure was conducted for all of the fuel types. For the experiments, a symmetric gasoline direct injection (GDI) 8-hole SprayG injector

[59] was utilized for each fuel while the injector current profile, fuel temperature, chamber temperature, 11ms injection duration, and an injection pressure of 172 bar were all kept constant. A 200-lumen white LED was collimated through the high-pressure spray chamber by a 150 mm parabolic mirror of 750 mm focal length and received by an identical parabolic mirror placed in a z-type configuration. A knife-edge was used as the Schlieren cut-off at the focal point of the converging mirror to amplify the contrast and intensity variations. The images were finally sized with a 50 mm plano-convex achromatic lens of 150 mm focal length and acquired using a Photron FASTCAM SA5 high-speed camera. The corresponding imaging frequency was set to 30,000 frames per second, resulting with a spatial image resolution of 298 μm/px capturing 376 x 640-pixel images [58]. All images were processed with an in-house MATLAB code developed by Sharma [69].

2.5 LPG/DME X15 Experimental Methods

Utilizing the experimental test cell and PFI injector configuration detailed in Sections 2.1 and 2.2, LPG/DME blends ranging from 0–30% DME by mass were evaluated in a Cummins X15 medium-to-heavy-duty spark-ignited engine. These experiments were designed to quantify the effects of DME addition on heavy-duty SI operation and to determine if DME/LPG blending provides a viable performance pathway compared to traditional natural gas (NG) and LPG benchmarks. Throughout the testing, a constant engine speed of 900 rpm and an IMAT of 35°C were maintained, and all experiments were conducted at a stoichiometric equivalence ratio (phi = 1.0). The engine was equipped with 9.3:1 nominal CR pistons; however, for this study, the original cylinder liners were replaced with a specialized version that did not feature an Anti-Polishing Ring (APR). This hardware modification reduced the total clearance volume, resulting in an effective

compression ratio of 10:1 for the duration of the experimental campaign. The experimental design utilized a CA50 sweep to characterize the combustion phasing sensitivity of 100% LPG, 5%, 10%, 15%, 20%, and 30% DME blends, alongside an industry-standard natural gas baseline. Due to the varying chemical reactivity of these fuels, the test matrix was divided into two load levels based on IMAP. A high-load condition at 120 kPa IMAP achieved a BMEP range of 10–11.7 bar for the natural gas, 100% LPG, and DME blends up to 20%. However, due to the high knock sensitivity of the 30% DME blend, a lower load condition achieving 6.5–7.6 bar BMEP was utilized at 90 kPa IMAP. To ensure parity and allow for direct performance comparisons, a secondary 20% DME test and an additional natural gas baseline were repeated at this 90 kPa condition. For each blend ratio, the CA50 sweep targeted timings from 16° aTDC to 4° aTDC to evaluate the trade-offs between efficiency and engine stability. During these sweeps, combustion phasing was advanced until the 4° aTDC target was reached or the fuel hit its knock limit. This systematic approach allowed for the identification of the knock-constrained operating envelope for the increasingly reactive DME blends, providing a clear comparison of the displacement-limited performance of each fuel mixture.

2.6 *LPG/DME 0D, 1D, and 3D CONVERGE and Chemkin Simulations*

This section details the computational framework employed for the 0D, 1D, and 3D simulations of LPG/DME blends. Given the computational expense associated with high-fidelity chemical kinetic mechanisms such as RC3 and Aramco 3.0, these were deemed unsuitable for 3D engine simulations in the CONVERGE environment. Consequently, this work necessitated the development of a reduced chemical kinetic mechanism tailored for engine-scale applications. The ALPINE-DME 158 mechanism was developed by integrating the UCSD DME sub-mechanism

comprising 14 reactions involving 5 species into the established CSU ALPINE 153 base mechanism [51, 52]. Table 2.6 summarizes the specific reaction and species additions that define the ALPINE-DME 158 framework.

Table 2.6. UCSD DME Sub Mechanism Reactions and Species added to ALPINE 153

Reactions	**Species**
CH3OCH3(+M) =CH3O+CH3(+M)	CH3OCH3
CH3OCH3+O2=CH3OCH2+HO2	CH3OCH2
CH3OCH3+OH=CH3OCH2+H2O	CH3OCH2O2
CH3OCH3+CH3=CH3OCH2+CH4	CH2OCH2O2H
CH3OCH3+H=CH3OCH2+H2	HO2CH2OCHO
CH3OCH3+HO2=CH3OCH2+H2O2	
CH3OCH2=CH2O+CH3	
CH3OCH2+O2=CH2O+CH2O+OH	
CH3OCH2+O2=CH3OCH2O2	
CH3OCH2O2+CH3OCH2O2=O2+2CH3O+2CH2O	
CH3OCH2O2=CH2OCH2O2H	
CH2OCH2O2H=CH2O+CH2O+OH	
CH2OCH2O2H+O2<=>HO2CH2OCHO+OH	
HO2CH2OCHO=CH2O+CO2+OH+H	

The predictive accuracy of ALPINE-DME 158 was assessed through a rigorous multi-stage validation study, comparing simulated performance against experimental ignition delay times (IDT) and laminar flame speeds. Both CONVERGE [48] and the ANSYS Chemkin-Pro software suite [70] were utilized as reaction kinetic solvers for these evaluations. 0-D kinetic studies were conducted using a closed, constant-volume, homogeneous batch reactor with adiabatic, chemically inert walls to model the pressure conditions reported in the RCM data by Dames et al. [40]. For these simulations, IDT was defined as the time corresponding to the peak OH radical concentration.

Additionally, laminar flame speeds were calculated using an adiabatic, freely propagating flame model under state conditions consistent with the experimental data of Vasu et al. [71]. For both 0D and 1D simulations, the RC3, UCSD, USC, LLNL, and combined USC/LLNL mechanisms were simulated alongside ALPINE-DME 158 to provide a direct comparative assessment of predictive capabilities against established literature models. Following this kinetic validation, ALPINE-DME 158 was implemented in 3D CONVERGE simulations. The solver configuration relied on the foundational numerical methods described in Section 2.2, with fuel mass fractions and thermophysical properties updated to reflect the specific LPG/DME blend ratios investigated in this work.

CHAPTER 3 - CFD MODELING OF AN LPG MEDIUM TO HEAVY DUTY X15 SPARK IGNITED ENGINE

3.1 PFI and DI Engine Performance

This section presents the results of LPG combustion in a heavy-duty spark-ignited (SI) engine, comparing performance differences between two fuel injection strategies: Port Fuel Injection (PFI) and Direct Injection (DI). Initial LPG engine testing, previously conducted by Fosudo et al. [45] is examined. Investigating the performance impacts of PFI and DI by quantifying operational differences in both in-cylinder pressure traces and Apparent Heat Release Rate (AHRR) curves across a Start of Injection (SOI) timing sweep, ranging from early injections at 360° before Top Dead Center (bTDC) to late timings at 120° bTDC. Figure 3.1 details the impact of SOI timing on AHRR curves for both injection strategies. The experimental engine data indicates that the PFI method consistently provided a stable AHRR across all operating conditions, presenting a clear contrast to DI operation. DI strategies demonstrated a significantly greater impact of SOI timing on AHRR, leading to substantial variations in heat release between operating conditions. The earliest injection timing (360° bTDC) produced a higher peak and shorter heat release duration compared to later timings (330° bTDC and 300° bTDC), where the heat release peak was drastically reduced and the duration increased, indicating less controllable combustion conditions. This AHRR behavior persists until late SOI timings of 150° bTDC and 120° bTDC are reached, where a similar trend to SOI 360° bTDC is observed with a decreased AHRR duration. Additionally, these later injection timings (120° and 150° bTDC) resulted in an increased peak heat release rate, achieving the maximum AHRR at SOI 150° bTDC, suggesting more favorable LPG combustion under this operating condition.

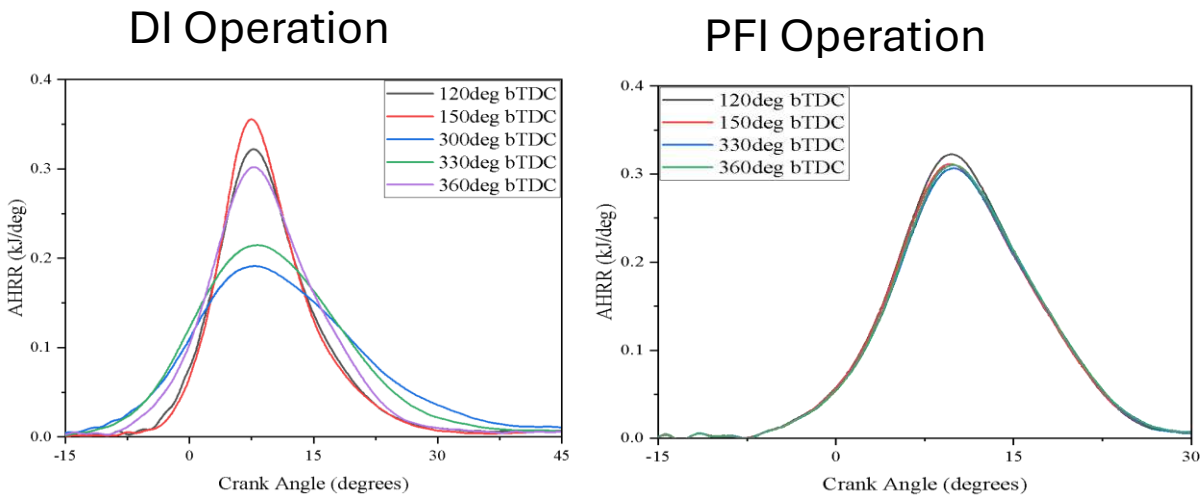

Figure 3.1. PFI vs DI Operational differences between AHRR curves for baseline CR 9.3

This behavior is further substantiated by Fosudo et al. [45], who crucially plotted the BTE as well as the COV of IMEP for selected SOI timings in PFI mode [11] and DI [45]. For Direct Injection (DI) operation, moving from early to late injections, the COV initially remains within a controllable range at early injection timings (360° bTDC). However, as the injection timing is retarded closer to Top Dead Center (TDC), the COV immediately increases beyond the stable engine operation limit, typically set at a COV value of 3. Following this increase, the engine demonstrated stable operating again at an injection timing of 150° bTDC [45]. Figure 3.2 compares the net IMEP trends for the DI and PFI configuration for the selected SOI timings and also demonstrates the attendant engine stability behavior at the baseline compression ratio of 9.3. For this DI configuration, the $IMEP_{net}$ increased steadily from late injection timings with the highest value observed at 360 deg bTDC SOI timing. In contrast, the highest $IMEP_{net}$ for the PFI mode was achieved at the late SOI timing 120 deg bTDC as the engine consistently achieved a COV_{imep} less than 3% across all injection timings. This contrasting IMEP behavior is likely due to the mixing time which is maximized at early SOI timings for the DI operation and at late SOI timings

for the PFI operation as the charge sits in the intake manifold all through the compression, power and exhaust strokes since the intake valve is already closed. To gain further insight into the observed engine performance differences arising from these two injection techniques, an extensive simulation campaign was conducted, and the results are presented in the subsequent section.

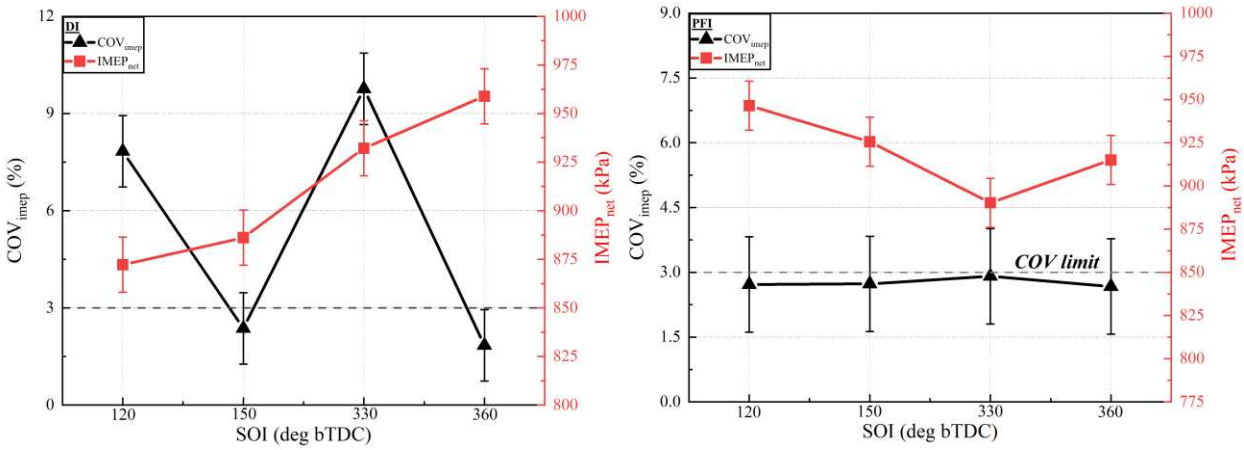

Figure 3.2. COVimep and IMEPnet vs Start of Injection timing for the heavy-duty LPG in PFI and DI mode at naturally aspirated conditions, 9.3 compression ratio, 1200RPM and an equivalence ratio of 1.

3.2 Numerical Investigation: PFI and DI 3D Simulations

To accurately predict LPG flashing behavior, a model was developed utilizing previous work done in collaboration with Colorado State University (CSU) and Argonne National Laboratory leveraging Argonne's previous spray work and experience. [72-75]. This prior research, conducted for a Department of Energy (DOE) project, focused on determining LPG spray behavior for engine simulations under medium and heavy-duty load conditions. Initially, baseline experimental test conditions from Fosudo et al. [45] were simulated in CONVERGE to validate if the ALPINE 153 chemical mechanism, coupled with the LPG spray model could accurately predict engine behavior. The results from initial HPSC simulations and experiments are presented in

Figure 3.3, providing a comparison of the extreme flash-boiling parameters defined in Section 2.2. To comprehensively characterize the spray, two diagnostic techniques were employed: Schlieren imaging was utilized to track the entire development of the gaseous fuel vaporization and plume expansion, while Mie-scattering was used to isolate the liquid penetration observed during the initial injection event. As shown in Figure 3.3, there is high qualitative agreement between the CFD spray model and the experimental visualizations for both the vapor and liquid phases under flashing conditions. This correlation is further quantified in Figure 3.4, which displays the graphical trend of penetration length over time.

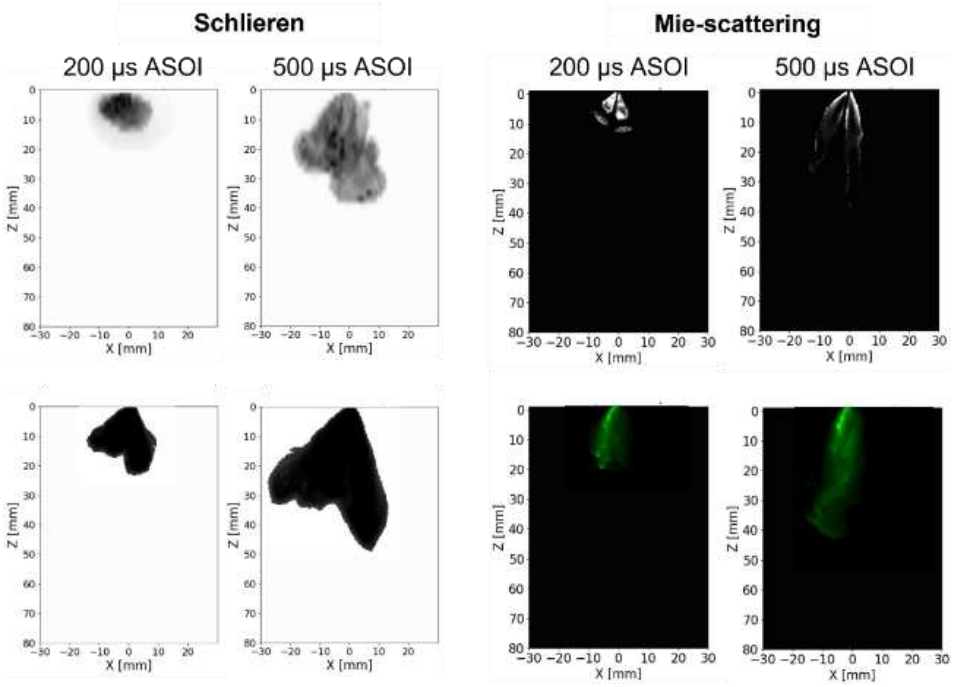

Figure 3.3. Results for the optimized 5-hole injector shown for "flashing" conditions for (top) CFD and (bottom) experiments.

At low chamber pressures and temperatures, the model slightly under-predicts the vapor penetration length but successfully captures the slope and trend of the experimental data. Conversely, at moderate chamber pressures (near 4 bar) and elevated temperatures (363 K), the

vapor penetration is over-predicted by the spray model; however, it remains consistent in capturing the overall increase in vaporization penetration as time progresses. Other studies conducted by Argonne [72-25] and Manava et al. [58] highlight the spray model's robust capabilities across various chamber pressures and temperatures. Overall, the model accurately follows the experimental vapor penetration length trends during the initial 1200 µs. This validates the spray model's ability to resolve the rapid phase change and high-velocity expansion characteristic of LPG flash-boiling, while providing necessary context for the specific conditions under which the model exhibits minor over- or under-prediction behavior.

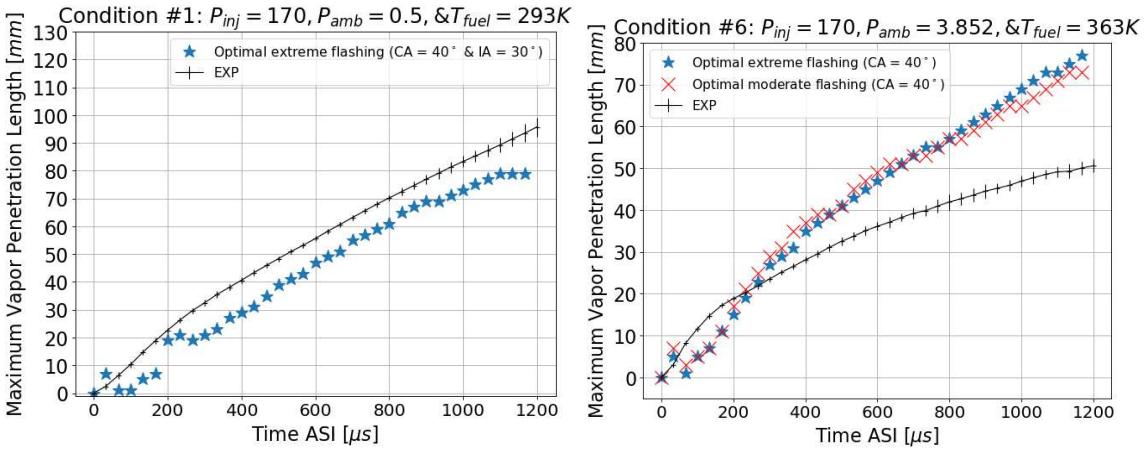

Figure 3.4. Vapor penetration at two experimental HPSC conditions representing high flahing behavior.

With the development of the extreme and nonextreme flash parameters for the KH-RT model described in section 2.2, and the verfication of these parameters carried out through HPSC experiemnts and simulatioins, 3D CONVERGE simulations were conducted to determine the valididy of these parameters in internal combustion engine applications. Both the extreme and non-extreme parameters were chosen to observe the sensitivity of the spray model on combusiton during late (-150° bTDC) and early injection timings (-340° bTDC) for DI engine operation. Figure

3.5 displays the initial results for the early injection timing of -340° bTDC. At this condition, the extensive residence time available for fuel-air interaction promotes effective mixing, resulting in a largely homogeneous mixture at the spark plug for both injection strategies. Consequently, both the extreme and non-extreme spray models generate cylinder pressure traces that fall well within the experimental 1000-cycle engine envelope. This agreement validates that at early injection timings, the global engine performance is less sensitive to the specific atomization sub-model, as the increased mixing time compensates for variations in initial spray development.

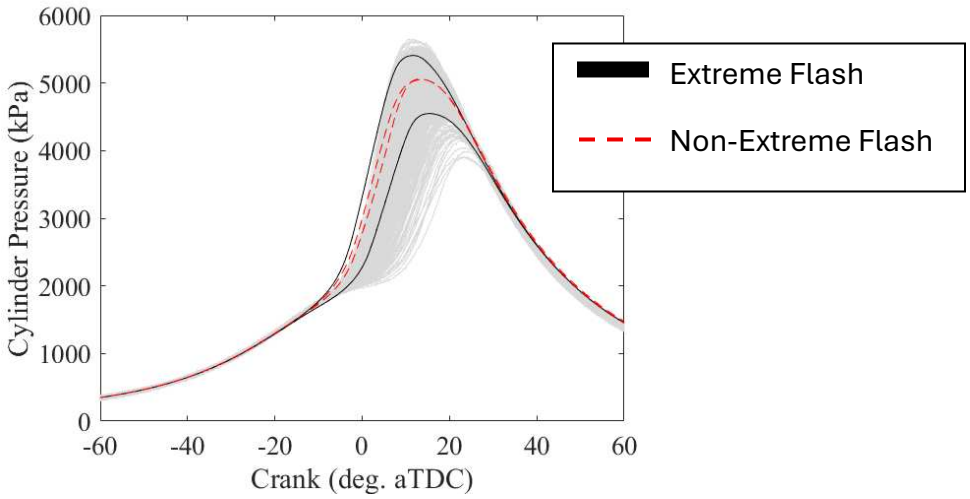

Figure 3.5. Extreme vs nonextreme flash parameters for early injection timing -340° bTDC. at baseline 9.3 CR

Figure 3.6 presents the combustion results for the late injection timing of -150° bTDC. Unlike the early injection case, engine performance at this timing is significantly affected by the choice of spray parameters. Under these compressed mixing timescales, the extreme flash spray parameters were the only conditions capable of achieving successful combustion. The non-extreme flash spray model failed to properly resolve the necessary atomization and liquid spray breakup. This resulted in 3D CONVERGE simulations that failed to ignite due to excessive liquid

impingement and severe wall wetting occurring during the late injection window. The reduced residence time inherent in this strategy exposed the limitations of the non-extreme model, as it could not predict the rapid phase change required to form a combustible mixture before the spark event. With the deficiencies of the non-extreme model identified, the extreme flash parameters were selected for the remainder of the DI engine simulations. This selection is justified by the model's demonstrated ability to accurately predict engine performance across the full operational spectrum, validating its use for both early and late DI injection strategies.

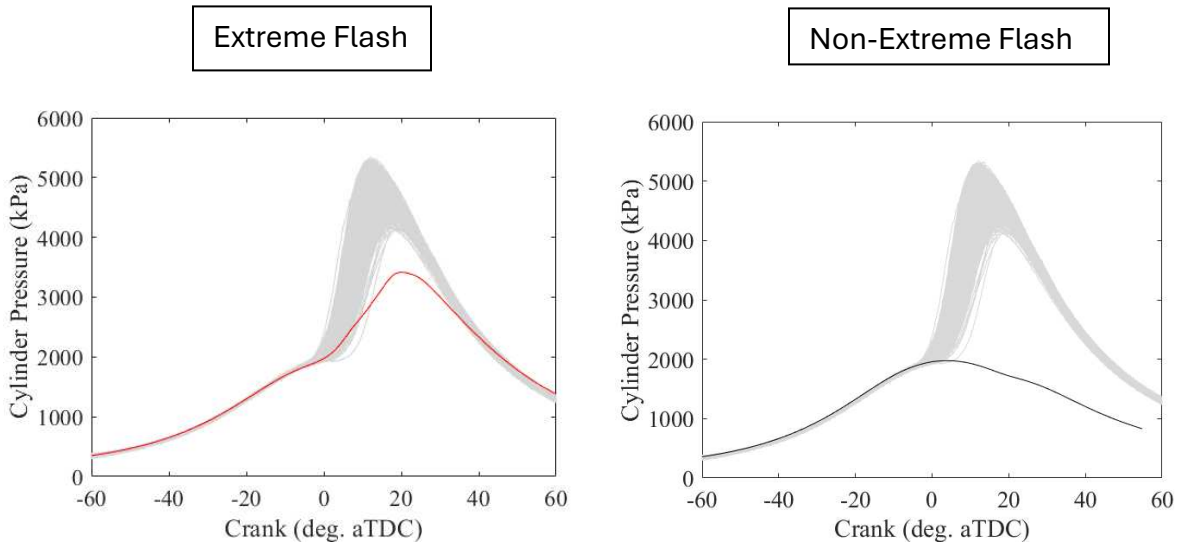

Figure 3.6. Extreme vs nonextreme flash parameters for late injection timing -150 at baseline 9.3 CR

Figure 3.7 examines these initial baseline simulations for both Port Fuel Injection (PFI) and Direct Injection (DI) techniques. The CONVERGE 3D CFD in-cylinder pressure results are depicted by the red and black traces, while 1000 cycles of experimental pressure data are shown in light grey. The simulation results for both injection operations fall within the 1000-cycle

experimental envelope, demonstrating excellent agreement between the model and experimental data.

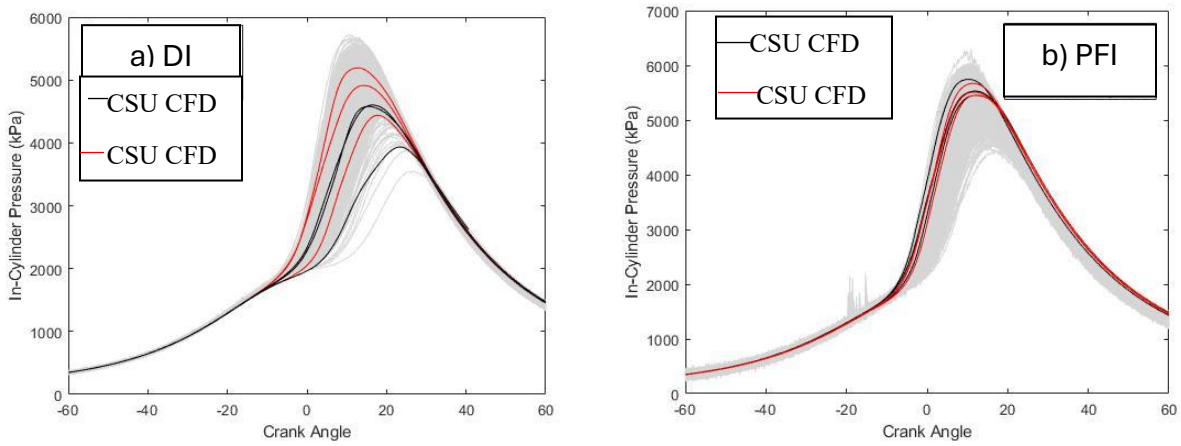

Figure 3.7. Baseline PFI and DI 3D CONVERGE simulations vs 1000 Experimental Cycles at naturally aspirated conditions, 9.3 compression ratio, 1200RPM and an equivalence ratio of 1.

The DI simulations, represented by the red and black traces in Figure 3.7a, accurately captured engine operation across the entire experimental data range, demonstrating the model's capability to predict observed cycle-to-cycle variation. With the model validated against experimental data, a simulation study was conducted in CONVERGE to examine the effect of injection timing (SOI) on DI operation. Figure 3.8 presents the results of this SOI sweep, illustrating the equivalence ratio distribution near the spark plug as a function of injection timing. The CONVERGE simulations indicate that for DI operation, injection timing significantly influences the in-cylinder mixture distribution, which ultimately impacts engine performance. The most uniform homogeneous mixture was achieved at SOI 340, where the mixture around the spark plug was slightly rich, with an equivalence ratio near 1.1.

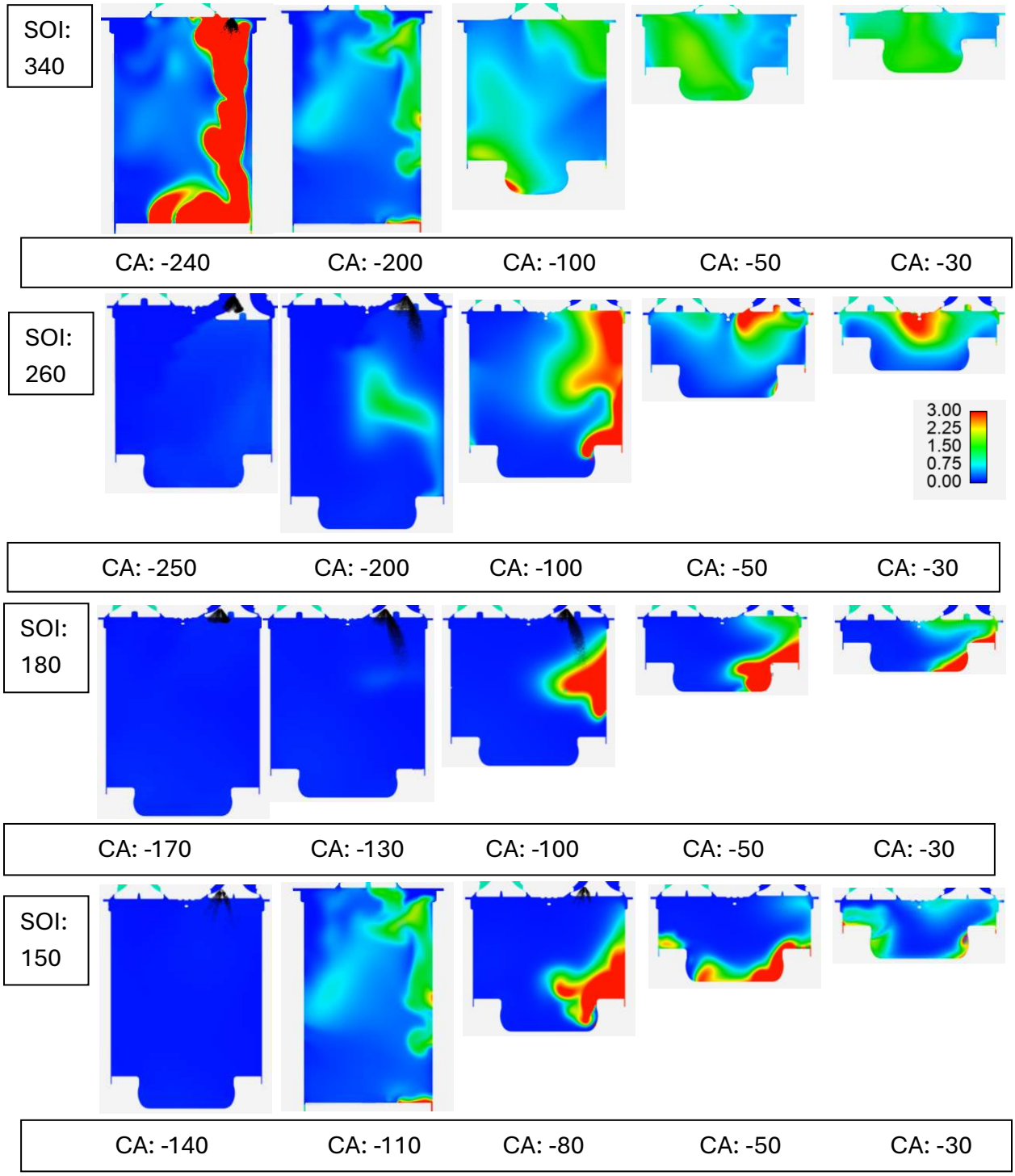

Figure 3.8. Mixture Distribution at different SOI's for DI operation at CR 9.3

In contrast, at SOI 260, which falls outside the controllable experimental engine operation, a stratified mixture with four distinct equivalence ratio zones (Figure 3.8) was generated. For DI

operation, a stratified mixture is often preferred due to its potential for improved fuel efficiency with leaner ignition and reduced emissions. However, despite the potential for enhanced performance and favorable combustion at SOI 260 due to stratification, this operational point, as reported by Fosudo et al [45] and shown in Figure 3.9, exceeds the coefficient of variation (COV) limit. Figure 3.8 further indicates that at SOI 260, the equivalence ratio around the spark plug is excessively rich, exceeding propane's upper extinction limit, thereby hindering combustion and flame propagation throughout the cylinder.

For SOI 260 to remain operational within the COV limit, the injected fuel mass would need to be reduced. Reducing the fuel quantity would then ensure an equivalence ratio below the extinction limit as the intake air and piston velocity at this injection timing would still generate a stratified mixture. Examining the SOI 180 simulation reveals that neither a stratified nor a homogeneous mixture is formed at the spark plug. Instead, two rich pockets are observed: one at the bottom of the piston bowl and another near the crevice volume, both situated on the cylinder's right side. These rich pockets at SOI 180 create in-cylinder conditions unfavorable for combustion, thus explaining the COV exceeding the limit at this DI operational point.

In contrast, at SOI 150, the engine COV remains stable, even outperforming PFI at comparable injection timings [45]. CONVERGE 3D simulations demonstrate that the mixture formation near the spark timing (30° bTDC) at SOI 150 differs significantly from the SOI 180 and SOI 260 cases. At SOI 150, the fuel-air mixture is primarily distributed along the cylinder walls, concentrated at the periphery of the piston bowl and the entrance to the crevice volumes. As the piston approaches TDC, the mixture localized at the bottom and sides of the bowl is transported toward the spark plug. This motion facilitates a more favorable equivalence ratio at the spark gap,

avoiding the excessively rich conditions and rich zones localized at the bottom of the piston bowl previously observed at SOI 180 and SOI 260.

These distinct mixture distributions elucidate why experimental results showed a performance increase at this injection timing, surpassing all other strategies except for the early injection at SOI 340. This analysis further clarifies the discrepancies in knock and end-gas autoignition (EGAI) reported by Fosudo et al. [45], who found that late DI strategies resulted in an increased knock ripple sum that surpassed the knock limit. In contrast, early DI remained below the knock threshold across all operational CA50 values. The current simulations demonstrate that late DI results in localized rich pockets within the piston bowl and cylinder periphery. These regions promote an environment conducive to EGAI as the flame front propagates from the spark plug, whereas the early injection (SOI 340) achieves a highly homogeneous mixture that suppresses autoignition tendencies.

The observed differences across SOI cases suggest that factors beyond maximized mixing time influence mixture formation and stable engine operation. Additional engine parameters that could affect in-cylinder mixture distribution include variations in intake velocity dependent on injection timing, cylinder motion (swirl, tumble, and squish effects), injector location, and spray pattern. The effects of some of these parameters will be further investigated in the next section, which examines how increasing the compression ratio can alter mixture formation.

3.3 Effect of Compression Ratio on Mixture Formation

3.3.1 Combustion Characteristics

The effect of compression ratio on mixture formation and the combustion and performance of the heavy-duty LPG engine was studied in DI and PFI mode by designing a 12:1 piston, which

offered higher compression and different bowl characteristics than the 9.3:1 piston. The SOI tests were more comprehensive than the baseline study, with intermediate fuel injection regions included in the experiments along with the late and early injection timing regions. The PFI hardware was redesigned for improved valve targeting different from the baseline PFI set-up and included a double injector design specifically for higher load operation of the engine. However, the PFI configuration behaved similarly to the baseline 9.3 operation in terms of engine stability despite the increase in engine compression ratio and difference in piston design. The COV_{imep} was consistently below the 3% mark, denoting stable engine operation at all tested SOI timings as illustrated in Figure 3.9. This beneficial stable engine operation at all SOI timings was attributed to the tendency of the LPG fuel to flash boil upon injection and the distance from the cylinder which increases the mixture preparation time and supports homogeneity of the intake charge. The IMEP also remained within a narrow range for all tested SOI timings except for the highest recorded IMEP at SOI 360 deg bTDC.

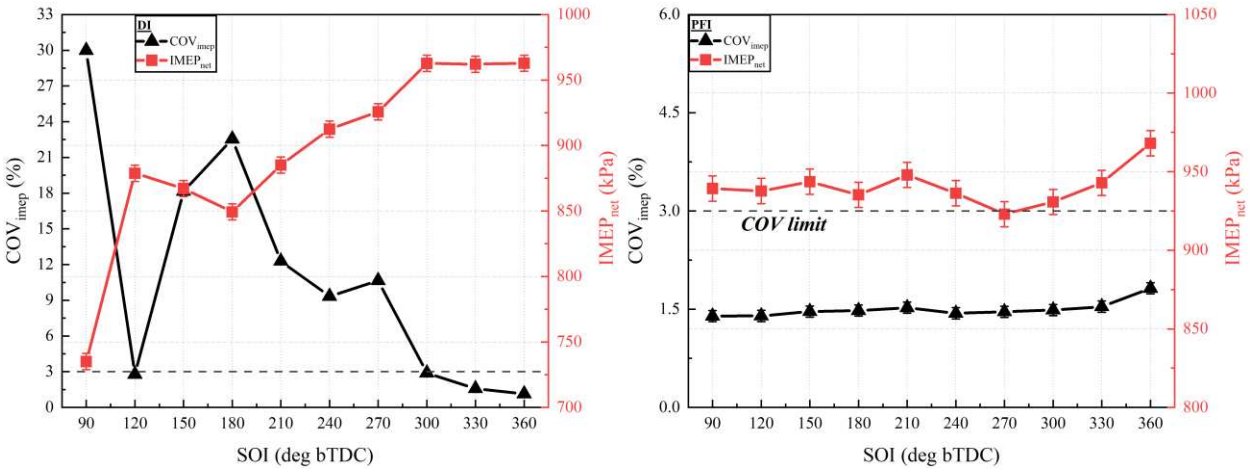

Figure 3.9. COV_{imep} and $IMEP_{net}$ vs Start of Injection timing for the heavy-duty LPG engine in PFI and DI mode at naturally aspirated conditions, 12:1 compression ratio, 1200RPM and an equivalence ratio of 1.

On the other hand, the DI configuration demonstrated a significant effect of SOI timing on engine stability similar to the baseline study with the behavior in the intermediate injection regions also captured. Importantly, Figure 3.9 also shows that the compression ratio has an effect on engine stability and SOI timing relationship. There was a pronounced extension of the stability region in the early injection timing region compared to the baseline study. SOI timings 300, 330 and 360 deg bTDC were stable engine operation conditions at compression ratio 12:1 compared to just 360 deg bTDC at compression ratio 9.3:1 in the early SOI timing regions. In the late SOI timing regions, there was a shift in the sole stable SOI timing from 150 deg bTDC at 9.3:1 compression ratio to 120 deg bTDC at compression ratio 12:1. The likely reasons for this trend are the change in fluid dynamics with the increase in in-cylinder pressure and temperature at the higher compression ratios as well as the difference in piston bowl designs. The IMEP generally trended downwards from the peak at the earliest tested SOI timing 360 deg bTDC to the minimum at the latest SOI timing 90 deg bTDC with a local peak in the late injection region at 120 deg bTDC, the only stable late SOI timing. Numerical studies were performed to better understand the in-cylinder behavior of the spray and inform the design of an optimized injection strategy for heavy-duty LPG engines. The subsequent section investigates how these fluid dynamic interactions are intensified when the compression ratio is increased to 12.0, further altering the pathway to mixture homogeneity.

3.3.2 Numerical Investigation: Effect of Compression Ratio on Mixture Formation

To verify the robustness of the numerical approach, the CONVERGE model was tested against two distinct compression ratios. After increasing the CR to 12, the same SOI trend observed in the experimental data persists. However, this trend is slightly altered from the CR 9.3 data, as the higher CR results in a phase shift between stable operational points. Reviewing the CR 12 data,

SOI 120 now represents a viable operational point, and SOI 90 is the newly observed operational limit where the COV once again surpasses the threshold. A 30° phase shift occurs when moving from CR 9.3 to CR 12, shifting the observed operational limits closer to TDC. Figure 3.10 compares experimentally measured in-cylinder peak pressure to calculated traces determined from CONVERGE 3D simulations for an SOI timing sweep from SOI 360 to SOI 90. Figure 3.10a details the experimental order of peak in-cylinder pressure by SOI (greatest to least): 360 > 330 > 300 > 240 > 120 > 210 > 270 > 150 > 180 > 90.

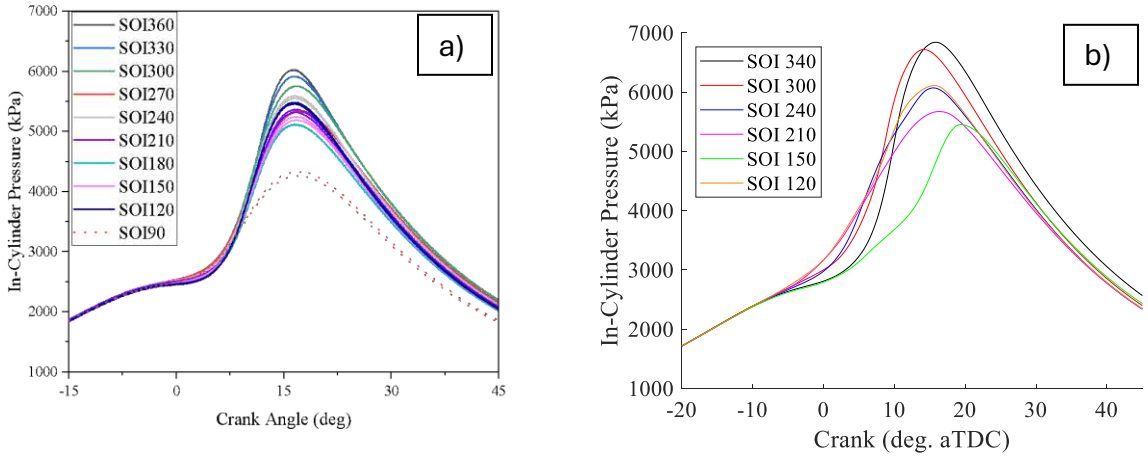

Figure 3.10. In-Cylinder pressure traces of Experimental SOI sweep vs 3D CONVERGE simulations at CR 12

Figure 3.10b highlights the results from the CONVERGE simulations indicating the ability of the reduced ALPINE 153 mechanism to capture the differences in performance between each SOI case following the experimental COV trend shown in Figure 3.9. The simulated peak in-cylinder pressures capture the performance decline as the engine stability decreases shown by the reduction in peak pressure as the SOI timing is retarded closer to TDC, where the peak pressure follows the SOI order of 340 > 300 > 120 > 240 > 210 >150. The 3D simulations capture the

experimental performance recovery observed at late injection timing of 120° bTDC. While the CONVERGE model accurately predicts the global performance trends across the SOI sweep, a minor divergence is noted between the simulated and experimental rankings of SOI 120 and SOI 240. Experimentally, SOI 240 exhibits a slightly higher mean peak pressure than SOI 120; however, the simulation shows SOI 120 marginally exceeding SOI 240. This discrepancy is attributed to the inherent cycle-to-cycle variation (CCV) present in the experimental data. The simulated pressure trace represents a single computational cycle, whereas the experimental value is an ensemble average of 1,000 cycles. Given that the experimental peak pressure values for these two timings are within a narrow margin of one another, the simulated result for SOI 240 likely reflects a cycle on the lower end of the experimental statistical envelope. Despite this minor localized inversion, the model successfully captures the broader velocity recovery phenomenon with SOI 120 which is examined in more detail in Figure 3.11. Ultimately, the alignment between the simulated results and the experimental data across both compression ratios underscores the robustness of the reduced ALPINE 153 chemical mechanism. Its ability to accurately resolve the 30° phase shift between compression ratios and capture the nuanced performance recovery at late injection timings demonstrates that the model effectively integrates the complex chemistry of LPG combustion with the highly dynamic, TKE driven flow fields inherent to high compression DI operation.

The fundamental mechanism driving the performance recovery at late SOI timings is the intensification of in-cylinder turbulence generated by the piston's upward translational velocity. While conventional internal combustion engine theory suggests that earlier injection timings are superior due to increased residence time for mixing, the TKE profiles at CR 12 reveal a critical competing effect. The TKE profiles in Figure 3.11 indicate that during each engine cycle, the intake

valve opening generates the highest TKE observed for the entire cycle, reaching an average value of 26.5 m^2/s^2.

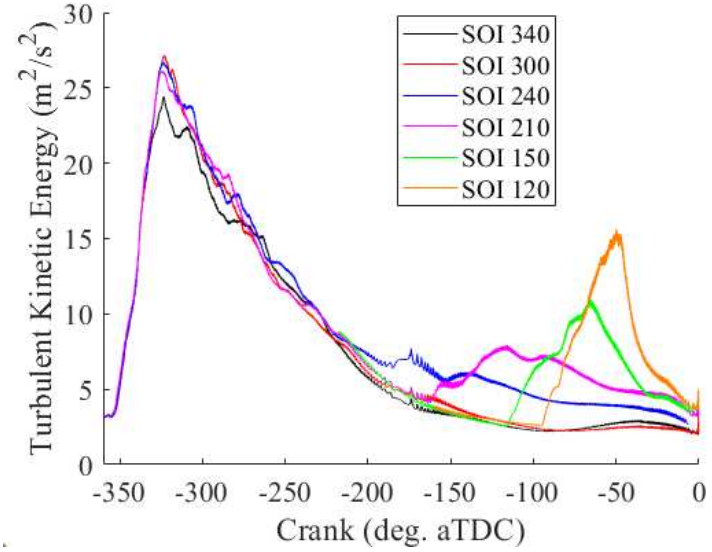

Figure 3.11. Turbulent kinetic energy (TKE) vs crank angle for each simulated CONVERGE start of injection timing at CR 12

This initial high TKE window occurring between crank angle -325° to -322° bTDC serves as the primary physical driver for the atomization of the LPG spray for early DI injection timings (-340° to -240° bTDC). However, as observed in the experimental engine stability data (Figure 3.9), the COV exceeds stable engine operational limit after SOI 300. This decline in performance is explained by the TKE evolution, Figure 3.11 shows that the peak TKE is already in a state of rapid decay by SOI 300 and only continues to diminish as the piston approaches bottom dead center at -180° bTDC. At BDC, the piston velocity reaches a momentary stagnation point, leading to a decay in organized tumble motion. Injecting during this window results in poor spray-air interaction, as the lack of fluid momentum prevents the breakdown of the fuel plume. The lack of kinetic energy during this injection range (SOI 270 to SOI 150) directly translates to the

uncontrollable engine operation as the LPG mixture cannot properly form a homogenous mixture because the influence of the intake generated turbulence has dissipated and the piston velocity is yet insufficient to generate local shear required for mixing. These TKE findings provide a clear mechanistic insight into the observed reduction in peak pressure and the rise in COV, marking this as a quiescent trough where neither intake generated nor compression generated energy is available to facilitate effective mixing.

Following the stagnation at BDC, a significant shift in the fluid dynamic environment occurs as the piston begins its upward compression stroke. The experimental recovery observed at 120° bTDC is corroborated by the CFD calculated TKE profiles where both late injection timings (SOI 120 and SOI 150) exhibit a sharp velocity recovery effect highlighted by their late cycle TKE peaks. At 120 deg BTDC, the piston enters a high-acceleration phase of the compression stroke. The resulting velocity at the piston top boundary generates sufficient shear to overcome fuel droplet surface tension, increasing the local Weber number and accelerating vaporization rate of LPG. The SOI 120 case benefits from a localized TKE intensification, peaking at approximately 15.5 m^2/s^2 slightly over halfway through the mixing process (-50° bTDC) which directly contributes to the mixture formation. This represents a 40% increase in mixing energy compared to the SOI 150 case, explaining how the engine overcomes significantly reduced residence time to achieve stable combustion. The 3D simulations successfully predicted both the performance dip after SOI 300 reaching a maximum near BDC and the subsequent recovery during the compression stroke. This dual condition validation confirms that the RNG k-ε turbulence model accurately scales the sub-grid scale energy based on boundary driven velocity gradients at the piston top, effectively capturing the interplay between mechanical motion and fluid mixing.

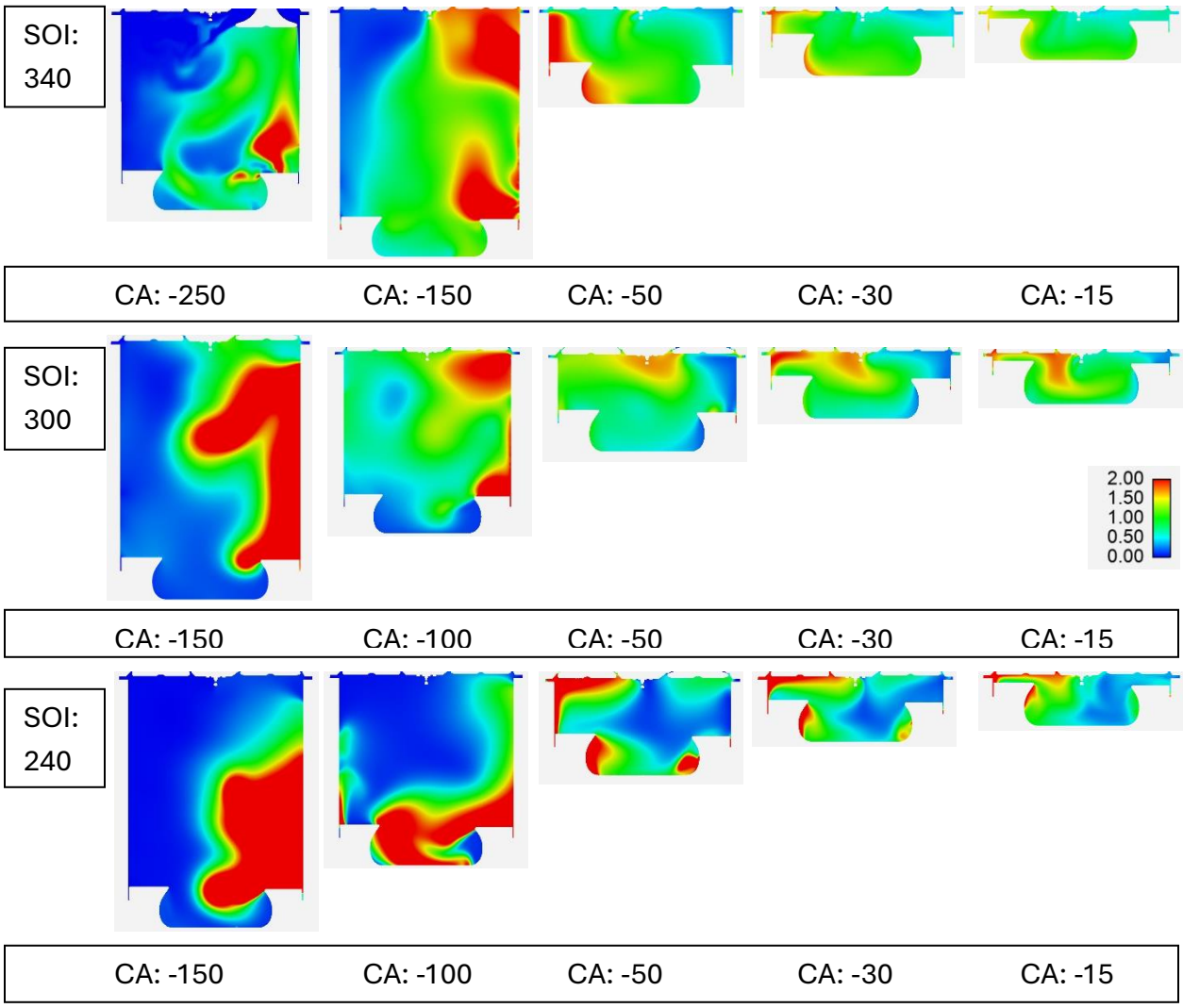

Figure 3.12. Mixture Distribution at early Start of Injection timings for DI operation at CR 12

The utility of utilizing the TKE at the piston top boundary as a diagnostic classification tool for assessing mixing potential across varying SOI timings is further substantiated by Figure 3.12 and Figure 3.13. These figures quantify the spatial mixture distribution by examining a cut plane through the spark plug for both early (SOI 340° to 240° bTDC) and late injection timings (SOI 210° to 120° bTDC) at the higher CR of 12. By coupling these mixture visualizations with the TKE profiles established in Figure 3.11, the driver behind the overall decline and recovery in engine performance as observed in both the COV trends of Figure 3.9 and the peak pressure

changes in Figure 3.10 are fully elucidated. Specifically, these distributions illustrate how the velocity decline near BDC leads to stagnant, poorly distributed fuel pockets, while the late-cycle velocity recovery successfully transports the charge into an ignitable state at the spark gap.

For the SOI timings at CR 12, five snapshots were selected throughout the injection and mixing duration to visualize the progression of charge formation toward the final distribution at spark timing. As SOI 340 represents the best performing experimental case, Figure 3.12 illustrates that by -15° bTDC, the fuel-air mixture achieves a highly homogeneous distribution where the equivalence ratio centered around the spark plug is near 1. This spatial uniformity provides the physical evidence for why this timing yields both the highest experimental peak pressure and the most stable engine operation (lowest COV). While SOI 300 remains a stable experimental operating point, the impact of the TKE decay already rapidly declining from the intake generated peak is visually apparent in the mixture formation. Specifically, at the -15° bTDC mark, the fuel on the left side of the cylinder begins to show increased stratification compared to the SOI 340 case. The reduced kinetic energy is unable to sustain the centralized distribution seen at the earlier timing, though it remains sufficient to prevent the severe stratification that leads to engine instability. By SOI 240, the lack of mixing energy is fully evident. The snapshots at -50° and -30° bTDC show rich fuel zones with the equivalence ratios reaching values near 2 that fail to disperse properly. The -15° bTDC snapshot reveals a clear degradation in homogeneity; prominent rich pockets (phi > 1.25) are visible, indicating that the decreasing TKE is no longer sufficient to fully disperse the LPG spray across the cylinder volume. The comparison of the -15° bTDC frames across these three early cases confirms a direct correlation: as the TKE intensity at the moment of injection drops, the ability of the charge to reach a near stoichiometric state at the spark gap

diminishes. This lack of a centered, uniform mixture at the electrode is the primary driver for the initial decline in peak pressure and the increase in COV observed in the experimental results.

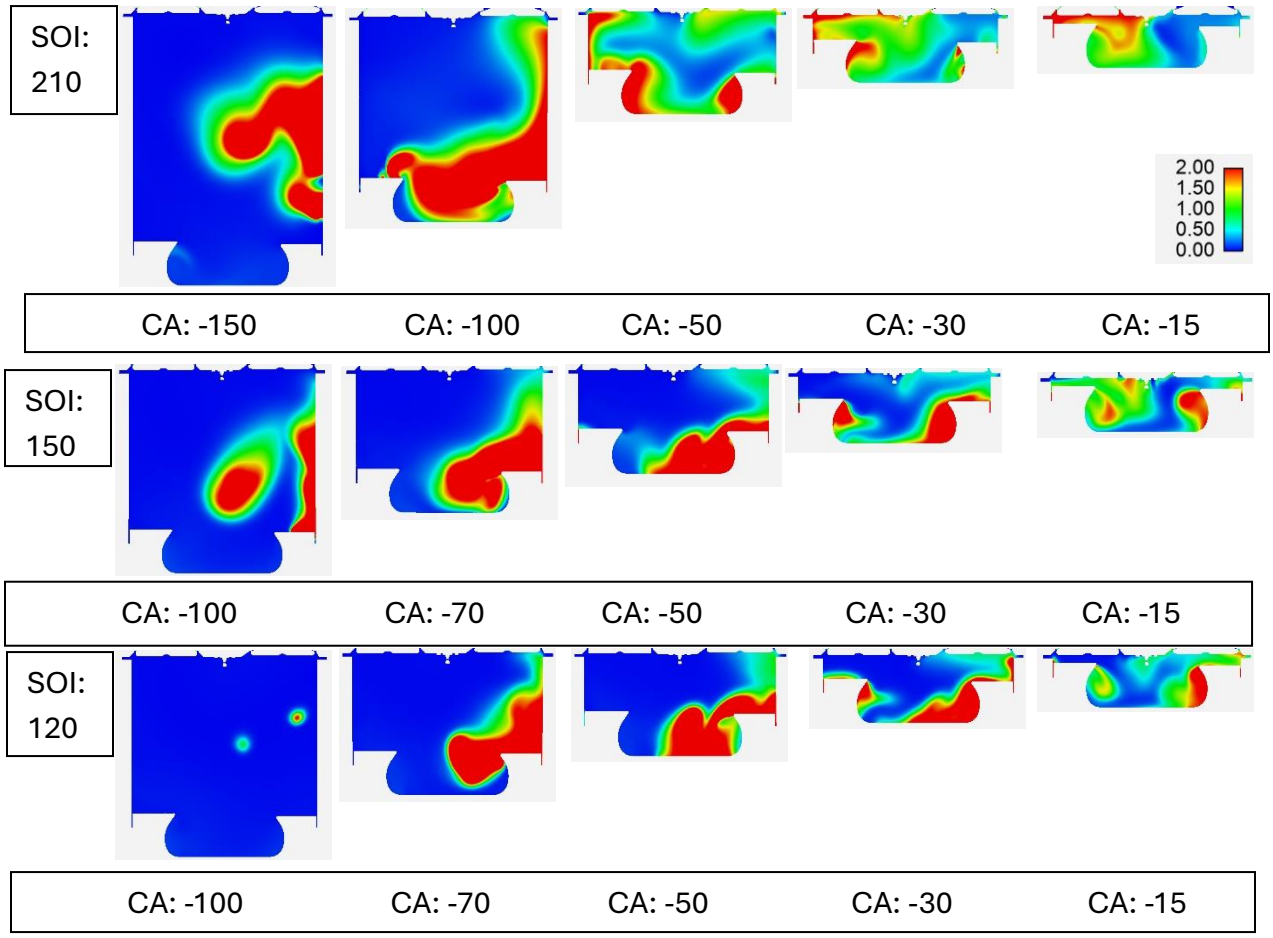

Figure 3.13. Mixture Distribution at late Start of Injection timings for DI operation at CR 12.

While the early injection timings illustrate a performance decay directly proportional to the loss of intake generated turbulence, the late cycle injection strategies reveal a reversal of this trend. To examine how the engine overcomes the velocity stagnation encountered at BDC, Figure 3.13 visualizes the mixture evolution for injection timings between SOI 210° and 120° bTDC, highlighting the physical impact of the compression-driven velocity recovery. From the experimental data, SOI 210 and SOI 150 both exhibit worse performance than the later SOI 120,

and the simulations provide a clear mechanistic explanation for this phenomenon. At these intermediate timings, LPG is injected into a low-energy environment as the piston velocity decreases near BDC, leading to massive stratification where rich pockets (phi~2.0) become sequestered deep within the piston bowl. In the SOI 210 case, the fuel mass is pushed toward the left side of the cylinder, creating a concentrated rich zone against the wall while leaving the right side nearly void of fuel. Conversely, by the spark timing of -15° bTDC, the fuel in the SOI 150 case remains largely trapped within the bowl geometry or clings to the right cylinder wall, leaving a lean, non-flammable zone at the electrode. This spatial misalignment explains the experimental instability and the dramatic drop in peak pressure at both timings. However, the TKE intensification (Figure 3.11) observed for SOI 150 explains why this later case achieves a stronger breakup of the fuel creating three distinct zones of concentration compared to the single cluster seen for SOI 210, as the peak TKE intensifies by 37.8% between these two timings.

In contrast, the SOI 120 case represents the physical culmination of the velocity recovery theory. While the intermediate late injection timings suffer from fuel sequestration, the SOI 120 case utilizes the localized TKE intensification of 15.5 m^2/s^2 to fundamentally alter the mixture formation process. As visualized in Figure 3.13, the high boundary driven shear during the upward compression stroke effectively transfers the fuel out of the piston bowl between CA -50° and -30° bTDC. This dynamic interaction prevents the formation of the stagnant rich clusters seen in the SOI 150 and 210 cases, instead transporting a stoichiometric cloud directly into the spark gap by -15° bTDC. This visual evidence confirms that the 40% increase in mixing energy from SOI 150 at SOI 120 allows the engine to overcome a significantly reduced residence time, providing the mechanistic basis for the reclaimed peak pressure and combustion stability observed in the experimental data. Furthermore, this alignment between fluid dynamic energy and resultant

mixture quality validates the ALPINE 153 chemical mechanism and the foundational spray development work conducted by Argonne National Laboratory and Colorado State University (CSU). The successful integration of these sub-models into the CONVERGE framework demonstrates the model's robust capability to resolve complex, boundary driven injection strategies and their impact on charge preparation in high compression LPG engines.

3.4 Spray Dynamics and Engine performance of a high flow LPG XDI injector

Following the validation of the spray model and the chemical kinetic mechanism, a simulation study was performed to evaluate the potential for performance optimization through hardware modification. Specifically, the study examined the transition from the baseline Delphi 5-hole injector to a high-flow XDI OEM LT4 7-hole injector. The primary motivation for this shift was the significantly higher mass flow rate of the 7-hole geometry, which substantially reduced the injection duration for a given fuel mass. From an operational standpoint, this reduction in duration is critical as it potentially expands the window of viable SOI timings. By completing the fuel delivery earlier in the cycle, the engine can benefit from an extended mixing residence time, which has been shown in section 3.2 to aid in the enhancement of mixture homogeneity and mitigate the performance decline observed with the baseline hardware. This simulation phase aims to quantify how the increased injection rate influences the mixture distribution near spark timing and the resulting combustion stability.

As illustrated in Figure 3.14, the XDI OEM LT4 injector demonstrates a significant leap in mass flow capability compared to the baseline Delphi 5-hole. While the Delphi injector reaches a maximum rate of 15.0 g/s at 350 bar, the XDI achieves a peak of 35.7 g/s at a much lower pressure of 225 bar. This 138% increase in peak injection rate facilitates a drastic reduction in injection duration. At the 170 bar injection pressure utilized for the engine experiments, the performance

gap between the two injectors is even more pronounced. The baseline Delphi 5-hole provides a mass flow rate of approximately 10.5 g/s, whereas the XDI OEM LT4 delivers 31.8 g/s. This approximately 300% increase in injection rate from the Delphi baseline at the operating setpoint allows for a drastic compression of the injection event. By delivering the required fuel mass in one-third of the time, the XDI hardware effectively increases the post-injection residence time, facilitating the charge homogenization required to stabilize combustion and overcome the stability limits identified in earlier DI sweeps. Additionally, the momentum flux entering the chamber is substantially elevated. This enhanced momentum promotes vigorous shear driven turbulence and air entrainment, ensuring that even at late-cycle SOI timings where piston-induced motion may be waning there is sufficient residual turbulence to support rapid flame kernel development and maintain combustion stability.

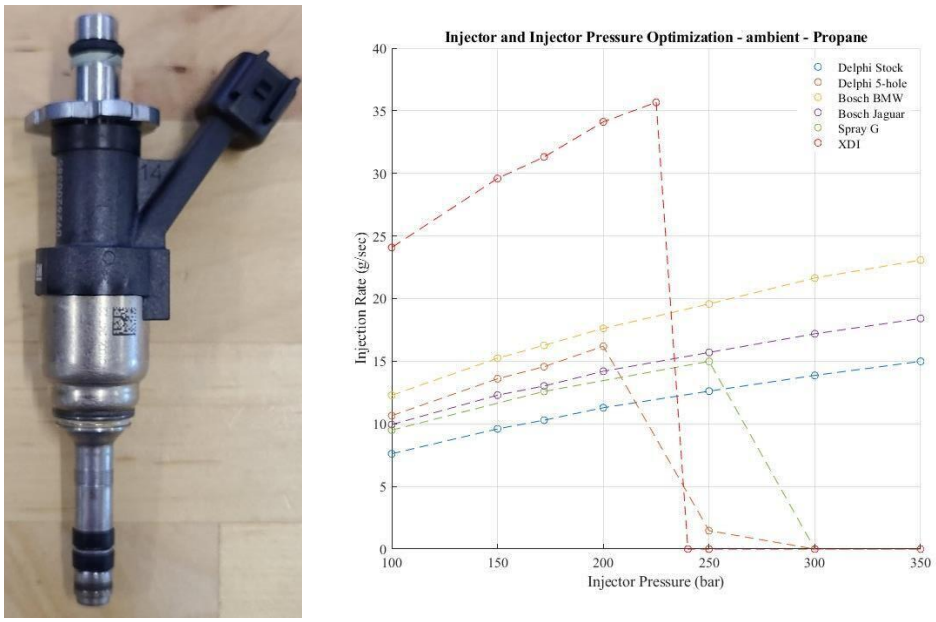

Figure 3.14. Image of the XDI injector and the results from the mass flow rate vs injection pressure sweep comparison of DI injectors.

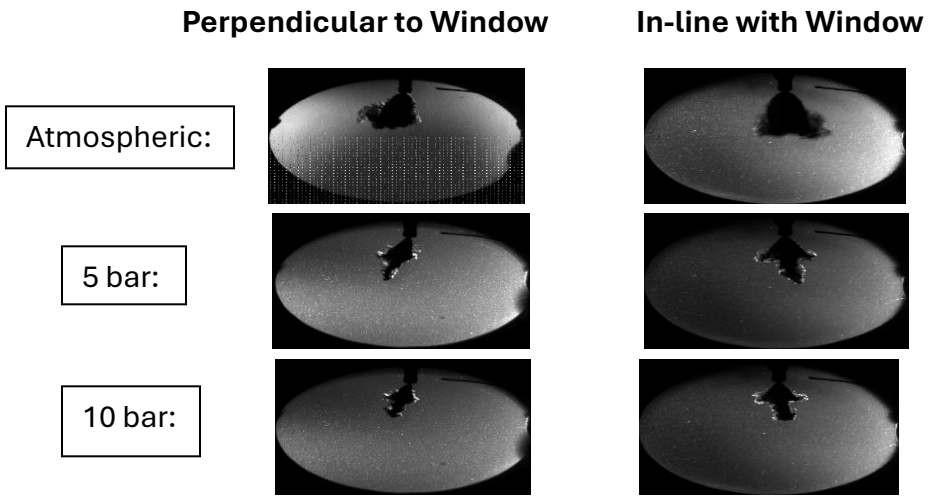

Figure 3.15**.** Direct comparison between penetration length for different chamber pressures at two injector orientations.

Following the quantification of mass flow benefits via HPSC testing, high-speed Schlieren imaging was employed to characterize the XDI injector's spray morphology. To develop a high-fidelity injector model, the spray was imaged across two distinct orientations while maintaining a constant injection pressure of 172 bar against a varying chamber pressure. As illustrated in Figure 3.15, the interaction between individual plumes is highly sensitive to the chamber pressure. At moderate chamber pressures of 5 bar and 10 bar, the individual jets remain discernible during the initial stages of injection. However, as the event progresses, the high-velocity discharge from the central 7th nozzle begins to dominate the spray structure. This central jet, a primary modification of the original LT4 architecture, acts as the primary driver for the observed mass flow gains. The impact of this 7th nozzle is clearly visible as the chamber pressure increases; the central jet's momentum allows it to surpass the boundaries of the initial injection cone penetration. This feature is responsible for the >65% gain in mass flow compared to the stock geometry and fundamentally dictates the in-cylinder injection characteristics. The geometric configuration of the nozzle, which informed the SolidWorks model used in subsequent simulations, is detailed in Figure 3.17. While the early snapshots in Figure 3.15 show individual plume development, the high momentum flux

eventually leads to a total collapse of the spray into a single, concentrated jet by the conclusion of the injection duration.

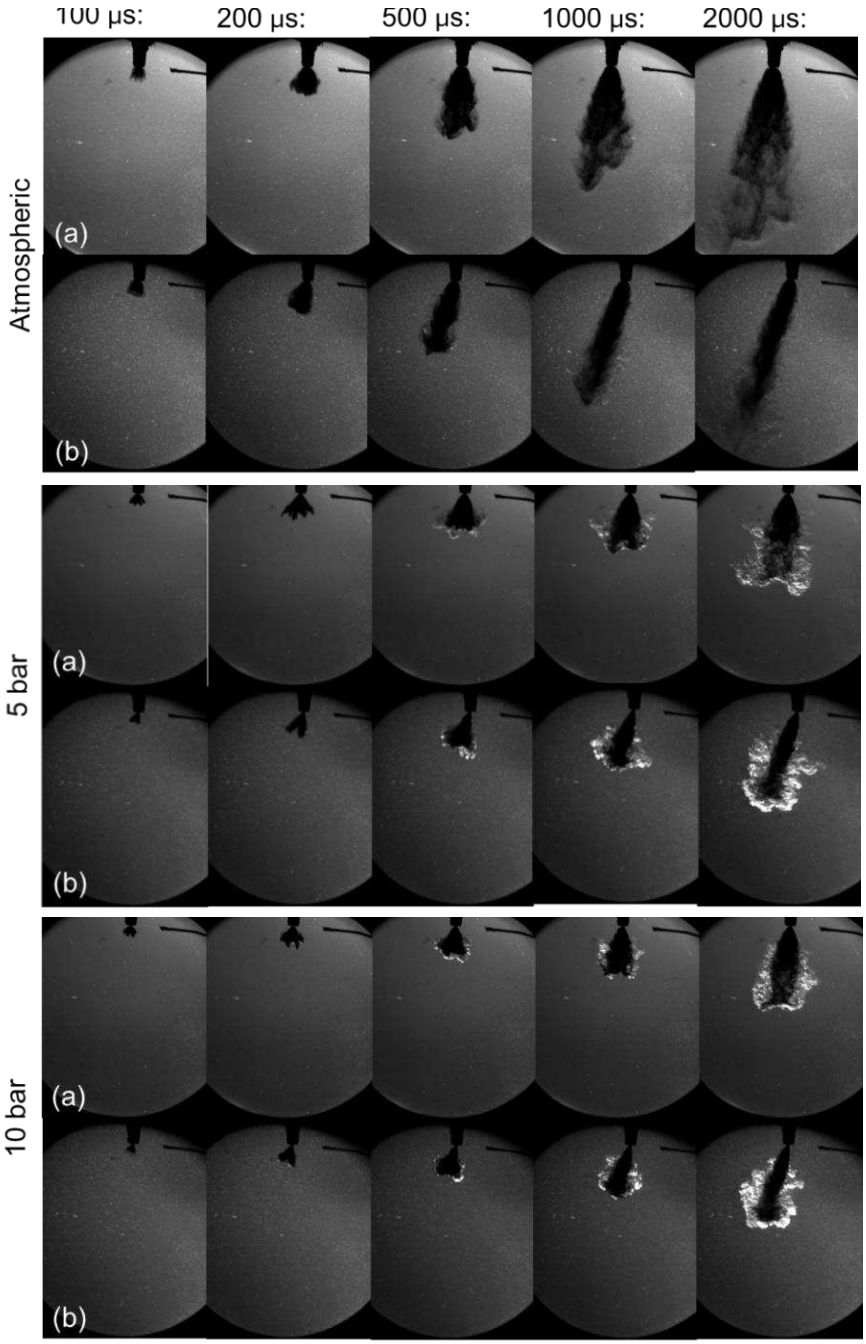

Figure 3.16. Snapshots over the initial 2000 µsec of schlieren imaging comparing penetration length and width for the OEM LT4 injector rotated (a) in line and (b) perpendicular to the imaging at atmospheric pressure (top) 5 bar (middle) and 10 bar (bottom)

To isolate the influence of the seventh nozzle and characterize the modified spray architecture, high-speed Schlieren imaging was also conducted for the baseline OEM LT4 injector. As the geometric precursor to the XDI +65% variant, the 6-hole OEM injector was imaged to establish a benchmark for individual plume cone angles and jet interaction. These baseline measurements were critical for developing an accurate 3D-CFD framework capable of simulating both the HPSC environment and in-cylinder engine combustion. The experimental results, illustrated in Figure 3.16, utilized the same dual-orientation approach as the initial XDI cases, imaging the spray both in-line with and perpendicular to the optical path. Consistent with the X15 engine test cell parameters, the injection pressure was maintained at 172 bar while the chamber pressure was swept from 0.85 to 10 bar. The data reveals that chamber pressure plays a decisive role in plume separation; at higher chamber pressures (5 and 10 bar), the individual jets remain discernible during the initial 100 to 200 microseconds of the injection event. However, even in the 6-hole OEM configuration, the spray eventually succumbs to a momentum-driven collapse into a single plume as the injection progresses. This observation is pivotal, as it indicates that jet collapse is an inherent characteristic of this injector family under high-pressure conditions, but is significantly accelerated and intensified by the high-mass-flow 7th nozzle of the XDI variant.

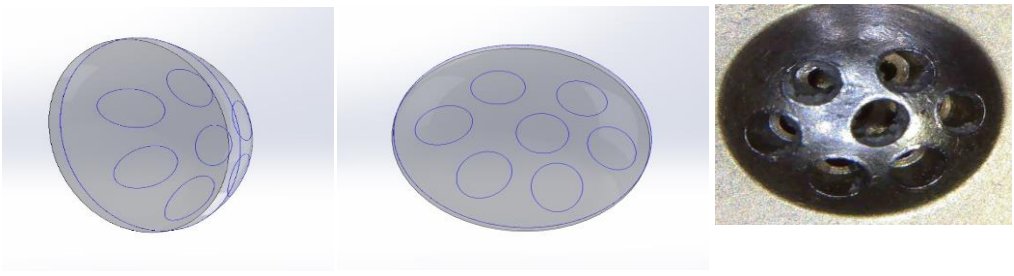

Figure 3.17. XDI Injector single SolidWorks model for implementation into HPSC.

The results from both the XDI LT4 +65% and the baseline OEM injector testing indicated that despite the 7th nozzle driving a substantial advancement in fuel propagation, both

architectures eventually resulted in the full collapse of individual injection plumes into a single observed jet. These findings provide the empirical justification for the subsequent transition to a simplified, high-momentum single-jet model in the CONVERGE CFD simulations, ensuring the numerical model reflects the physical reality of a collapsed spray. Due to the high computational complexity associated with integrating a detailed SolidWorks-derived nozzle model into CONVERGE, a streamlined simulation approach was implemented. This strategy sought to model the fuel injection as a single nozzle, as the experimental data suggested that all engine-relevant injection durations would result in this consolidated jet structure. Under these conditions, the influence of the peripheral six nozzle plumes was found to be minimal and nonconsequential compared to the dominant momentum flux originating from the central 7th nozzle.

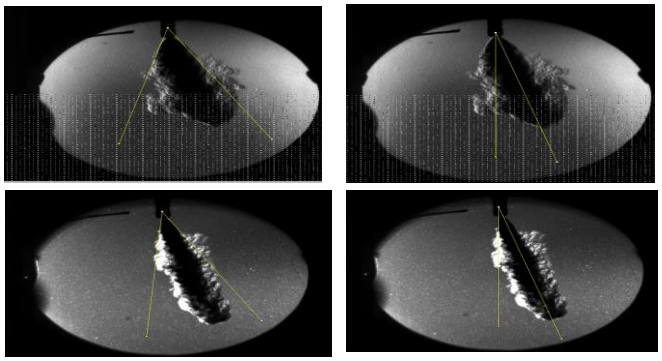

Figure 3.18 ImageJ measurements of the cone angle and the angle from the vertical at varying chamber pressures.

To parameterize this model, Figure 3.18 shows how ImageJ was utilized to determine the injection cone angle from measured experimental data at varying chamber pressures based on the known chamber window dimensions. Quantitative analysis showed that the angle relative to the vertical axis did not deviate from the measured 15° across all tested chamber pressures. However, the cone angle width demonstrated a sensitivity to ambient density, narrowing by 10° as the

chamber pressure increased from atmospheric conditions to 10 bar. Specifically, atmospheric conditions produced the widest cone angle at 40°, while the 10 bar condition resulted in a contraction to 30°. To ensure a robust representation across the pressure gradients encountered during the engine cycle, an average cone angle of 35° was utilized for the subsequent CONVERGE CFD simulations. This approach provides a computationally efficient yet physically grounded boundary condition for resolving the macroscopic mixing and fuel distribution within the cylinder.

Figure 3.19 illustrates the performance of two distinct numerical strategies designed to simulate the elevated mass flow rate of the XDI injector. The first strategy utilizes a simplified approach, where the mass flow rate of the baseline Delphi 5-hole injector is scaled upward to match the XDI's 31.8 g/s delivery rate. The second strategy is the single-nozzle method derived from the Schlieren-observed jet collapse. Both strategies are benchmarked against the baseline Delphi 5-hole experimental data to evaluate their predictive accuracy.

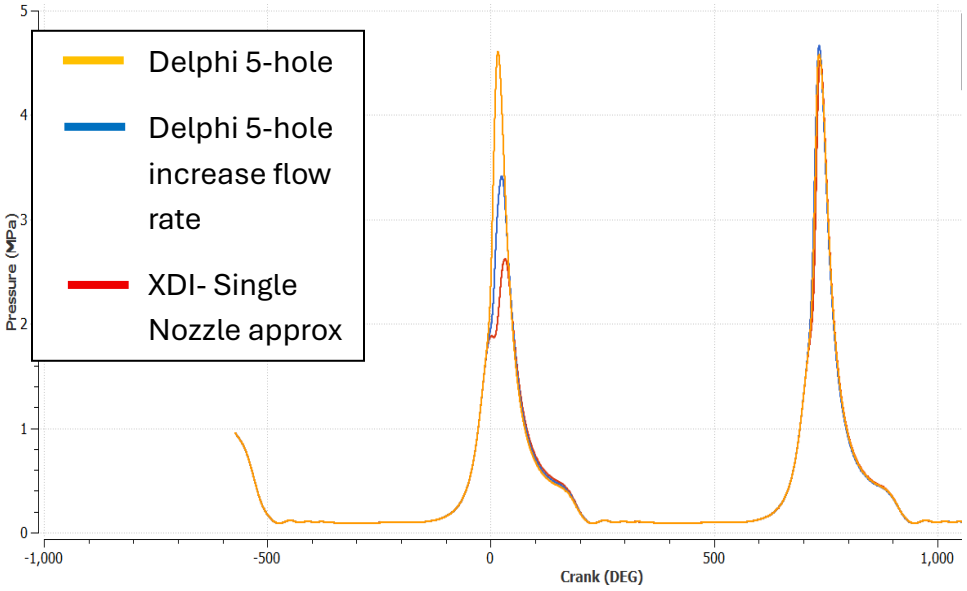

Figure 3.19. XDI Injector single nozzle model vs baseline pressure trace for CR 9.3 experimental conditions.

During the initial simulation cycle, both high-mass-flow strategies struggle to replicate the combustion characteristics of the baseline case. This initial discrepancy is likely due to the significant differences in charge cooling and local equivalence ratio distributions caused by the sudden increase in fuel mass. However, once the simulation progresses beyond the first cycle and achieves a more stable residual gas and temperature field, both injection strategies successfully converge to match the baseline performance. This convergence confirms that while the transient start-up of the simulation is sensitive to the injection model, the single-nozzle approach effectively captures the bulk energy release and pressure rise required for high-load engine simulations. Furthermore, it validates that the single-jet simplification is sufficient for predicting global engine performance parameters once the in-cylinder conditions have stabilized.

The combustion instabilities observed in the CONVERGE simulations closely mirrored the initial engine testing results obtained with the XDI injector at the baseline CR of 9.3. Rather than merely matching successful data, the CFD study was leveraged to evaluate the efficacy of the XDI's increased mass flow rate and to investigate the root causes of the instabilities that emerged when compared to the baseline Delphi 5-hole design. By utilizing a validated modeling tool to replicate these failed conditions, the underlying physics of the stability limits could be isolated and analyzed. This comparative study was conducted under baseline operating conditions: an engine speed of 1200 rpm, a compression ratio of 9.3, and a Start of Injection (SOI) of -340° ATDC for both injector configurations. The XDI simulations utilized the simplified single-nozzle approach, which—based on the previously discussed Schlieren findings accurately represents the high-momentum jet collapse characteristic of this hardware.

By maintaining identical timing and compression parameters, the simulation specifically highlights how the change in injection architecture and momentum flux alters the mixture preparation. This approach allowed for a direct investigation into whether the increased mass flow was being effectively utilized or if the resulting high-momentum jet was driving the fuel into regions of the cylinder (such as the piston bowl or liner) that were inaccessible to the flame kernel, thereby triggering the observed instabilities.

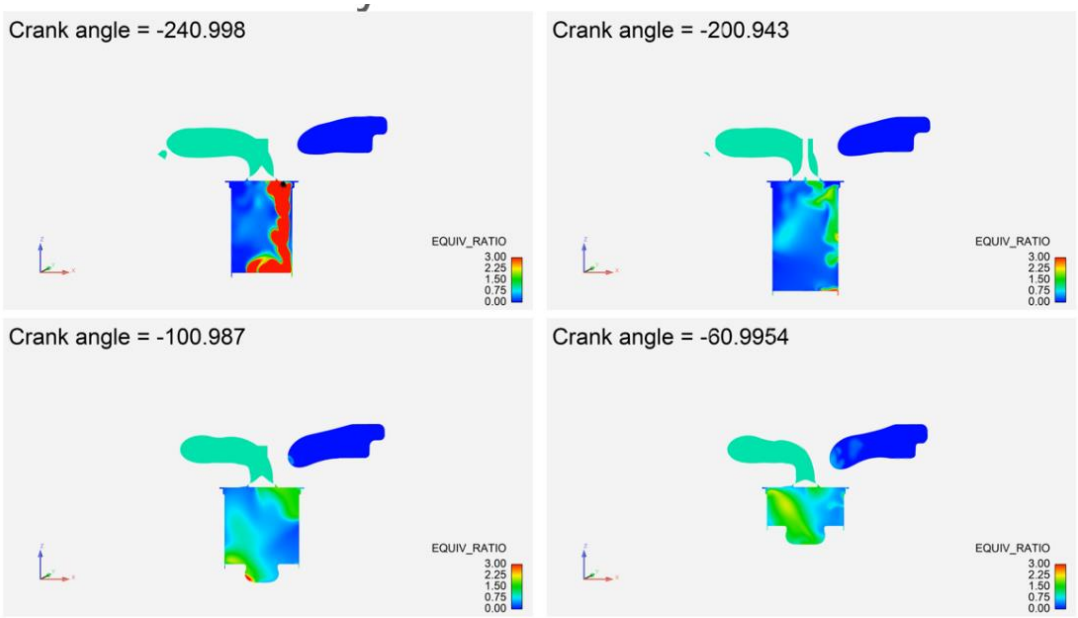

Figure 3.20. Crank angle degree resolution of the equivalence ratio for the baseline 5-hole injector during critical stages of mixture formation.

The in-cylinder equivalence ratio maps for the baseline Delphi 5-hole injector in Figure 3.20 illustrate a well-controlled fuel-air mixing process. At -240° CA, the 172 bar injection event displays distinct plumes that penetrate into the cylinder without the aggressive, singular momentum seen in the XDI hardware. While there is initial contact with the cylinder liner, the lower mass flow rate (approximately 10.5 g/s) prevents the formation of a massive, stagnant liquid film or an unmanageable rich zone. As the compression stroke progresses through -200° and -100°

CA, the Delphi plumes begin to interact with the piston bowl geometry. The Delphi's fuel clouds remain relatively central and mobile. By -60° CA, the mixture shows a favorable distribution where the fuel is beginning to occupy the central clearance volume, avoiding the deep crevice pooling that characterizes unoptimized high-flow injectors. The definitive success of the Delphi baseline is captured at -18° CA in Figure 3.22, just prior to the ignition event. At this stage, the equivalence ratio has reached a nearly homogeneous state. This level of uniformity is critical for spark-ignited operation, as it ensures that the flame kernel can initiate and propagate consistently across the chamber. These baseline results establish the gold standard for mixture preparation in this geometry, providing a clear benchmark. For the XDI injector to be successful, it must eventually replicate this level of late-cycle homogeneity despite its 65% increase in mass flow.

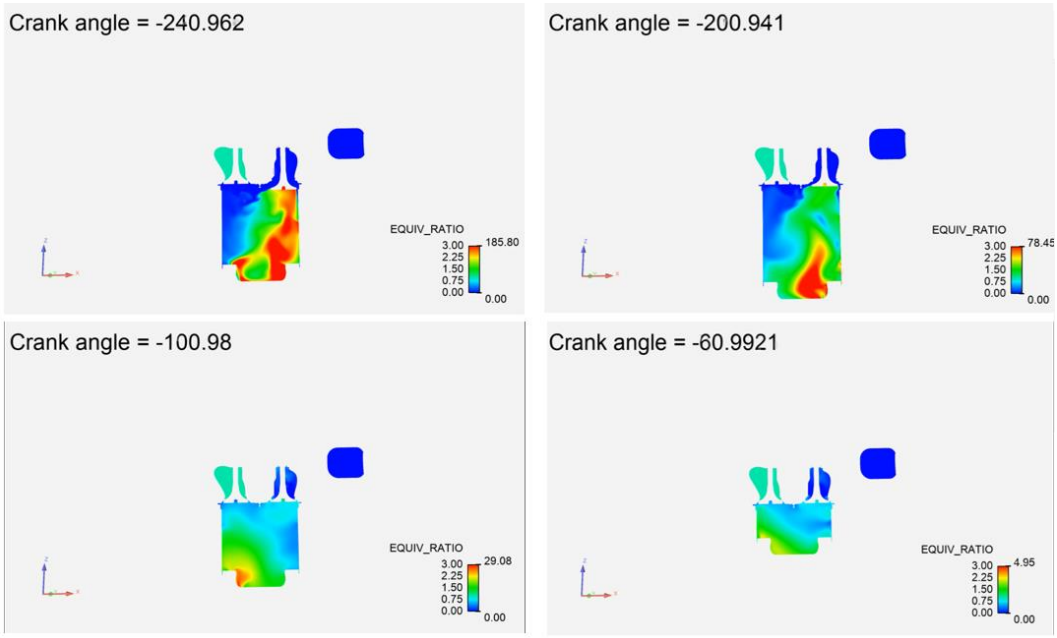

Figure 3.21. Crank angle degree resolution of the equivalence ratio for the XDI 7-hole injector during critical stages of mixture formation.

The contrast between the baseline Delphi results and the XDI simulation provides the definitive evidence for the performance degradation observed in initial testing. By comparing the spatial evolution of the equivalence ratio across these two configurations, the role of momentum-driven fuel transport becomes clear.

The equivalence ratio maps of Figure 3.21 for the XDI injector at the baseline 172 bar injection pressure reveal a drastically different mixing trajectory than the Delphi 5-hole baseline. At -240° CA, the XDI's consolidated high-momentum jet exhibits extreme penetration, with a massive rich core (phi > 3.0) driven directly into the piston bowl. As compression continues through -100° and -60° CA, this excessive momentum prevents the fuel from diffusing effectively into the central air charge. Instead, the fuel is physically trapped within the bowl geometry and along the cylinder wall. The consequence of this entrapment is most evident when comparing the state of the mixture just prior to ignition at -18° CA (Figure 3.22). While the Delphi baseline achieves a nearly homogeneous state with the combustible charge centrally located for the spark, the XDI case remains highly stratified. The XDI cylinder is characterized by localized lean zones in the central clearance volume near the spark plug, which lacks the necessary fuel concentration for a stable flame kernel. Simultaneously, a significant portion of the fuel mass remains sequestered as persistent rich pockets in the lower left region of the piston bowl. This geometric misalignment indicates that the high-flow 7th nozzle effectively over-shot the optimal mixing zone, placing the fuel where the flame cannot effectively reach it.

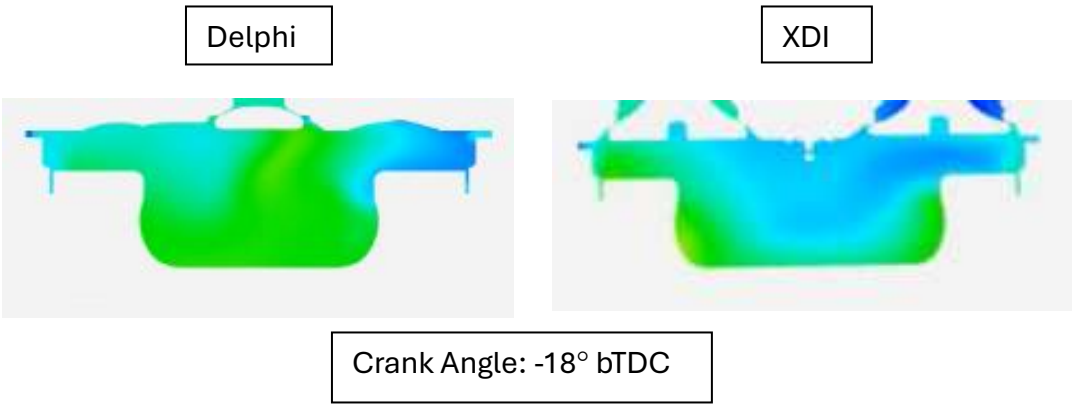

Figure 3.22. Direct comparison between the XDI 7-hole and baseline injectors near spark timing.

Analysis of Schlieren imaging (Figures 3.15 and 3.16) coupled with these simulations confirms that the increased mass flow rate led to a plume collapse phenomenon. These findings directly explain the initial experimental results at the baseline CR 9.3 condition, where the expected performance gains from the XDI injector were not realized. By coupling experimental observations with the high-fidelity CFD model, the fuel entrapment and wall wetting issues were identified as the primary bottlenecks. This diagnostic insight led to a strategic reduction in injection pressure for the subsequent experimental phases. Lowering the pressure mitigated wall wetting while still leveraging the XDI's superior mass flow rate, ultimately yielding the performance improvements initially hypothesized. This sequence underscores the utility of an accurate spray model; it serves as a powerful predictive tool that can identify hardware-driven mixture deficiencies and guide experimental optimization without the need for exhaustive and costly engine testing.

3.5 Conclusions

This chapter utilized a combination of experimental pressure trace analysis and 3D CONVERGE CFD simulations to investigate the non-linear relationship between injection timing

and combustion stability in a direct-injection engine. The following conclusions were drawn from the research.

1. The integration of the KH-RT spray model with Extreme Flash parameters demonstrated high qualitative and quantitative agreement with HPSC Schlieren and Mie-scattering data. While minor over-predictions in vapor penetration were noted at moderate chamber pressures (4 bar), the model successfully captured the rapid phase-change slopes and high-velocity expansion characteristic of LPG. This confirms the model's ability to resolve the distinct flashing behavior of LPG compared to standard liquid fuels.
2. Comparative simulations between extreme and non-extreme flash parameters revealed that engine performance sensitivity to the spray model is a function of injection timing. At early injection timings (-340° bTDC), the extended residence time allows for sufficient fuel-air mixing to mask deficiencies in the atomization sub-model. However, at late injection timings (-150° bTDC), the Non-Extreme model failed to ignite due to excessive liquid impingement and wall wetting, whereas the Extreme model correctly resolved the rapid vaporization required for combustion.
3. The validated 3D CONVERGE simulations for both Port Fuel Injection (PFI) and Direct Injection (DI) achieved excellent agreement with experimental data, with pressure traces falling entirely within the 1000-cycle experimental pressure envelope. This demonstrates that the coupled ALPINE 153 chemical mechanism and LPG spray model provide a robust predictive framework for investigating the performance limits of high-pressure LPG direct injection.

4. The failure of the non-extreme model at late timings serves as a physical diagnostic that highlights the critical importance of rapid vaporization in DI strategies. By identifying that the Extreme Flash parameters are the only ones capable of capturing the full operational spectrum (early to late injection), this work provides the foundational physics necessary to move forward with the optimization of the high-pressure XDI system.
5. Initial comparisons between PFI and DI strategies at both compression ratios of 9.3 and 12 demonstrated that combustion instability is exclusively sensitive to SOI timing in direct injection operation. While the PFI strategy maintained a stable COV of IMEP across all timings, the DI cases exhibited a distinct performance decline at intermediate injection timings that was not only intensified by the higher compression ratio but also characterized by a noticeable phase shift in optimal injection timing. This shift suggests that the increased in-cylinder density at CR 12 fundamentally alters the interaction between the fuel spray and the airflow, shifting the window of stability relative to the lower CR configuration.
6. Experimental and numerical data identified a critical decay in turbulent intensity near bottom dead center that correlates with the observed combustion instability increase at CR 12. At SOI 150°, the turbulent kinetic energy at the piston top boundary remains below 11 m^2/s^2 compared to 26.5 m^2/s^2 at earlier injection timings, and this lack of aerodynamic shear prevents effective fuel/air atomization.
7. A significant performance recovery was observed at SOI 120° bTDC, proving that turbulent intensity is a more critical driver for fuel preparation than total residence time. Despite a 20% reduction in mixing duration compared to SOI 150°, the rapid

acceleration of the piston generates a TKE spike of approximately 15.5 m^2/s^2 representing a 40% increase in mixing energy allowing the engine to overcome the reduced residence time by effectively transferring the fuel out of the piston bowl.

8. Vertical cut-plane analysis at the spark plug successfully visualized the results of these high-energy boundary interactions, providing critical insight into why performance decreased at intermediate timings. The simulations not only captured the performance recovery at SOI 120° bTDC but also accurately visualized the formation of stagnant, rich fuel clusters during the performance This visual evidence of mixture inhomogeneity at the spark gap compared to the homogeneous stoichiometric cloud at SOI 120° confirms the model's capability to resolve the complex, boundary driven physics that dictate combustion stability for varying CR seen during LPG engine operation.

9. These observed trends were validated as robust across varying geometric constraints, specifically at both CR 9.3 and CR 12. While the higher compression ratio increased the magnitude of the instabilities and shifted the optimal SOI timings, the underlying physics governed by the momentum exchange at the piston top boundary remained consistent.

10. The transition to a streamlined, single-jet simulation approach in CONVERGE accurately captured the bulk momentum flux of the collapsed spray, providing a computationally efficient yet physically grounded tool for diagnosing combustion instabilities.

11. The Equivalence ratio mapping of the XDI and Delphi injectors proved that reducing injection pressure was the primary lever for mitigating wall wetting and pulling the fuel cloud back into the central clearance volume, effectively stabilizing combustion while leveraging the XDI's high mass flow capacity.

Numerical and experimental results further demonstrate that while the optimal SOI timing is sensitive to the compression ratio, the underlying physical mechanism, the requirement of high boundary-layer velocity for effective fuel atomization remains invariant. This suggests that the piston top velocity profile can be used as a universal design parameter for optimizing DI timing and ensuring engine performance can still be maintained when changing compression ratios.

While the optimization of the XDI injection system provided a stable hardware platform for high mass flow operation, the ultimate decarbonization potential of the Cummins X15 engine relies on the integration of low-carbon alternative fuels. LPG has already seen widespread application due to its favorable emission profile and established infrastructure. However, to further reduce the carbon intensity of the combustion process, there is significant potential in blending LPG with renewable DME. Despite the promise of these blends, a critical knowledge gap remains regarding their specific performance and autoignition characteristics, specifically their Motor Octane Number (MON) and Research Octane Number (RON) when applied to modern, high-load engine architectures. Consequently, Chapter 4 focuses on an experimental characterization of LPG/DME blends to quantify these fundamental fuel properties and determine their viability for real-world engine applications.

CHAPTER 4 ALTERNATIVE FUELS: DETERMINING THE EFFECT OF DME ADDITION ON THE PROPERTIES OF LPG/DME BLENDS UTILIZING A SPARK IGNITED COOPERATIVE FUELS RESEARCH ENGINE

4.1 Motor and Research Octane Numbers

This section discusses the results related to the MON and RON testing of the LPG/rDME blends. The measured MON and RON are provided in Figure 4.1. The Oberon 100% LPG fuel sample resulted in a MON that is consistent with the previously established literature results and the preliminary test of commercial AmeriGas LPG [23, 76]. Boldt [77] and Morganti et al. [76] both determined the MON and RON for various LPG compositions where Morganti et al. reported a MON of 96.3 for 100% LPG, while Boldt found a similar value of 96.3 ± 0.7. The measured MON 96.5 ± 0.2 for the Oberon 100% LPG is within the 95% confidence interval of that previously measured with commercial LPG compositions.

As the concentration of rDME increases, as expected, the MON values decrease. At the max rDME blend level investigated of 30%, the MON was measured to be 84.2, a 12.4% decrease in MON compared to the 100% LPG baseline fuel. Interestingly, the fuel blends assessed did not vastly deviate from the baseline value of 100% LPG until the concentration of rDME increased above 20%. The 20% rDME blend maintained a MON of 90.3 - a 6.3% decrease from the baseline.

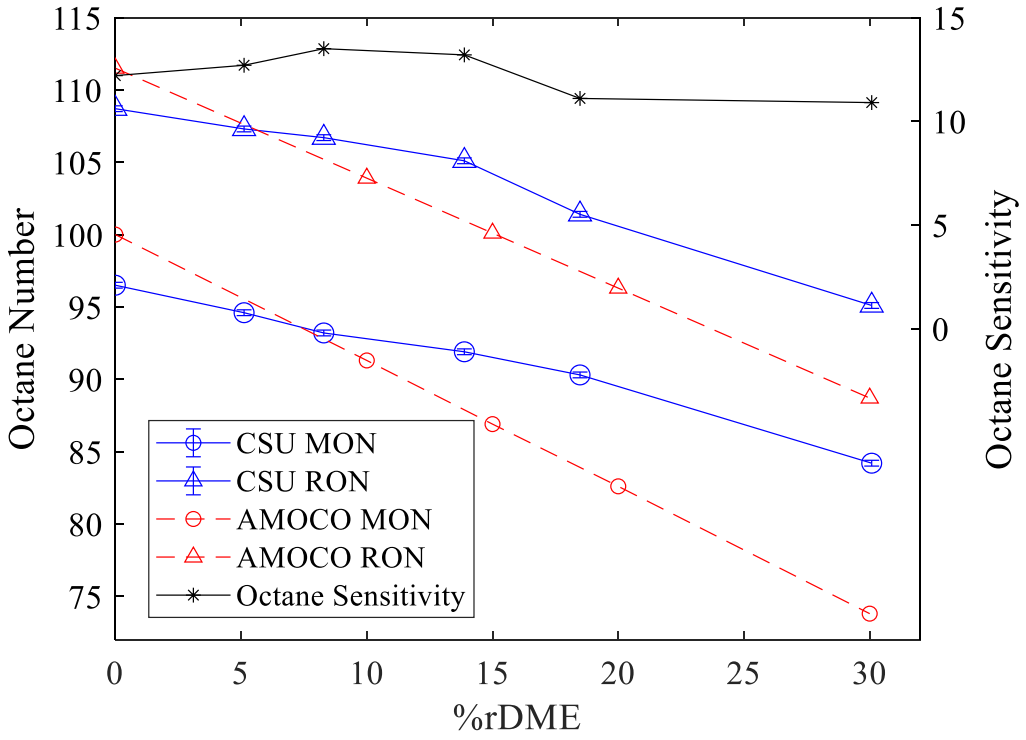

Figure 4.1. Colorado State University (CSU) and American Oil Company (AMOCO) Octane Numbers for LPG/rDME blends ranging from 0-30% rDME.

The RON of 108.7 determined for 100% LPG agrees with Morganti et al findings of 109.4 for pure propane and 108.2 for HD-5 propane [76]. The RON testing followed the same trend observed with the MON data where the behavior of the intermediate blends of rDME slowly deviates from the baseline, showing that the RON of blends up to 20% rDME is relatively insensitive to the addition of rDME with a 6.6% reduction observed for the 20% rDME blends from the baseline 100% LPG fuel. The RON of 30% rDME saw the biggest difference from the baseline between both test methods decreasing 13.5%. The RON and MON values experienced a similar overall reduction in octane number between the 100% LPG and 30% DME blend with a difference of 13.85 for the RON data set compared to 11.95 for the MON testing.

Examining the average octane number ((RON+MON) /2) or known more commonly as the antiknock index (AKI) for the 20% rDME blend results in value of 95.9, which suggests a higher resistance to autoignition than premium commercial grade gasoline (average AKI of 87-93). The 30% rDME blend exhibits the closest behavior to mid-grade 89 gasoline with an AKI value of 89.7. Similar blending behaviors have been seen in other combustion properties of blended DME/LPG fuels, consistent with the results of engine test data presented by Soto et al. [29] where DME/LPG blends up to 20% offered performance metrics comparable to 100% LPG. Consistent with earlier experimental work by Lee et al. [78], 100% LPG and a 20% rDME/LPG blend showed comparable explosion hazards, evident in their very similar flame speeds and overpressure. However, 100% DME produced the highest velocity and overpressure.

For all the sample fuels tested, the octane sensitivity or the difference between the RON and MON are displayed in Table 4.1. Mittal et al. [79] found that fuels with higher sensitivity showed better antiknock performance under knock-limited engine conditions. They used chemical kinetic models to study autoignition in fuels with increasing sensitivity. Their analysis revealed that fuels with high sensitivity have a strong temperature dependence in the intermediate temperature range of 775K–900K. This leads to slower low-temperature chemistry and faster high-temperature chemistry, mainly due to aldehyde formation. For the fuels studied in this paper, an increase in sensitivity was observed with an increase in DME concentration until a maximum sensitivity of 13.5 was obtained with the 10% rDME blend, then the fuel sensitivity decreased with rDME addition reducing to 10.8 for the 30% DME blend. The sensitivity results indicate that the 10% and 15% rDME blends exhibit higher temperature dependence in the intermediate combustion regime. This characteristic promotes improved antiknock behavior under operating conditions that yield lower end-gas temperatures, primarily due to slower low-temperature

chemistry in this regime [79]. This behavior is corroborated by Soto et al. [29], who investigated the effects of DME/LPG blends on knocking in a boosted spark-ignited engine. Their findings indicated that a 10% DME blend exhibited similar engine performance metrics, including COV of IMEP and indicated efficiency, to regular propane at MBT operation. While its knock intensity was slightly higher due to an octane number change, the performance still aligned directly with regular propane.

Table 4.1
Octane Number and Sensitivity

Fuel	**CSU MON**	**CSU RON**	**Sensitivity (RON-MON)**	**CSU (R+M)/2**
100% LPG	96.5 ± 0.2	108.7 ± 0.2	12.2 ± 0.4	102.6 ± 0.4
5% DME	94.6 ± 0.2	107.3 ± 0.2	12.7 ± 0.4	101.0 ± 0.4
10% DME	93.2 ± 0.2	106.7 ± 0.2	13.5 ± 0.4	99.9 ± 0.4
15% DME	91.9 ± 0.2	105.1 ± 0.2	13.2 ± 0.4	98.5 ± 0.4
20% DME	90.3 ± 0.2	101.4 ± 0.2	11.1 ± 0.4	95.9 ± 0.4
30% DME	84.2 ± 0.2	95.0 ± 0.2	10.8 ± 0.4	89.7 ± 0.4

Table 4.2 Gas Chromatography Results for test fuels taken before and after engine testing

Samples Taken before Engine Testing					
	Ethane	Propene	Propane	RDME	Butane
5% rDME	1.83	.10	91.22	4.66	2.19
10% rDME	1.86	.24	87.21	8.57	2.12
15% rDME	1.30	.33	80.57	15.10	2.69
20% rDME	1.73	.48	77.76	18.49	1.54
30% rDME	1.14	NA	67.54	29.42	1.90

Samples Taken After Engine Testing					
	Ethane	Propene	Propane	RDME	Butane
5% rDME	1.44	NA	91.69	4.82	2.05
10% rDME	1.89	NA	87.58	8.87	1.66
15% rDME	1.76	NA	83.37	13.48	1.39
20% rDME	1.52	NA	78.11	18.93	1.45
30% rDME	1.13	NA	67.75	29.96	1.17

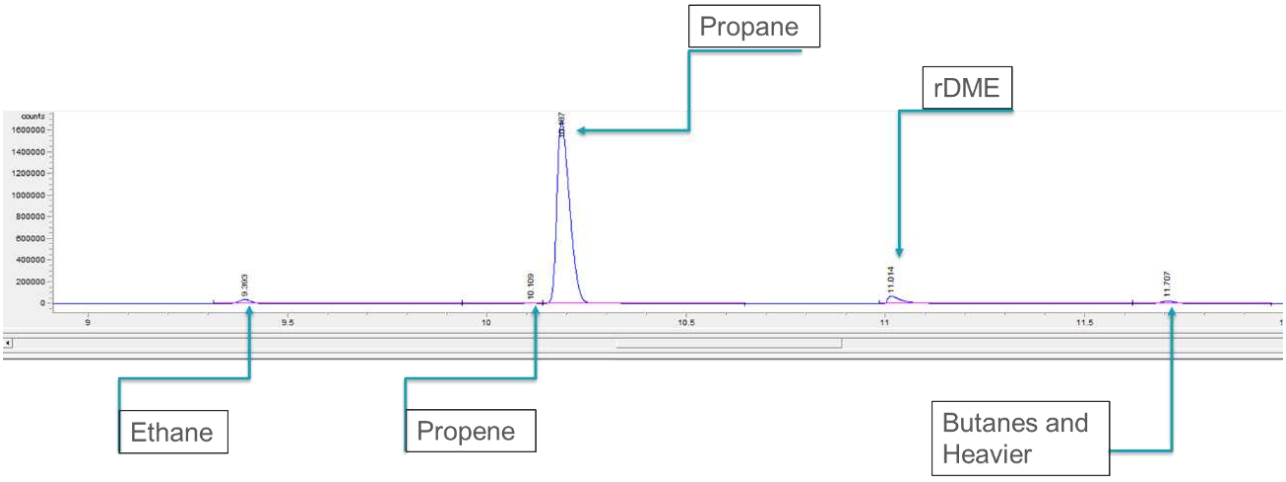

Figure 4.2. Example Gas Chromatograph Plot for an LPG/DME blend.

The work conducted in this study demonstrates that octane number ratings using an in-cylinder pressure transducer can accurately predict a fuel's reactivity when compared to the ASTM standard detonation meter. For example, there are many methods to quantify knock intensity with in-cylinder pressure transducers shown in the work of Bayliff [65, 66] while this study used the FFT method to evaluate the knock intensity. If the user understands the knock limits of their test engine the cylinder height guide tables do not have to be used to predict accurate octane numbers. To compare knock quantification methods, the maximum amplitude of bandpass filtered cylinder pressure trace (MAPO), defined in Bayliff's work [65, 66], was found for all the test conditions and produced the same MON and RON within the determined uncertainty across all test fuels when compared to the FFT method indicating that the scale to quantify knock intensity can be updated from the detonation meter. The MAPO values are displayed with the FFT in Table 4.3 and Table 4.4.

The only available data from literature regarding the octane numbers of LPG/rDME blends was conducted in 1995 by AMOCO [80] with their corresponding data displayed in Figure 4.1 in

red. The data presented in the AMOCO study results in a linear fit R-squared value of directly one, bringing into question the validity of the data as the measured ON in this study did not exhibit a linear behavior as the concentration of rDME increased. Additionally, the change in behavior could be due to differences in the fuel constituents between AMOCO and the experiments conducted in this study. AMOCO does not provide a gas chromatograph of their tested fuels, and they do not define whether they tested pure propane or if it followed the HD-5 guidelines for LPG. The fuels tested here contained residual methanol and water impurities from DME manufacturing but at the reported trace levels it is not expected that these impurities would impact the reactivity of the fuel blend.

Table 4.2 presents the results for gas chromatography testing taken both before and after engine testing experiments to ensure that the mixture composition was not changing during engine operation. All of the blends experienced slight reductions in the butane and heavier hydrocarbons but the propane and DME values were consistent between both test cases. Figure 4.2 shows an example of the peak formations determined by the GC for each of the present fuel constituents.

4.2 MON & RON Combustion Characteristics

First, considering the MON CFR experiments, Figure 4.3 presents measured representative in-cylinder pressure traces for both the sample fuel and bracketing PRFs. For the sample fuels, the 1000 experimental cycle envelope is presented along with an average and knock representative trace; while a knocking representative cycle pressure trace is displayed for each of the PRFs. For the test fuels, the LPG/rDME gaseous blends exhibited a more advanced location of peak pressure than the PRFs. For the baseline MON testing of 100% LPG, the average peak pressure is higher, and the average location of peak cylinder pressure is more advanced than the PRFs, occurring at 6.4 crank angle degrees (CAD) aTDC: 3 CAD earlier than PRF 96 and 3.8 CAD earlier than PRF

98. At a 30% concentration of rDME, the average peak pressure location is still advanced when compared to the PRFs 84 and 86, respectively. Table 4.3 highlights combustion properties obtained from MON testing. The determined MON IMEP between the 100% LPG baseline and the 30% rDME blend has a 2.4% difference allowing for comparison between the two test fuels to be made. When moving to the 30% rDME blend, the compression ratio had to be reduced to achieve the same medium knock FFT rating. The CA50 and knock onset crank angle (KOCA) for the 30% rDME blend was more delayed by approximately 1.5 CAD when compared to the 100% LPG baseline, but the other operational parameters including the CA10-50 and CA10-90 remained unchanged between the two test fuels. The same trend is observed for the other blends of rDME/LPG during MON testing observed in Table 4.3.

In addition, Figure 4.3 displays the KOCA in red for the test fuel while in blue and green for the PRFs on both the in-cylinder pressure and the AHRR traces. The average knock point obtained from 1000 cycles of engine operation and four representative knock cycles are presented in Figure 4.3. The knocking representative cycles were chosen through a cost function which analyzes the average knock intensity and chooses representative cycles that closely match the average knock intensity. KOCA can be defined as the crank angle at which a sharp inflection occurs in the in-cylinder pressure trace right before the onset of high frequency pressure oscillations. The peak of the second derivative of the in-cylinder pressure trace is utilized to determine the approximate knock location for each cycle following the method described in the work performed by both Bayliff et al. and Kar et al. [65, 66, 81, 9]. Considering 100% LPG the average KOCA occurred at 3.9 deg aTDC compared to 6.8 and 7.6 deg aTDC for the lower and higher bracketing PRFs. The same trend is observed when increasing the concentration of rDME on the KOCA locations as the test fuel is more advanced than the bracketing PRFs. Examining 30% rDME, the

average KOCA point occurs at 7.59 deg aTDC, then 10.1 and 10.9 deg aTDC for PRFs 84 and 86. For all the test fuels the onset location of knock proceeded the PRFs.

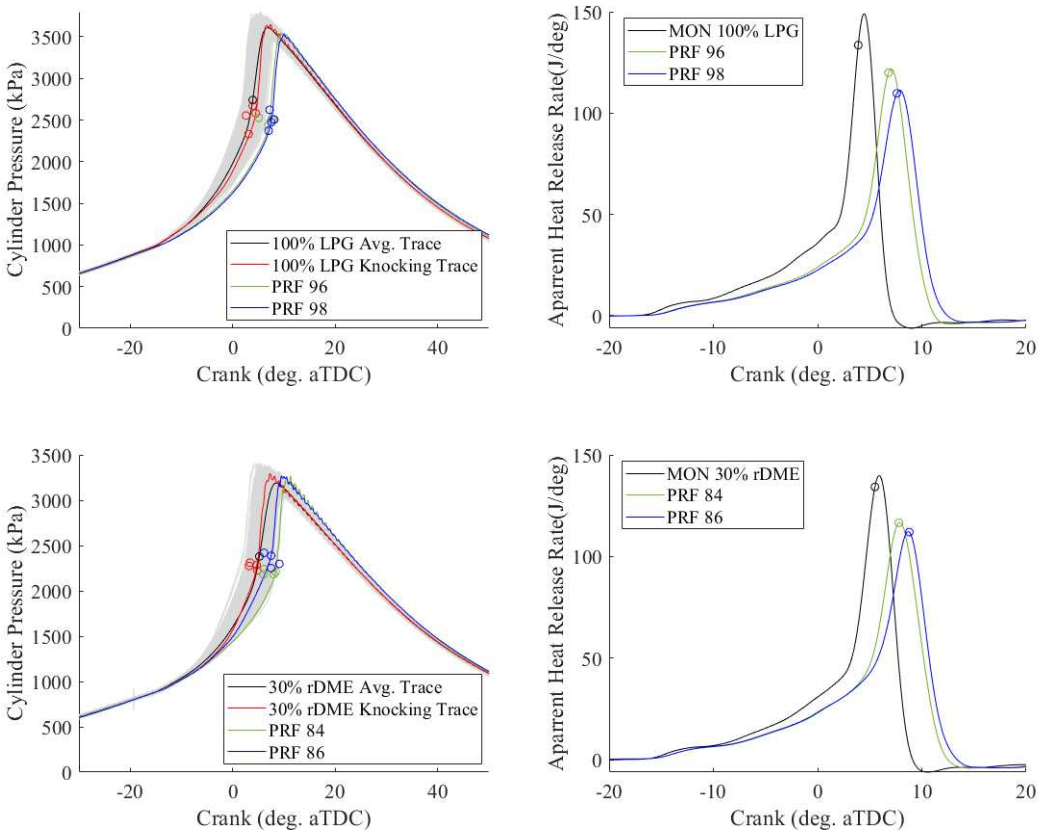

Figure 4.3. MON In-Cylinder pressure trace with knock onset crank angle (KOCA) locations for 100% LPG, 30% rDME and their corresponding bracketing fuels. Average pressure trace is shown for the fuel while a representative knocking cycle is displayed for both the sample fuel and the PRFs. Additionally, the 1000 cycle average Apparent Heat release rates (AHRR).

Table 4.3 and Table 4.4 display the indicated mean effective pressure (IMEP) obtained for all the tested fuels. IMEP is calculated using the indicated work over the entire cycle. Comparing the PRFs and the test fuel, the IMEP follows the order, sample fuel<lower PRF < higher PRF

where the sample fuel exhibits the lowest IMEP while the higher bracketing PRF obtains the highest IMEP. For MON testing, the IMEP increases from the 100% LPG baseline with the addition of rDME even though the CR is decreased. The COV of IMEP stays under 2 for all the tested fuels showing that the engine can maintain operation stability with the higher concentrations of rDME. The RON experiments follow a different trend as the IMEP between the test fuels and the 100% LPG baseline effectively remain the same until the 30% rDME test case where a decrease in IMEP occurs.

For the MON experiments, a CR of 7.8 was employed for testing 100% LPG. As the sample fuels concentration increased with rDME, the compression ratio had to be decreased to keep the knock intensity in the desired range resulting in a CR of 7.53 for 15% rDME and CR of 7.03 for 30% rDME. The mass fraction burn (MFB) duration in crank angle is compared across the sample fuels assessed, both the CA10-50 and CA10-90 are considered to examine how the addition of DME affects the flame progression in-cylinder. The flame development time and the flame propagation does not change with the addition of rDME observed from Tables 4.3 and 4.4 as the 10-50% MFB does not vary across the sample fuels, while the PRFs experience a delayed 10-50% MFB when compared with the test fuels during MON testing but for the higher sensitivity fuels CA10-90 are more delayed than the lower bracketing fuel during RON testing. These findings are consistent with previous results from literature as Vasu et al. [71] conducted experiments to determine the laminar flame speed (LFS) of various rDME/LPG mixtures. Vasu et al. found a significant difference between the flame speed of the two pure constituents with rDME having a higher velocity but when looking at blends with lower concentrations of rDME, less than 20% rDME results in the flame speed and other combustion characteristics remaining the same as 100%

LPG [71]. The RON experiments were conducted at a higher CR, but the same general trend observed in the MON data is captured also in the RON cases.

Table 4.3 MON Combustion Properties

MON										
Test Fuel	**CR**	**IMEP (kPa)**	**COV IMEP**	**FFT**	**MAPO**	**CA50 (°aTDC)**	**CA 10-50 (°aTDC)**	**CA 10-90 (°aTDC)**	**KOCA (°aTDC)**	**Lambda AFR**
100% LPG	7.8	498	1.3	992	38	2.95	9.6	12.0	3.9	0.948
PRF 96	7.8	516	1.8	1042	40	5.63	10.3	13.2	6.8	0.934
PRF 98	7.8	519	2.0	826	33	6.18	10.6	13.7	7.6	0.939
5% DME	7.8	539	1.3	1749	44	3.6	9.8	12.4	4.7	0.937
PRF 94	7.8	567	1.3	2109	46	5.5	10.4	13.6	7.2	0.925
PRF 95	7.8	568	1.2	1547	42	5.6	10.5	13.7	7.4	0.924
10% DME	7.0	531	1.1	805	23	4.6	9.4	13.7	7.4	0.915
PRF 92	7.0	564	1.2	1573	30	7.0	10.3	15.1	10.0	0.940
PRF 93	7.0	569	1.2	865	26	7.0	10.4	15.0	10.3	0.933
15% DME	7.5	530	1.2	1322	45	3.89	9.6	12.5	5.1	0.926
PRF 91	7.5	548	1.2	2053	49	5.8	10.4	14.2	8.2	0.905
PRF 92	7.5	555	1.2	1204	44	5.8	10.3	14.0	8.0	0.905
20% DME	7.4	516	1.3	1850	39	3.8	9.6	12.2	4.7	0.956
PRF 90	7.4	527	2.0	1940	42	6.2	10.3	13.7	7.7	0.972
PRF 92	7.4	532	2.0	1418	31	6.6	10.7	14.2	8.2	0.979
30% DME	7.0	510	1.2	1716	71	4.4	9.7	12.3	5.2	0.985
PRF 84	7.0	516	1.5	1763	73	6.4	10.6	13.7	7.7	0.937
PRF 86	7.0	523	1.4	1308	57	6.7	10.9	14.3	8.5	0.936

Table 4.4 RON Combustion Properties

RON										
Test Fuel	**CR**	**IMEP (kPa)**	**COV IMEP**	**FFT**	**MAPO**	**CA50 (°aTDC)**	**CA 10-50 (°aTDC)**	**CA 10-90 (°aTDC)**	**KOCA (°aTDC)**	**Lambda AFR**
100% LPG	9.9	638	0.98	1250	38	4.2	9.1	12.0	6.1	0.967
PRF 107.6	9.9	660	1.08	1522	28	5.6	9.6	12.2	7.1	1.033
PRF 110	9.9	669	0.92	851	51	6.1	9.8	13.2	8.5	1.010
5% DME	9.7	636	1.3	1192	40	4.5	9.1	12.0	6.7	0.981
PRF 103.3	9.7	637	1.4	2517	85	4.4	8.6	10.2	4.9	1.005
PRF 107.6	9.7	664	1.3	1073	32	5.8	9.5	12.7	7.8	1.012
10% DME	9.4	636	1.1	740	27	4.8	9.3	12.9	7.4	0.970
PRF 103.3	9.4	652	1.3	1772	54	5.6	9.5	11.8	6.7	0.992
PRF 107.6	9.4	665	1.1	442	18	6.0	9.7	13.8	9.2	1.013
15% DME	9.4	636	1.1	1240	42	4.6	9.2	12.1	6.5	0.957
PRF 103.3	9.4	652	1.3	1772	54	5.6	9.5	11.8	6.7	0.992
PRF 107.6	9.4	665	1.1	442	18	6.0	9.7	13.8	9.2	1.013
20% DME	9.1	636	0.9	1185	118	5.15	9.4	12.2	6.9	0.955
PRF 100	9.1	638	1.9	1357	202	6.15	9.8	13.0	8.4	0.919
PRF 103.3	9.1	672	0.8	1054	33	6.06	9.7	12.7	8.0	0.991
30% DME	8.2	607	1.1	1329	155	5.6	9.5	12.0	7	0.924
PRF 94	8.2	618	1.5	1843	178	7.0	10.5	12.6	7.9	0.930
PRF 96	8.2	648	1.2	872	133	7.8	10.7	13.7	10.5	0.923

The combustion properties for RON test fuels and their corresponding PRFs are displayed in Table 4.4. Figure 4.4 presents the in-cylinder pressure traces, AHRR, and KOCA for the RON experiments. Examining the RON data shown in Figure 4.4, it followed the same trend from MON testing for the 100% LPG, 20% and 30% rDME blends where the peak pressure location is more

advanced than the PRFs, but for the intermediate blends 5%, 10%, and 15% rDME the opposite behavior is observed where the average pressure trace is bracketed between the PRFs. The change in behavior is related to the sensitivity of the fuel blends, from Table 4.1 the 5, 10, and 15% blends are all more sensitive than the baseline 100% LPG, 20% rDME, and 30% rDME fuels. RON testing taking place with an IAT of 10 °C, the temperature dependence for more sensitive fuels does not have as drastic of an effect causing the fuels to experience an increase in ignition delay. This phenomenon is observed in the work of Mittal et al. [79] where they examined the autoignition delay for a range of intake temperatures, finding that for more sensitive fuels, the autoignition delay more significantly increased at lower intake temperatures. Comparing the RON IMEP between test fuels, the rDME blends up to 20% DME exhibited the same IMEP as the 100% LPG baseline while reducing the compression ratio (from 9.9 to 8.2). The 30% rDME blend saw a reduction in IMEP by 5% from the baseline value. Comparing the combustion properties of the rDME blends, the addition of DME has no effect on the CA50 until a concentration of 20% rDME is obtained resulting in the CA50 for the 20% and 30% rDME blends to be delayed by 1 crank angle degree. The CA10-50 and CA10-90 times are unchanged between the test fuels and the baseline but the KOCA location for all of the test fuels is delayed from the 100% LPG baseline observed in Table 4.4.

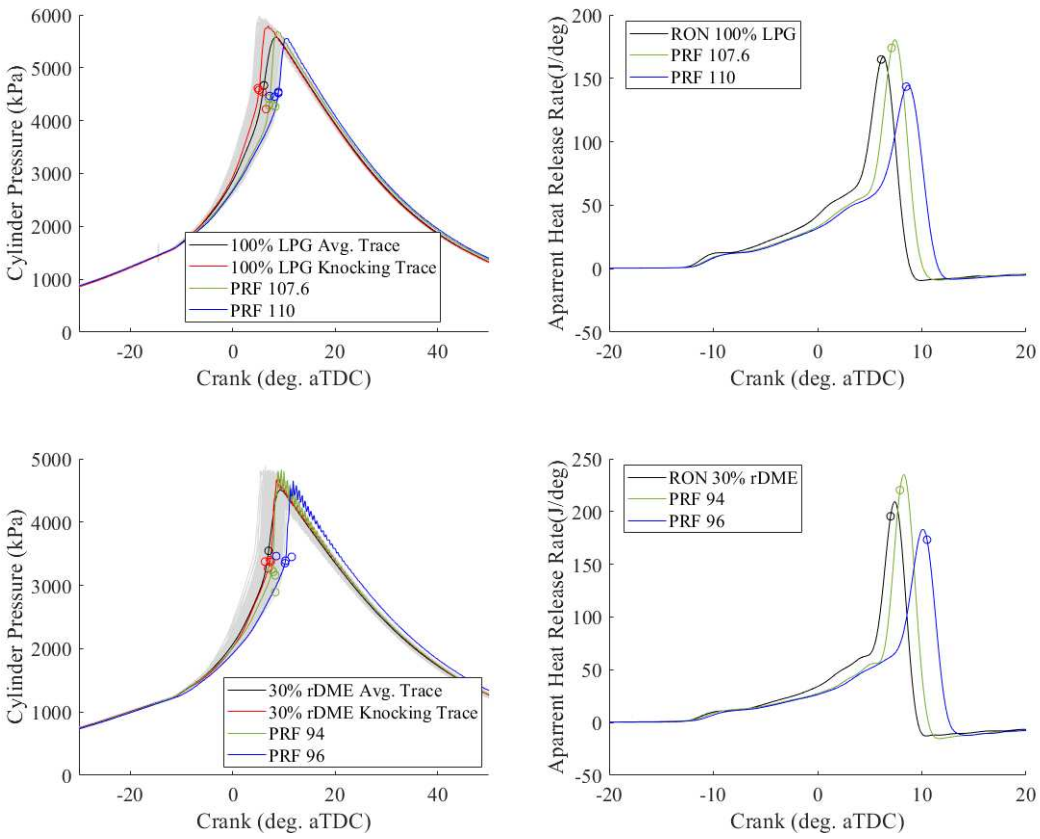

Figure 4.4. RON In-Cylinder pressure trace with knock onset crank angle (KOCA) locations for 100% LPG, 30% rDME and their corresponding bracketing fuels. Average pressure trace is shown for the fuel while a representative knocking cycle is displayed for both the sample fuel and the PRFs. Additionally, the 1000 cycle average Apparent Heat release rates (AHRR).

For the MON and RON experiments, the AHRR is calculated from in-cylinder pressure data utilizing the first law of thermodynamics with a single zone model which does not include the heat losses to walls and crevices [46, 82]. Considering the MON experiments, the test fuels 100% LPG and the LPG/rDME blends all exhibited a more advanced location and a higher maximum peak value observed on the AHRR curves when compared to the bracketing PRFs. The AHRR for both the LPG/rDME mixtures and their PRFs all experienced a rapid rise in slope where this

observation is consistent with the expected physical and chemical behavior of an end gas autoignition (EGAI) event where the volumetric autoignition causes a very rapid heat release, thus creating a steep increase in the slope of the AHRR curve which is consistent with both the MON and RON CFR data indicating medium to heavy autoignition is occurring [83]. The average knock or end gas autoignition onset location obtained over 1000 experimental cycles is displayed on the AHRR traces. The MON and RON experiments KOCA location did not vastly deviate between each other with the RON values falling slightly behind the MON location primarily due to the slower operating speed used for RON testing. When comparing the MON and RON AHRR curves, the RON test fuels do not generate the maximum heat release and are bracketed between the PRFs used at each test condition following the trend of most reactive PRF, test fuel, and lastly the less reactive PRF. These differences observed between test methods are further discussed utilizing chemical kinetic simulations.

4.3 rDME/LPG Chemical Kinetic Simulations

Zero-Dimensional chemical kinetic modeling is a valuable tool to provide insight into the interactions between fuel properties and engine operating conditions. In this study, a numerical investigation was conducted using CONVERGE [48]. Fuel samples that ranged from 100% LPG to 100% rDME were considered for zero-dimensional simulations to obtain insight into the different ignition behavior observed in the CFR engine testing.

For the ignition delay simulations, engine-relevant peak pressures of 3 MPa were chosen to model the observed MON test conditions and the C3 V3.3 mechanism [31] was utilized which is developed by the Computational Chemistry Consortium which consists of NUI Galway, Lawrence Livermore National Laboratory, ITV-RWTH Aachen, CRECK Modeling Lab-

Politecnico di Milano, and Convergent Science. The fuel composition from the provided COAs were used as inputs for the constant volume solver. MON testing requires a mixture temperature of 149 °C – this high intake temperature combined with a compression ratio between 7:1 and 8:1 results in a TDC temperature range around 825 -850K. This corresponding TDC pressure/temperature point for MON testing results in an ignition delay occurring after the NTC region ranging between 1.16- 1.21 on the x-axis of Figure 4.5. The ignition delay simulations show that small concentrations of rDME do not excessively change the ignition delay behavior exhibited by LPG/rDME blends until the concentration of rDME reached 20% for MON operating conditions, this behavior is captured by examining the spacing differences observed between the test fuels' ignition delay curves at this temperature range. At higher temperatures, when observing the 1.16-1.21 region on Figure 4.5, the ignition delay behaviors present for intermediate LPG/rDME blends (5%, 10%, 15%) do not vastly differ between the fuel mixtures. The slight differences present in the ignition delay simulations follow the same trend shown in the experimental MON data. Inside the NTC region, examining 1.24- 1.34 area on the x-axis of Figure 4.5, a small amount of rDME shows a more significant decrease in the ignition delay. At lower temperatures, 1.24-1.58, the spacing and slope differences observed indicate that rDME has a greater effect on ignition at these conditions. Comparing RON and MON testing methods, they are able to capture the ignition delay behavior, for example, considering MON testing, the experimental results indicate that the MON is only reduced by approximately 1.5 between fuels until 30% rDME is reached causing a 6.1 reduction in MON compared to the 20% rDME blend. Examining RON testing, for the intermediate blends, a slight reduction in RON is observed approximately 1.5 between test fuels until 20% rDME where a 3.7 reduction in RON is captured transitioning between 15% to 20% rDME. The ignition delay simulations capture the experimental

behavior and provide valuable insight into the chemical kinetic differences observed between test fuels.

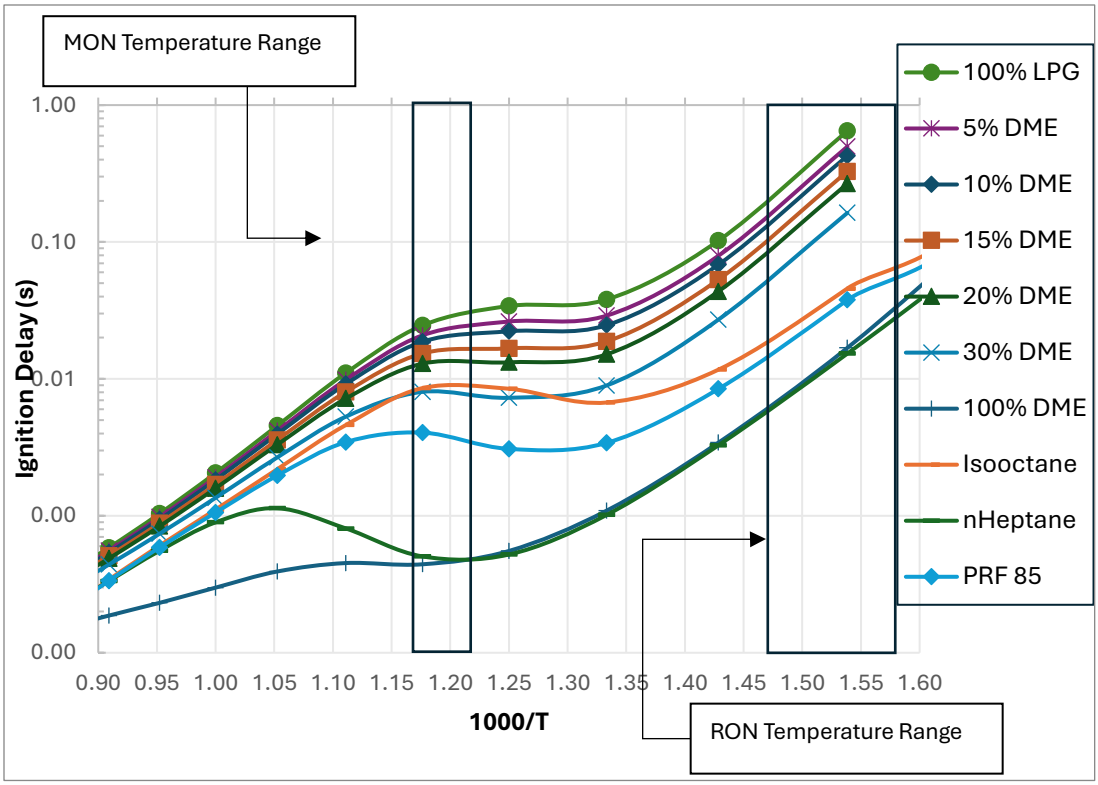

Figure 4.5. Zero-Dimensional CONVERGE Simulations comparing the Ignition delay at 3 MPa and an Equivalence Ratio of 1 between the full range of fuel composition.

For RON testing, the intake air temperature is 10°C but the CR needed to produce a medium knock signal is higher than MON testing ranging between a CR of 8-10. Due to the low intake air temperature, the TDC temperature observed by the engine will be much lower and on the other side of the NTC region (630-680K). RON operating conditions result in ignition delay behavior before the NTC region begins ranging between 1.47-1.58 on the x-axis on Figure 4.5. This ignition behavior creates a wider variation in RON testing between fuel types in this region because the effect of rDME on ignition delay is increased at these conditions seen in Figure 4.5.

The trends observed in the ignition delay simulation agree with results found in literature. The experimental MON and RON results along with previous studies from literature show that concentrations of 20% rDME or lower exhibit similar ignition characteristics to 100% LPG [29, 71, 78]. The ignition similarities between blends up to 20% DME can be explained by the sensitivity trend introduced with Table 4.1. Mittel et al [79] determined that for fuels with higher octane sensitivity RON test conditions would allow these more sensitive fuels to have better antiknock performance while non-sensitive fuels would have better antiknock performance under higher temperatures obtained with MON operating conditions. As DME concentration increases, the octane sensitivity initially increases, achieving a maximum at 10% rDME then decreasing below the initial octane sensitivity obtained with 100% LPG at the 20% rDME blend interval. The 20% and 30% rDME blend reduction in sensitivity indicates that the two fuels will not exhibit the same antiknock performance as the more sensitive intermediate fuel blends (5-15% rDME) and the baseline 100% LPG following the previously observed trends captured in literature and the RON and MON engine tests.

Considering the findings from the kinetic study, the behavior differences observed in the AHRR between the RON and MON testing can be interpreted. In their analysis of binary fuel mixtures of DME/LPG, Dames et al [40] found that propane combustion is enhanced through the low temperature oxidation of DME. DME's low temperature autoignition sequence is engaged through O_2 addition to the CH_3OCH_2 radicals. The gain of OH radicals result in H-abstraction occurring from propane producing n-propyl radicals which initiates the low temperature autoignition for propane. For MON testing, the TDC temperatures reached allow for the addition of DME to engage the autoignition sequence for propane. The higher intake temperature used for MON testing places the TDC temperature on the other side of the NTC region where the fuel

ignition characteristics are able to benefit from the autoignition sequence of both DME and propane creating the maximum AHRR during MON testing. While for RON testing, the lower intake air temperature (IAT) creates TDC conditions that are not at a high enough temperature to promote the autoignition sequence of propane. Dames et al. determined that sensitivities of fuel concentration to H-abstraction by OH from both DME and propane are of opposing magnitudes due to the different overall reactivity between the two fuels at lower temperature conditions. The low temperature chain branching sequence for DME is active at these conditions but for propane it is not effectively creating a radical sink. As discussed by Merchant et al. [84], this is due to the inability of i-propyl to undergo OH producing chain branching reactions which instead goes on to produce HO_2 +propene. The differences observed between the MON and RON AHRR curves are primarily due to the different operating temperatures promoting the autoignition sequence for DME while not promoting that for propane.

Table 4.5
CONVERGE Simulation results vs Experimental data

Fuel Sample	**CONVERGE RON**	**CSU RON**	**CONVERGE MON**	**CSU MON**
100%LPG	>100	108.7 ± 0.2	NA	96.5 ± 0.2
5% DME	>100	107.3 ± 0.2	97.4	94.6 ± 0.2
10%DME	>100	106.7 ± 0.2	95.9	93.2 ± 0.2
15%DME	100	105.1 ± 0.2	93.6	91.9 ± 0.2
20%DME	100	101.4 ± 0.2	91.75	90.3 ± 0.2
30%DME	94.8	95.0 ± 0.2	87.55	84.2 ± 0.2

Table 4.5 displays additional CONVERGE simulations as CONVERGE allows to simulate RON and MON experiments. For the RON and MON simulations of the various LPG/rDME fuel samples conducted in this study, the C3 V3.3 mechanism was used. To evaluate the RON or MON CONVERGE calculates a critical compression ratio (CCR) for the specified fuel which is then

correlated against a reference CCR that is determined for combinations of the PRFs isooctane and n-heptane. To determine the reference CCR, CONVERGE uses the LLNL Gasoline mechanism [85] for its calculations but the user can provide a specified mechanism to create their own reference RON or MON table. The user can also specify both the mechanism and thermodynamic files for the sample fuel. The compression ratio of each PRF is varied and the lowest compression ratio that causes the fuel to auto-ignite is the CCR for that specific PRF which is how CONVERGE creates a correlation between a PRF and CCR. To determine a fuel sample's MON or RON CONVERGE then compares the calculated CCR for the fuel sample to its stored library of reference CCR for PRFs. For both the RON and MON simulations, CONVERGE has limitations as it cannot calculate octane numbers that are over 100. For octane numbers vastly over 100, CONVERGE cannot determine a reference CCR hindering it from being able to make a comparison to the sample fuel's determined CCR [48].

The fuel sample compositions from the Oberon COA were used for these simulations. The trend presented by the CONVERGE MON simulations are consistent with the experimental data. The MON simulation and the experimental data both show a slight reduction in the octane number with increasing concentrations of rDME. The simulations show a greater effect of rDME on the sample fuel properties when the concentration of rDME is increased from 20% to 30%. The CONVERGE RON simulations were hindered by CONVERGE's inability to calculate octane numbers above 100 as LPG has a RON of 109-112. The RON simulations were not able to determine RONs for the 100% LPG, 5% rDME, and 10% rDME because each of them would have a RON above 100. The RON value for the 30% rDME blend, as calculated by CONVERGE, lies within the accepted range defined by experimental uncertainty.

4.4 Conclusions

In the present work, we examine the effects of up to 30% rDME addition to LPG on the ignition characteristics and other combustion properties obtained by the fuel mixtures. Presented in this paper are both the experimental and numerical study of a spark-ignited CFR engine. The main conclusions can be summarized as follows.

1. The MON and RON results indicate that rDME causes a non-linear promoting effect on autoignition of LPG, consistent with other findings in literature. The octane number ratings are relatively insensitive to DME concentration until a larger effect is observed with 20% DME by weight.
2. Measured RON/MON are higher than previously thought and show suitable values for SI engine operation up to 20% rDME blend ratios. The measured AKI values indicate that up to 20% rDME addition results in higher octane numbers than commercially available gasoline while 30% rDME compares well with current standards with an AKI value of 89.7.
3. Additional combustion properties do not vastly deviate from the LPG baseline including CA50, CA10-90, CA10-50, and KOCA. LPG and the LPG/DME blends have a higher sensitivity when compared to traditional fuels indicating a stronger temperature dependence of the autoignition delay time resulting in slower low temperature combustion and faster high temperature combustion. The MON and RON tests display this trend, in MON testing the higher sensitivity test fuels are more advanced than the less sensitive PRFs while during RON testing at lower temperatures, the more sensitive test fuels combustion parameters are delayed when compared to the PRFs.

4. Accurate octane numbers can be calculated with modern in-cylinder pressure transducers compared to the outdated detonation meter. If users utilize a different knock intensity method while understanding the acceptable knock limits of the test engine, octane number ratings that agree with the ASTM standards can be accurately achieved if the bracketing technique is still employed. This work found that two knock intensity metrics produced the same octane rating indicating that the vast difference between the detonation meter and these other knock intensity measurements is the scale that is being employed.

MON/RON experiments indicate that blends up to 20% rDME exhibit similar combustion properties to the baseline 100% LPG while blends of 30% rDME offer similar performance to commercial gasoline. Additional engine testing is required to understand how rDME/LPG blends will perform at higher load conditions under medium and heavy-duty engine operation. Furthermore, to fully utilize this alternative fuel a full emissions analysis at heavy duty operation is required to determine how rDME addition can impact emission formation. The simulation framework is currently being expanded to create a DME/LPG mechanism that is validated for engine operation.

CHAPTER 5 SPRAY PROPERTIES OF LPG AND LPG/DME BLENDS

5.1 Spray Dynamics of LPG/rDME Blends

After completing MON and RON experiments, further analysis was conducted to evaluate the compatibility of these blends with current GDI systems by studying their spray characteristics through high-speed schlieren imaging. Figure 5.1 and Figure 5.2 displays the respective schlieren imaging for all test fuels offering both a visual and quantitative comparison into the spray morphology characteristics by evaluating the vapor-liquid interactions, distinct jets vs single plumes, spray penetration length and widths. Schlieren imaging allows for the vapor and liquid regions to be distinguished from each other creating a deeper insight into the observed spray behavior, where the darker regions present represent the liquid core of the spray while the lighter regions showcase the development of the vapor regions. Figure 5.1 displays the processed images obtained from high-speed schlieren experiments conducted initially at 1 barg chamber pressure for 100% LPG, 30% DME/ 70%LPG and 100% DME at four-time steps: 200 µs, 500 µs, 1000 µs, and 2000 µs all after the start of injection (ASOI). At 1 barg chamber pressure, initially all fuel types exhibit a similar spray pattern where three individual plumes can be distinguished from each other at 200 µs ASOI. As the spray progresses, the 30% DME/70% LPG blend and 100% LPG spray plume interactions cause the individual jets to collapse into one observed plume while for 100% DME the individual spray plumes can still be distinguished from each other differing from 100% LPG and 30% DME/70%LPG test fuels, likely due to the reduced vapor pressure between DME and LPG. In addition to the vapor pressure differences, the DME spray can still be distinguished because of the higher heat of vaporization obtained with DME (22.2 kJ/mol) [86] when compared to propane (19.2 kJ/mol) [87]. At 2000 µs ASOI, the 30% DME/ 70% LPG blend and 100% LPG vaporization appear to be more significant as noted in Figure 5.1 with the presence

of larger lighter regions captured by schlieren imaging denoting the vapor regions. 100% DME also has a greater liquid penetration when compared to the other fuels. Three schlieren experiments were used to obtain the average penetration lengths and widths for all three fuel types which are displayed in Figure 5.3. At 1 barg chamber pressure, 100% DME took the longest to reach the bottom of the spray chamber while 100% LPG and 30% DME blend exhibited the same behavior with both their penetration lengths and widths. In general, the presence of 30% DME did not change the spray characteristics when compared to 100% LPG.

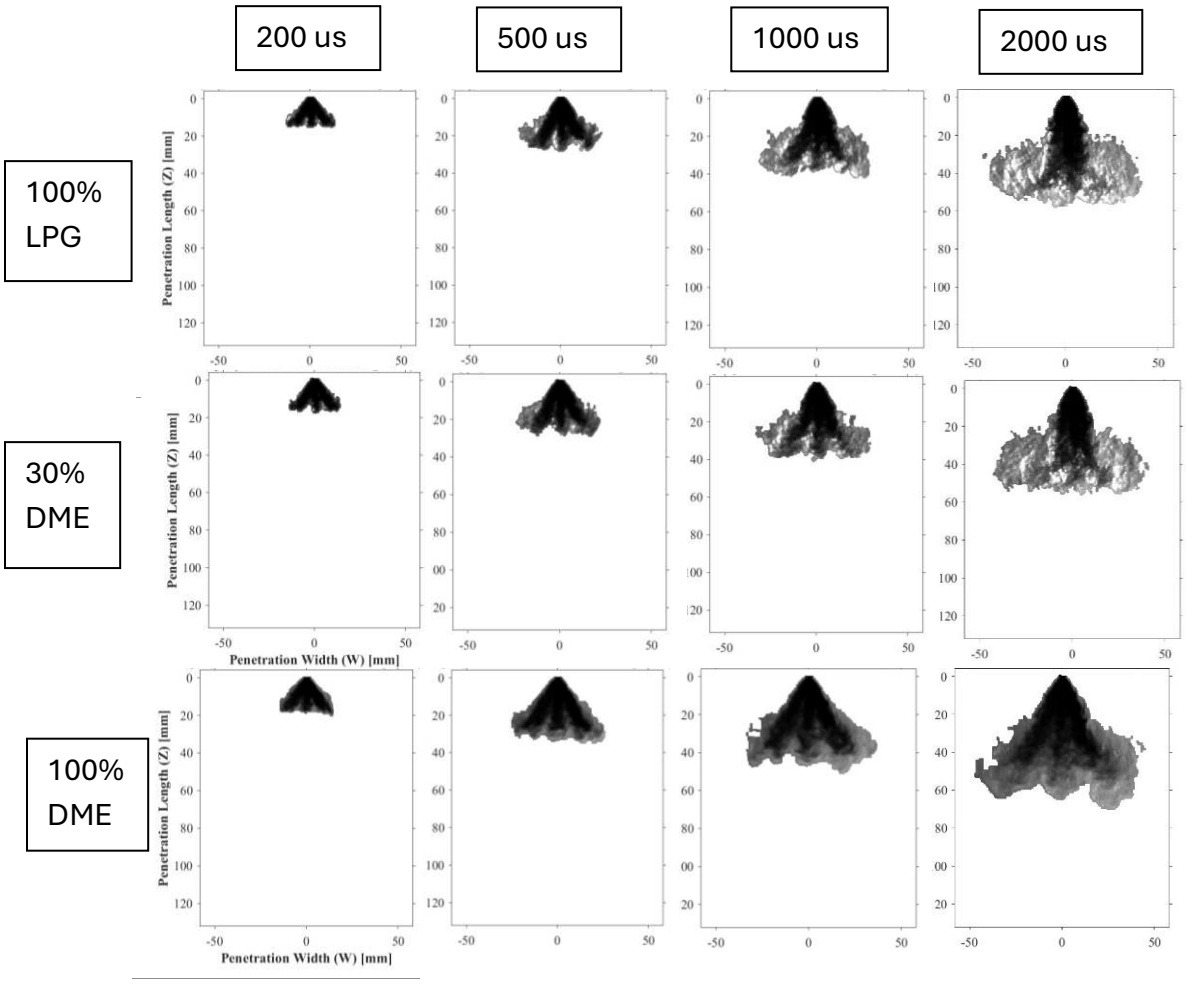

Figure 5.1. Processed Schlieren images for 30% DME, 100% LPG, and 100% DME at 1 barg chamber pressure

Figure 5.2 displays schlieren imaging conducted at 10 barg chamber pressure. The same trend is present for the 30% DME and 100% LPG fuels as the penetration lengths are unchanged for the 30% DME when compared to 100% LPG but a change in the spray behavior is observed with the penetration width of the 30% DME blend as it behaves closer to 100% DME observed in Figure 5.3. At higher chamber pressure conditions, the 100% DME fuel initially has an increased penetration length until 3600 µs where 100% LPG and 30% DME catch up to 100% DME. The penetration length rates are similar across all fuel types during 3600 µs to 5000 µs where after the penetration rate for 100% LPG decreases compared to the two other test fuels. It takes a longer duration for all the test fuels to reach the bottom of the spray chamber. i.e., 10,000 µs compared to 2,400 µs for the lower chamber pressure test condition. Similar to the 1atmg sprays, each fuel type experiences a collapse of the individual nozzle jets into a single plume and the 100% LPG and 30% DME/ 70% LPG blend exhibit an increase in vaporization/flash boiling of the initial liquid fuel injection.

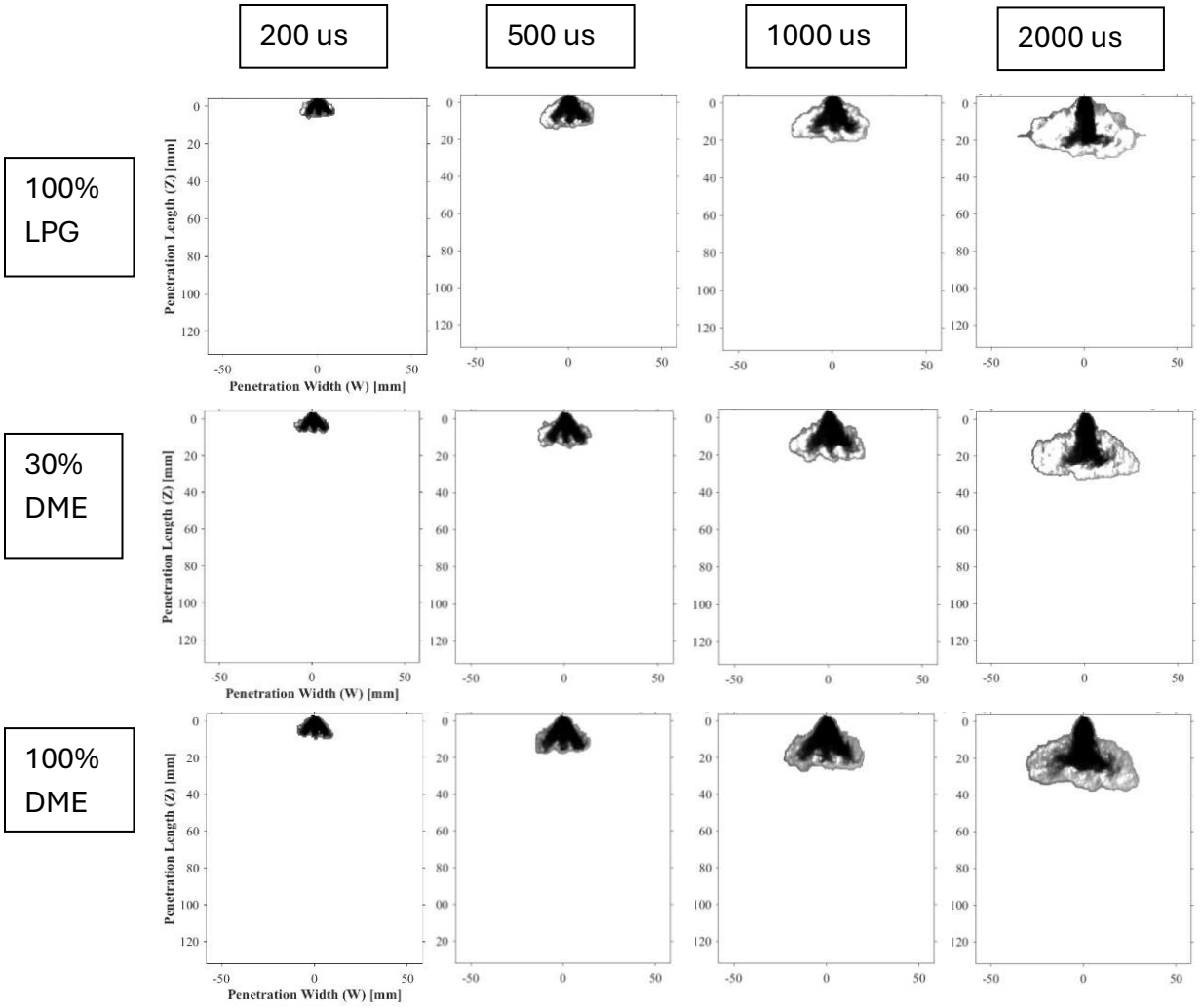

Figure 5.2. Processed schlieren images for 30% DME, 100% LPG, and 100% DME at 10 barg chamber pressure

All fuel types, regardless of composition, eventually develop a characteristic tulip-like shape due to the interaction of individual spray plumes. This phenomenon results in the collapse of multiple jets into a single jet after approximately 2000 μs, observed under both high and low chamber pressure conditions. However, distinct differences are observed between fuel types in terms of spray behavior and jet duration. For 100% DME, the individual liquid jets remain distinguishable for a longer period compared to the other test fuels. Specifically, at lower chamber

pressures, 100% DME maintains its distinct jets longer, while 100% LPG and the 30%DME/70% LPG blend fully collapse into a single jet.

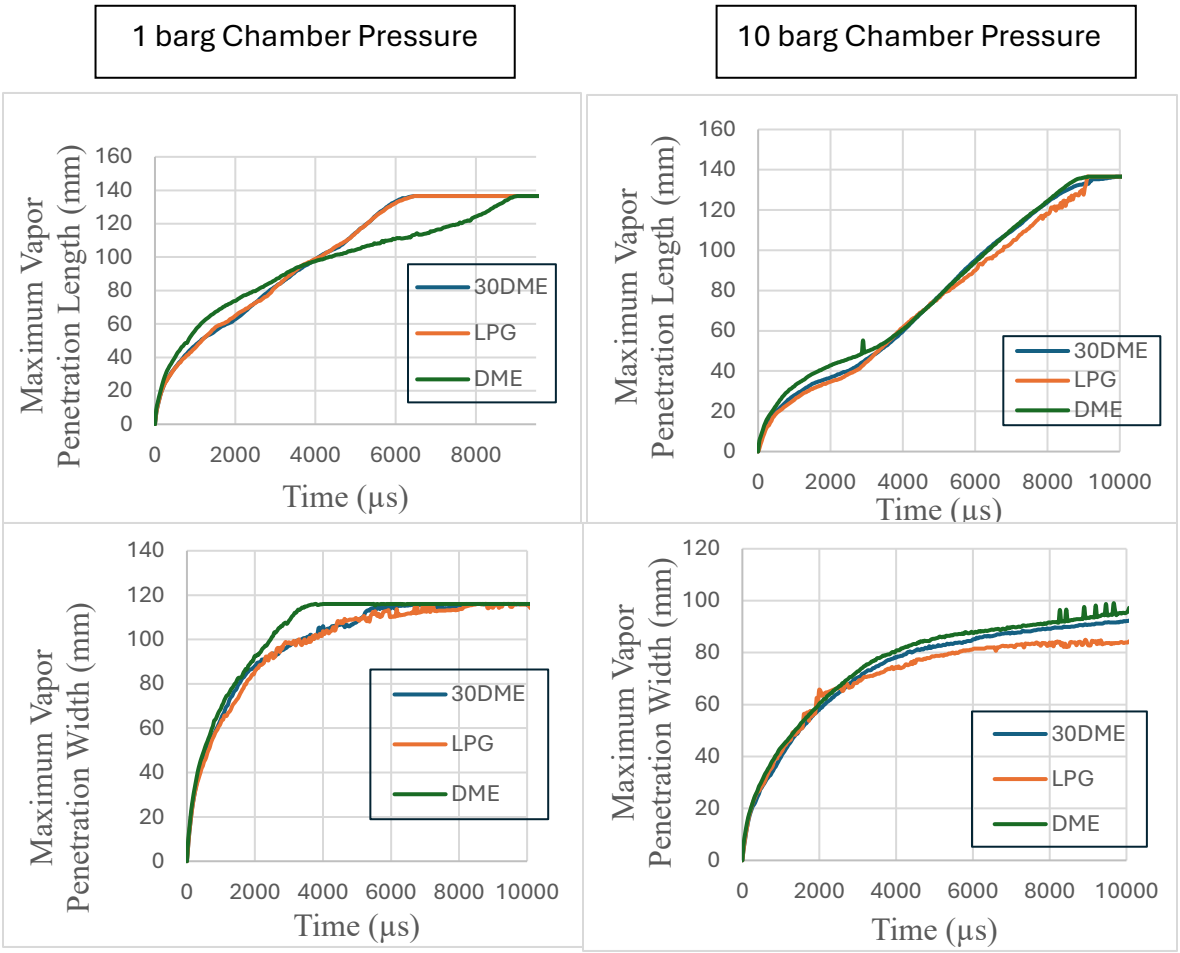

Figure 5.3. Spray penetration length and spray penetration width data taken at two chamber pressures. Comparing the spray dynamics between the three test fuels.

When comparing 100% LPG to the 30% rDME/LPG blend, the spray structure, penetration width, and penetration length exhibit minimal differences despite the addition of DME. The spray behavior of the blended fuel closely resembles that of 100% LPG, indicating that injectors

optimized for 100% LPG can be used without modification for the 30% DME blend. Consequently, direct injection (DI) systems designed for LPG can be directly adapted to rDME/LPG blends without requiring changes to system operational parameters, such as injection pressure or injection duration.

The results from high-speed schlieren imaging further suggest that up to a 30% DME concentration, both premixed and direct injection combustion approaches remain viable without necessitating modifications to the overall system.

5.2 Conclusions

1. Between 100% LPG and the 30% rDME/LPG blend the spray structure, penetration widths and penetration lengths do not vastly change with the addition of DME, thus allowing DI systems that have been designed for LPG to be utilized for up to 30% rDME addition with no modifications required.

CHAPTER 6 – LPG/DME BLENDS: OPERATION IN A BOOSTED MEDIUM TO HEAVY DUTY SPARK IGNITED ENGINE

6.1 Combustion and Performance Characteristics

This section reviews the experimental results of LPG/DME blends tested in a heavy-duty, spark-ignited Cummins X15 engine under boosted conditions. The experimental methodology is detailed in Section 2.5, while Section 2.1 provides an overview of the X15 test cell architecture and experimental setup. Figure 6.1 presents the Brake Thermal Efficiency (BTE) and Brake Mean Effective Pressure (BMEP) plotted against the experimental CA50 range. Natural gas (NG) exhibited both the lowest BTE and BMEP among all test fuels. Following NG, the BTE for the10% DME blend performed lower than the other LPG/DME based fussels. In ascending order of BTE, the test fuels are categorized as follows: 15% DME, 5% DME, 100% LPG and 20% DME. While only the 20% DME test fuel resulted in a higher BTE than LPG, at later CA50 timings, the 5%, 15% and 20% DME blends all performed better than the baseline 100% LPG. The 100% LPG blend achieved better performance than the 5% and 15% DME blends at an early CA50 timing of 7.5° aTDC. While earlier CA50 timings for 15% DME were not taken it is unclear whether it would continue to trend upward, achieving a peak BTE and then falling back down. While 20% DME achieved the highest BTE of 42.9%, a 0.5% difference from 100% LPG value of 42.7%, the other test fuels achieved comparable performance metrics to the 100% LPG baseline. The 15% DME max BTE of 41.9% results in a 1.9% difference while the 5% DME BTE of results in a 1.4% percent difference. The 10% DME blend deviated the most from the LPG baseline with a 6% difference between BTE values. Notably, BMEP trends did not directly mirror the BTE order; instead, BMEP values across all cases remained tightly coupled between 9.8 and 12 bar.

A comprehensive summary of the combustion performance metrics and characteristics for each fuel is provided in Table 6.1. As DME concentration increased from the 100% LPG baseline, BMEP initially rose by 4.4% at the 5% DME level. However, further increasing the blend concentration to 10% and above reversed this trend, with BMEP returning to levels comparable to the 100% LPG baseline. Regardless of the blend ratio, both the LPG baseline and all LPG/DME mixtures maintained a higher BMEP than natural gas at identical test conditions. The observed BTE trends are primarily attributed to the fraction of end-gas autoignition (f-EGAI) occurring in-cylinder. The f-EGAI values are summarized in Table 6.1, alongside the Knock Onset Crank Angle (KOCA) and Maximum Amplitude of Pressure Oscillations (MAPO). This f-EGAI metric, developed by Zdanowicz et al. and enhanced by Bestel et al. [88, 83], quantifies the energy contribution of the autoignition event relative to the total heat release. At the highest BTE points for NG, zero autoignition was detected, a finding confirmed by the f-EGAI metric and the normalized Apparent Heat Release Rate (AHRR) in Figure 6.2. In contrast, the 100% LPG baseline exhibited EGAI Type 1, indicating light-to-medium autoignition activity. According to the f-EGAI metric, approximately 11.6% of the total energy release in the LPG case is attributed to autoignition. The addition of DME significantly intensified this phenomenon; for the 5% DME case, the f-EGAI increased to 21.5%, representing nearly a 100% increase in autoignition energy compared to the LPG baseline. This significant increase in reactivity is responsible for both the efficiency gains over the LPG baseline and the elevated BMEP observed in the 5% DME case, which yielded the highest BMEP among all tested fuels.

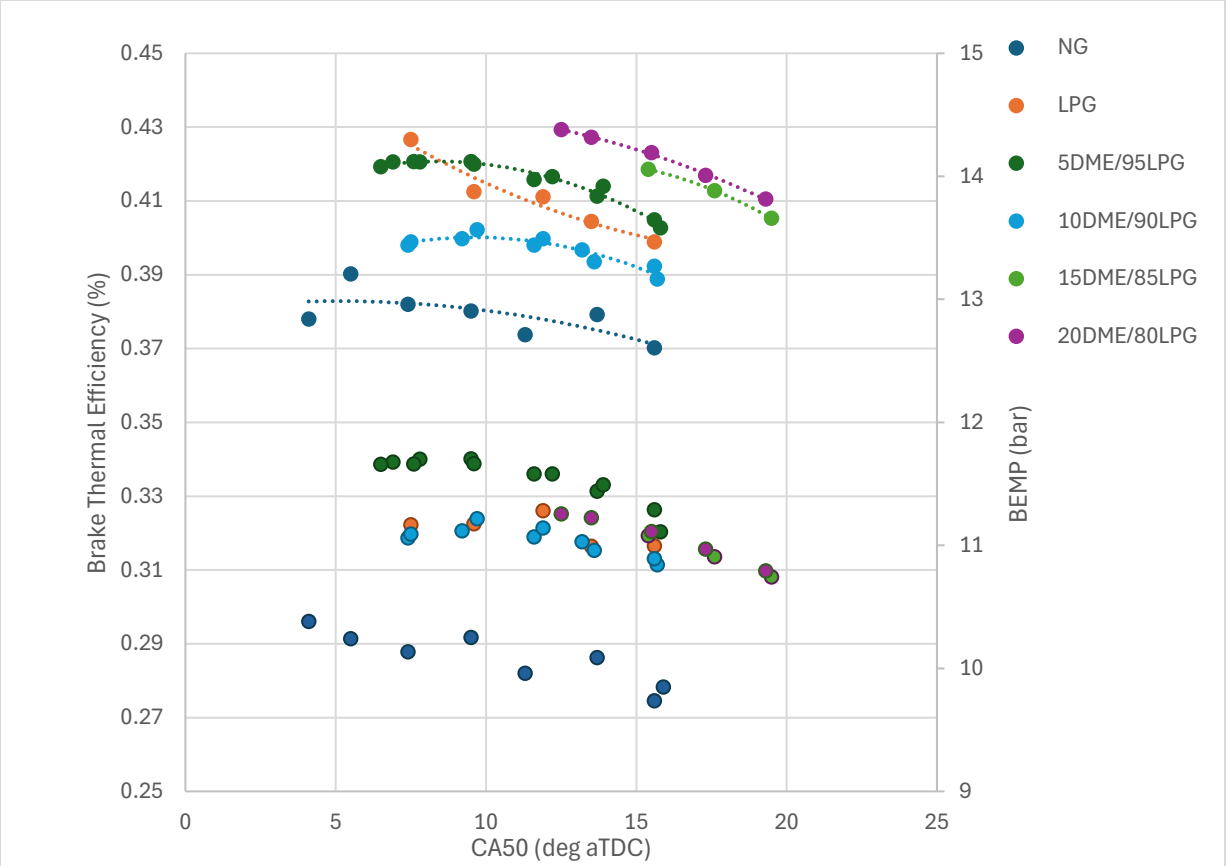

Figure 6.1 BTE and BMEP vs CA50 for high load test conditions.

The transition from the(NG baseline to 100% LPG and LPG/DME blends resulted in a significant reduction in the CA10-90 burn duration. As summarized in Table 6.1, the 100% LPG baseline achieved a reduction in burn duration of approximately 3–5 crank angles across the entire CA50 sweep compared to NG. Interestingly, the addition of DME to the LPG base did not result in further drastic changes to the CA10-90 duration; in most cases, the duration remained nearly identical to the 100% LPG baseline or increased slightly by only 1 crank angle. These findings are highly consistent with the CFR engine testing (MON and RON) results detailed in Section 4.2. This suggests that while DME significantly influences the end-gas autoignition the primary flame propagation is dominated by the LPG base.

Table 6.1. Combustion and Performance Experimental Data

Fuel	CA50	CA10-90	BTE (%)	BMEP (bar)	f-EGAI (%	KOCA (deg)	MAPO (bar)	THC (C1 Basis) (PPM)	O2 (%)	Nox (PPM)	CO2 (%)	CO (PPM)
Natural Gas	15.9	16.5	38.1	9.8	10.5	9.9	2.76	350	0.56	1738	9.5	1565
	15.6	16.1	37.0	9.7	10.9	9.8	2.75	380	0.48	1546	9.5	2175
	13.7	15.8	37.9	10.1	5.2	12.7	2.77	375	0.51	1653	9.5	1378
	11.3	15.0	37.4	10.0	3.1	15.1	2.76	397	0.44	1563	9.5	1735
	9.5	15.2	38.0	10.3	3.2	14.6	2.76	381	0.54	1706	9.4	1369
	7.4	14.9	38.2	10.1	2.0	14.2	2.74	394	0.50	1589	9.4	2274
	5.5	15.2	39.0	10.2	0.4	15.8	2.75	375	0.60	1759	9.4	1735
	4.1	17.7	37.8	10.4	0.2	12.7	2.71	373	0.58	1717	9.3	1573
LPG	15.6	13.8	39.9	11.0	7.4	14.0	2.82	278	0.57	1842	10.8	2695
	13.5	13.4	40.4	11.0	3.9	20.2	2.77	270	0.60	1849	10.8	2607
	11.9	14.8	41.1	11.3	1.9	20.8	2.76	295	0.59	1846	10.8	2532
	9.6	13.0	41.3	11.2	4.7	16.8	2.81	315	0.60	1871	10.8	2706
	7.5	12.4	42.7	11.2	11.6	12.0	3.16	322	0.77	2070	10.7	2084
5% DME	15.6	13.7	40.5	11.3	11.2	11.9	2.79	305	0.53	1823	10.8	2200
	13.7	14.0	41.1	11.4	4.5	18.5	2.74	314	0.54	1825	10.8	2032
	11.6	13.5	41.6	11.6	3.2	20.0	2.69	326	0.54	1854	10.8	1984
	9.5	12.7	42.1	11.7	6.8	16.3	2.81	337	0.55	1872	10.8	2020
	7.8	12.8	42.1	11.7	16.7	11.7	3.53	356	0.56	1892	10.8	2051
	6.9	12.7	42.1	11.7	21.5	10.1	4.74	369	0.57	1912	10.8	2045
	6.5	11.8	41.9	11.7	21.3	10.0	4.77	368	0.57	1910	10.8	2078
	7.6	12.2	42.1	11.7	17.7	11.5	3.65	347	0.57	1902	10.7	2079
	9.6	12.7	42.0	11.7	7.9	15.8	2.82	333	0.58	1879	10.7	2076
	12.2	13.5	41.7	11.6	3.1	20.1	2.65	318	0.59	1850	10.7	2091
	13.9	14.6	41.4	11.5	3.4	20.9	2.68	302	0.60	1851	10.7	2107
	15.8	14.8	40.3	11.1	9.7	13.7	2.68	269	0.69	1913	10.7	2115
10% DME	15.7	13.8	38.9	10.8	13.7	12.6	2.66	283	0.57	1843	10.7	2255
	13.6	13.1	39.4	11.0	9.1	16.4	2.70	287	0.57	1840	10.7	2201
	11.6	12.7	39.8	11.1	9.4	16.7	2.76	306	0.59	1876	10.7	2145
	9.2	12.3	40.0	11.1	17.1	13.0	3.41	323	0.59	1894	10.7	2149
	7.4	11.4	39.8	11.1	24.5	10.6	5.33	338	0.59	1905	10.7	2206
	7.5	11.5	39.9	11.1	23.8	10.7	5.18	339	0.60	1911	10.7	2187
	9.7	12.8	40.2	11.2	8.6	15.1	2.86	329	0.61	1867	10.7	2295
	11.9	13.5	40.0	11.1	5.8	18.6	2.70	319	0.60	1850	10.7	2267
	13.2	13.7	39.7	11.0	9.2	16.4	2.73	307	0.59	1837	10.7	2248
	15.6	13.1	39.2	10.9	16.6	11.0	2.70	286	0.57	1806	10.7	2284
15% DME	19.5	15.2	40.5	10.7	28.2	10.2	2.86	-	-	-	-	-
	17.6	15.0	41.3	10.9	20.2	10.4	2.94	-	-	-	-	-
	15.4	13.8	41.9	11.1	11.4	13.3	2.93	-	-	-	-	-
20% DME	19.3	14.3	41.0	10.8	30.2	10.6	2.88	-	-	-	-	-
	17.3	13.5	41.7	11.0	21.3	11.7	2.97	-	-	-	-	-
	15.5	12.8	42.3	11.1	15.2	15.7	3.28	-	-	-	-	-
	13.5	12.0	42.7	11.2	20.8	14.9	4.56	-	-	-	-	-
	12.5	11.7	42.9	11.3	28.8	14.0	5.87	-	-	-	-	-

Conversely, the 10% and 15% DME blends exhibit a decrease in both BTE and f-EGAI compared to the 100% LPG baseline and the 5% DME case at the most retarded CA50 test points.

The normalized AHRR traces for these intermediate blends indicate only minimal or light autoignition activity. In these specific cases, the CA50 timing serves as the primary governor for the intensity of the autoignition event. For the 10% DME fuel, the relationship between phasing and reactivity is highly sensitive. At a retarded CA50 of 16° aTDC, the f-EGAI averages 15.2%. As the combustion phasing is advanced toward TDC, the f-EGAI initially fluctuates before achieving a maximum value of 24.2% at a CA50 of 8° aTDC. This intensification of the autoignition event is corroborated by the MAPO values, which rise to 5.25 bar at this advanced timing, indicating a shift toward more aggressive end-gas kinetics. Interestingly, the BTE for the 10% DME case does not deviate significantly during this CA50 sweep, suggesting that the efficiency gains from increased autoignition are being offset by other thermodynamic factors or heat transfer losses at this concentration. A definitive performance threshold is reached at the 20% DME concentration. At this level, the BTE rises back above the 100% LPG baseline, driven by a significantly stronger EGAI event. This represents a regime shift where the combustion transitions from Type 1 to Type 2 EGAI. The transition to Type 2 EGAI culminated in the 20% DME blend achieving the highest overall performance metrics of the study. This blend exhibited both the highest BTE and the highest average f-EGAI across the tested range. Specifically, at a CA50 of 12.5° aTDC, the 20% DME case produced its peak BTE, coinciding with an f-EGAI of 28.8% and a MAPO of 5.87 bar. The MAPO knock intensity metrics support this transition, with the 5% and 20% DME blends consistently exhibiting higher pressure oscillations compared to the 10% and 15% blends, as well as the NG and LPG baselines. These experimental findings demonstrate that while DME generally increases reactivity, its impact on engine efficiency is governed by a complex interplay between blend ratio and combustion phasing.

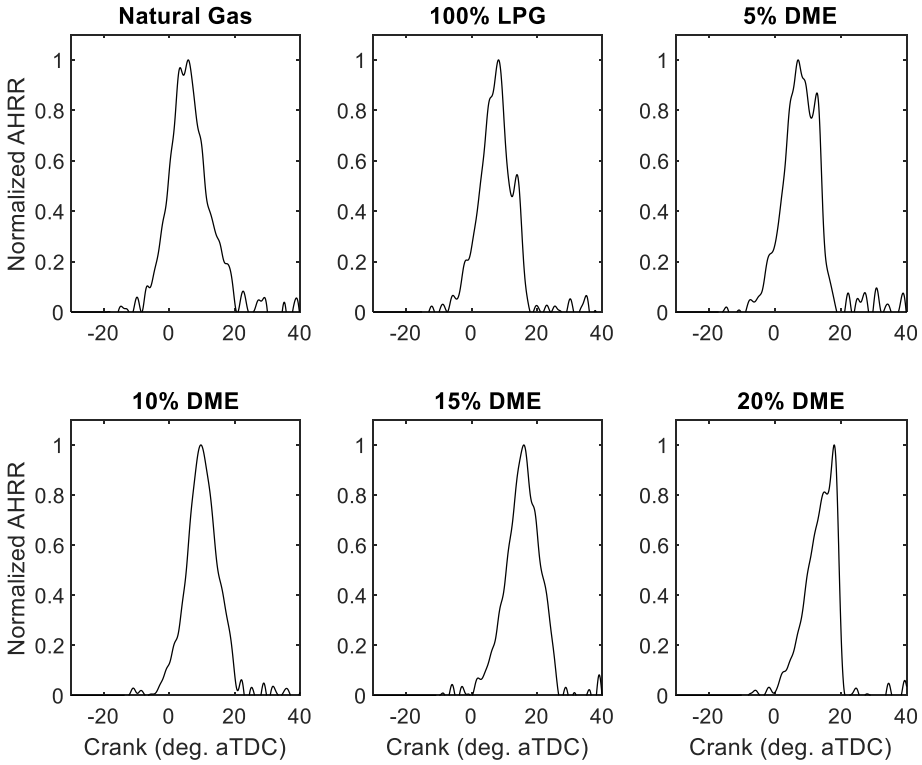

Figure 6.2. Normalized AHRR rate for highest BTE condition

These results underscore a critical trade-off: while the 20% DME blend provides superior thermodynamic efficiency by accelerating the late-stage energy release, the resulting MAPO levels approach possible knock limits of the engine hardware. This specific operating point—characterized by high efficiency coupled with high knock intensity serves as the primary validation target for the CONVERGE 3D engine simulations. To safely optimize the use of such high-reactivity blends, the computational tools must be capable of resolving the exact chemical triggers that lead to this 28.8% autoignition fraction. Figure 6.3 compares the highest BTE cases for each fuel type, illustrating the significant differences in CA50 and peak cylinder pressure. The fuels exhibit the following order of decreasing PCP: 5% DME blend, 100% LPG baseline, NG, 10% DME, 20% DME and lastly 15% DME. The lower PCP observed for the 20% and 15% DME blends is primarily attributed to their more retarded CA50 timing compared to the other test fuels.

Despite the later combustion phasing, the 20% blend maintained high efficiency, further validating that the increased autoignition fraction (f-EGAI) compensates for the expansion work losses typically associated with retarded timing. The 5-gas emission analysis indicated that THC emissions remained constant across all fuels. NOx emissions decreased from the LPG baseline but remained higher than the NG data, while CO2 percentage and CO PPM emissions increased with DME addition but still produced comparable metrics to the LPG cases.

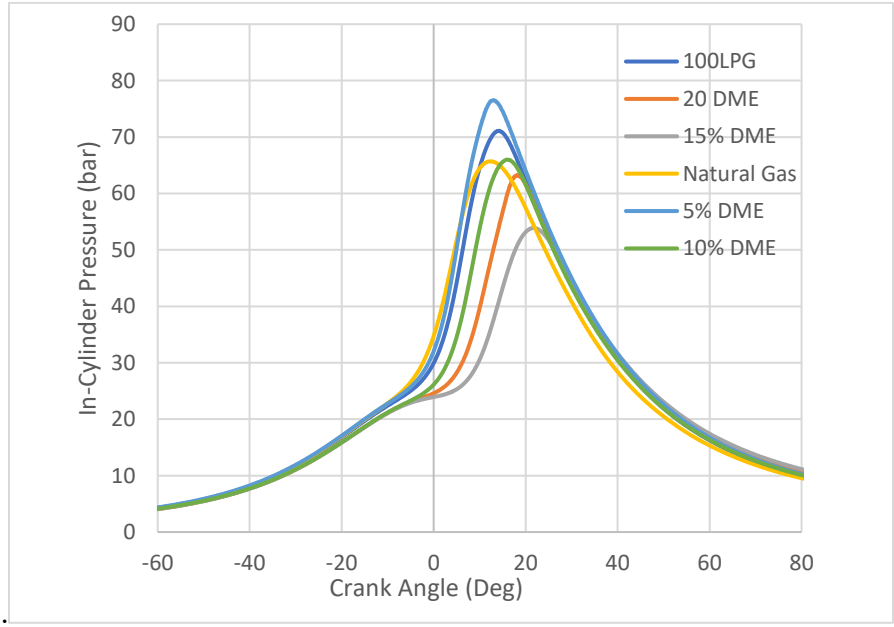

Figure 6.3. Experimental Mean In-cylinder pressure of the highest BTE condition for each test fuel.

A critical metric for the viability of alternative fuel blends is the stability of the combustion process across varying blend ratios and engine loads. For all tested operational points, each LPG/DME blend exhibited a COV IMEP of less than 3%, which is widely considered the threshold for stable engine operation. The majority of the experimental data clustered around a COV IMEP

of 1.25%, demonstrating that the Cummins X15 platform maintained highly consistent cyclic combustion regardless of the DME concentration. This high degree of stability is significant because it indicates that even at the 20% DME concentration where the engine experienced strong Type 2 EGAI—the autoignition events were phase-locked and predictable rather than erratic. This consistency ensures that the performance gains observed in BTE and BMEP are reliable and that the engine can be effectively controlled using standard ECU strategies, even when operating near the knock limit.

6.1.2 Reduced Load experimental results

This section details the experimental engine test results under reduced load conditions. Figure 6.4 illustrates the BTE and BMEP trends graphed against the CA50 sweep values for a new natural gas baseline compared against 20% and 30% DME blends. While there are small deviations of the BMEP with the values ranging from 6.5 to 7.6 bar, the LPG/DME blends outperformed the NG baseline while at identical experimental conditions. This performance gap highlights the dramatic increase in efficiency achievable through fuel blending at lower loads.

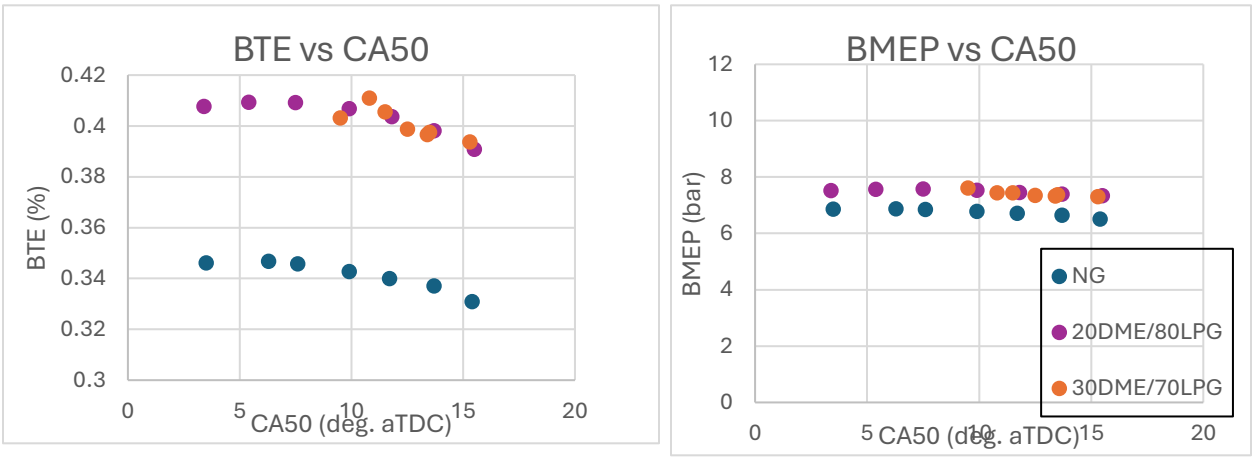

Figure 6.4. BTE and BMEP vs CA50 at low load test condition for Natural Gas, 20% DME, and 30% DME.

The impact of fuel reactivity on low-load performance is most clearly evidenced in Figure 6.4, which compares the BTE of the NG baseline against the 20% and 30% DME blends across a CA50 sweep. There is a definitive vertical shift in the efficiency frontier. While the NG baseline struggles to exceed 34.6% BTE, the 20% and 30% DME blends consistently operate above 39%, with the 30% DME blend peaking at 41.1% and the 20% DME blend peaking at 40.9%. The NG baseline shows a rapid decline in efficiency as CA50 is retarded beyond 10° aTDC, likely due to the slow laminar flame speed of methane at reduced pressures leading to incomplete or late combustion. In contrast, the LPG/DME blends exhibit a much flatter profile. Even at a retarded CA50 of 14° aTDC, the 20% and 30% DME blend maintains an efficiency level nearly 6 percentage points higher than the best-performing NG case. This data suggests that the chemical acceleration provided by the DME/LPG mixture effectively mitigates the expansion-stroke cooling that typically hampers NG efficiency. By maintaining a faster burn rate (as seen in Table 6.2 with the CA10-90 trends), these fuels allow for a more effective conversion of chemical energy into work, even when combustion is phased later in the cycle to potentially manage emissions.

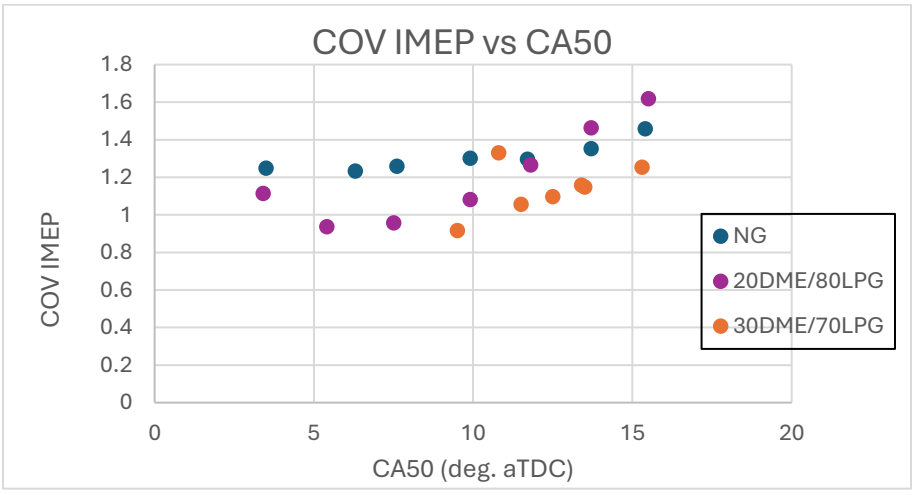

Figure 6.5. COV IMEP vs CA50 at low load experimental tests for Natural Gas, 20% DME, and 30% DME.

Figure 6.5 illustrates the COV IMEP trends for the low-load sweep. Stability remains excellent across all test cases, with all values staying well below the 3% industry threshold for stable operation. Despite the high chemical reactivity of the 30% DME blend, COV values (ranging from 0.9% to 1.3%) are often lower than the NG baseline at comparable CA50 timings. While all fuels show a slight upward trend in COV as CA50 is retarded toward 16° aTDC, the 30% DME blend remains notably more stable than the 20% blend at the most retarded points. This tight clustering of COV data suggests that the engine control unit (ECU) can reliably manage these high-DME blends without fear of misfire or partial burn, even when utilizing late phasing.

Table 6.2 Combustion and Performance Experimental Data for Natural Gas, 20% and 30% DME blends at reduced BMEP.

Fuel	CA50	CA10-90	BTE (%)	BMEP (bar)	f-EGAI (%)	KOCA (deg)	MAPO (bar)
Natural Gas	15.4	16.6	33.1	6.5	4.8	11.1	2.8
	13.7	16.5	33.7	6.6	3.1	9.3	2.8
	11.7	16.2	34.0	6.7	1.5	NA	2.8
	9.9	16.7	34.3	6.8	0.9		2.8
	7.6	16.0	34.6	6.8	0.3		2.9
	6.3	19.9	34.7	6.9	0.2		2.9
	3.5	15.8	34.6	6.9	0.1		2.9
20% DME	15.5	14.8	39.1	7.3	10.0	10.9	2.8
	13.7	15.3	39.8	7.4	5.6	14.2	2.8
	11.8	15.0	40.4	7.4	2.3	16.7	2.8
	9.9	15.0	40.7	7.5	2.0	15.3	2.8
	7.5	13.5	40.9	7.6	3.5	12.1	2.9
	5.4	13.2	40.9	7.6	10.6	8.9	3.1
	3.4	12.8	40.8	7.5	18.0	6.8	3.7
30% DME	9.5	12.2	40.3	7.6	30.5	10.9	5.5
	15.3	13.3	39.4	7.3	16.4	17.3	4.4
	13.4	12.7	39.7	7.3	20.8	14.8	5.8
	13.5	13.0	39.7	7.4	18.9	14.9	4.3
	12.5	12.6	39.9	7.3	19.7	14.0	5.1
	11.5	13.4	40.5	7.4	19.2	12.8	3.6
	10.8	13.8	41.1	7.4	17.3	12.4	3.1

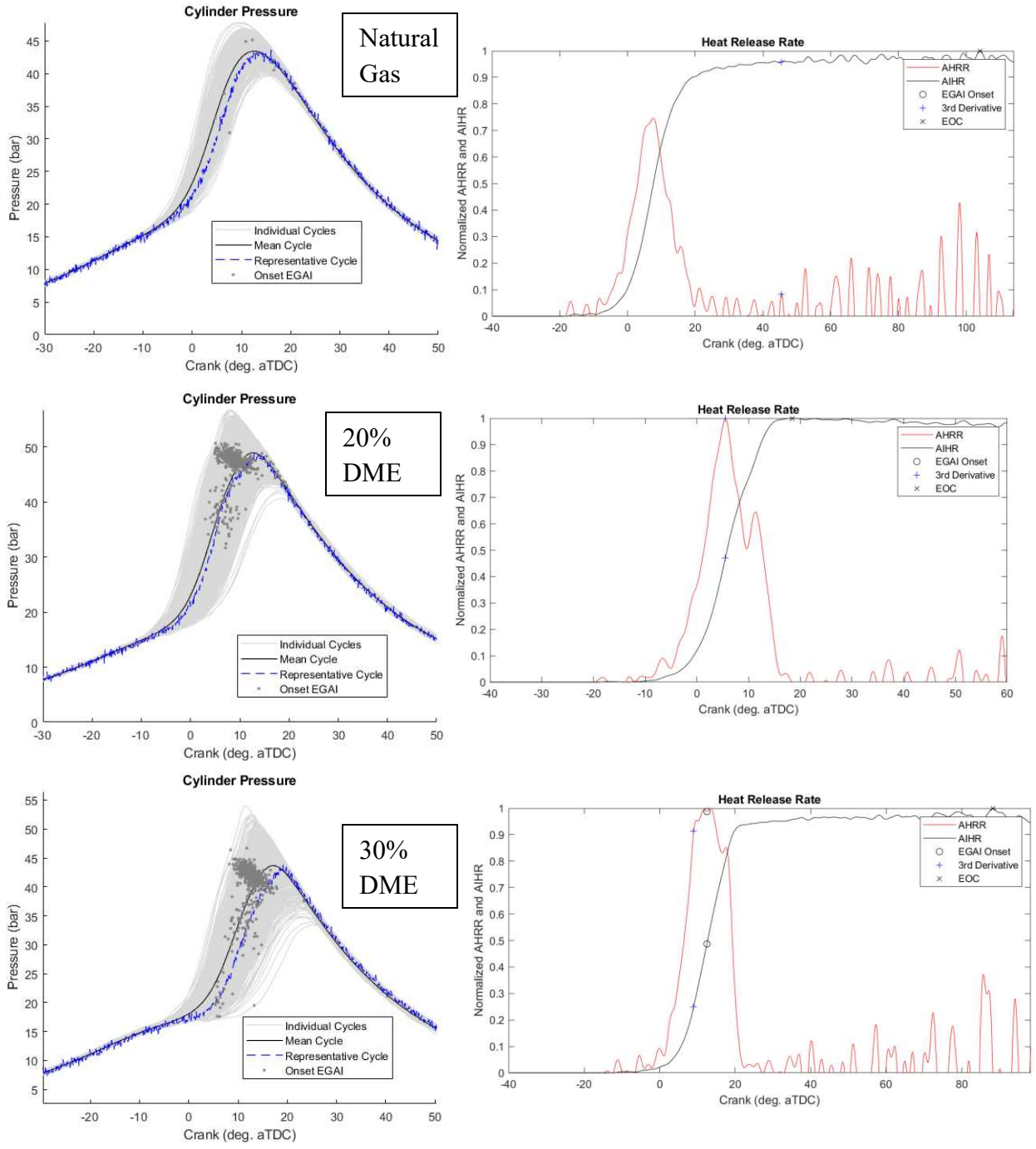

Figure 6.6. Experimental In-cylinder average pressure and the 1000 cycle spread coupled with the normalized apparent heat release rate and apparent integrated heat release for all test fuels.

Table 6.2 presents a comprehensive overview of the performance and combustion characteristics of the LPG/DME blends compared to the NG baseline, highlighting several key

trends in reactivity and efficiency. The f-EGAI results at lower loads trend similarly to the high-load operation; specifically, the NG baseline does not exhibit any autoignition and maintains a consistent MAPO, indicating zero knock across all timing points. In contrast, the LPG/DME blends present significant f-EGAI for every tested CA50, particularly in the 30% DME cases where the f-EGAI ranges from 16% to 30%. The 20% DME blend shows a more moderate response, with f-EGAI values ranging from 3% to 18%. For these LPG/DME blends, the f-EGAI is directly related to the CA50 timing, where timings closer to TDC result in higher f-EGAI compared to delayed timings around 15° aTDC. This relationship is further supported by the MAPO values for 30% DME, as the highest recorded MAPO corresponds to the peak f-EGAI of 30.5%. Interestingly, the MAPO values for the 20% DME fuel did not deviate from the NG baseline until f-EGAI values rose above 18%. This suggests that at lower loads, the energy released from end-gas autoignition aids in the achievable work without the risk of damaging engine hardware.

A pivotal finding in this data is that the highest BTE case for 30% DME achieved substantial EGAI (17.3%) while producing a MAPO of only 3.1 bar. This value does not deviate from the MAPO levels observed during standard NG operation, highlighting that if the CA50 timing is optimized, these highly reactive LPG/DME blends are entirely viable for heavy-duty engine operation. This constructive autoignition allows the engine to reach its peak efficiency of 41.1% while remaining well within the mechanical safety limits.

Figure 6.6 provides a direct comparison of the experimental in-cylinder pressure traces—encompassing the full 1,000-cycle dataset and the AHRR for the peak BTE cases of each fuel. The addition of DME significantly elevates the pressure profile of the engine, with the 20% and 30% DME blends exhibiting an increase in peak cylinder pressure of 5–10 bar relative to the natural gas baseline. This expansion of the peak pressure envelope is a primary contributor to the observed

BTE gains, as it represents a higher degree of constant-volume combustion and improved expansion work.

The AHRR traces further elucidate the behavioral shift between the fuels; while the NG baseline demonstrates a smooth profile with zero EGAI activity, both the 20% and 30% DME cases clearly indicate the presence of Type 1 EGAI. The presence of this autoignition "bump" in the heat release rate confirms that the DME is successfully sensitizing the end-gas to react before the arrival of the primary flame front. Crucially, the 1,000-cycle pressure overlays show that even with this increased peak pressure and autoignition activity, the combustion remains stable and repeatable, reinforcing the viability of these blends for high-efficiency operation in the Cummins X15 platform.

LPG/DME enhancement is particularly significant at reduced loads, where lower in-cylinder temperatures often lead to sluggish combustion and increased time-losses in NG-fueled engines. The addition of DME, even at these lower pressures, appears to provide the necessary chemical acceleration to maintain a fast, efficient burn rate. These results suggest that high-reactivity blends offer a dual benefit: they provide the potential for high-power density at boosted conditions (as seen in Section 6.1) and recovery of lost efficiency during throttled or lower-load operation.

6.2 Chemical Mechanism Validation

6.2.1 Ignition Delay 0D Simulations

As described in the introduction, very few established chemical kinetic mechanisms possess the requisite reaction pathways for both LPG and DME. An initial review identified the UCSD, RC3, ARAMCO 3.0, and Huang Mod Mech C5 as potential candidates for predicting the

combustion performance of these blends. However, several practical constraints dictated the selection process and ultimately required a customized approach. The Huang Mod Mech C5 was excluded due to the absence of a transport property file, which is essential for accurate 1D flame speed analysis and 3D-CFD. Furthermore, while the ARAMCO 3.0 and RC3 mechanisms are chemically comprehensive, their vast size was deemed computationally prohibitive for the intensive 3D engine simulations required in this study.

Consequently, this work sought to develop a more efficient numerical tool by hybridizing established frameworks. Two high-fidelity DME sub-mechanisms, LLNL and the UCSD base DME, were selected for integration into existing LPG-centric frameworks, specifically the USC and the CSU generated ALPINE 153 mechanisms. The species and reactions for the UCSD DME mechanism are detailed in section 2.6 while the 79 species and 351 reactions of the DME LLNL mechanism are not described. The blended mechanisms are referred to as USC_LLNL, ALPINE_LLNL, and ALPINE-DME 158. To validate these newly developed hybrid frameworks, this section utilizes experimental rapid compression machine (RCM) ignition delay data from Dames et al. [40] covering a comprehensive blend spectrum ranging from 100% LPG to 100% DME. This comparison serves as a foundational validation point, ensuring the mechanisms can resolve the varying reactivity levels across the full range of blend ratios before their implementation in both 1D flame speed and 3D engine simulations. Figure 6.7 examines the ignition delays for 100% LPG, comparing experimental data against results calculated in both Chemkin and CONVERGE for the UCSD, RC3, USC, USC_LLNL, ALPINE-DME 158, and ALPINE_LLNL mechanisms. The RC3 mechanism was used as a comparison tool for validation to see how the newly constructed chemical mechanism performed against known frameworks.

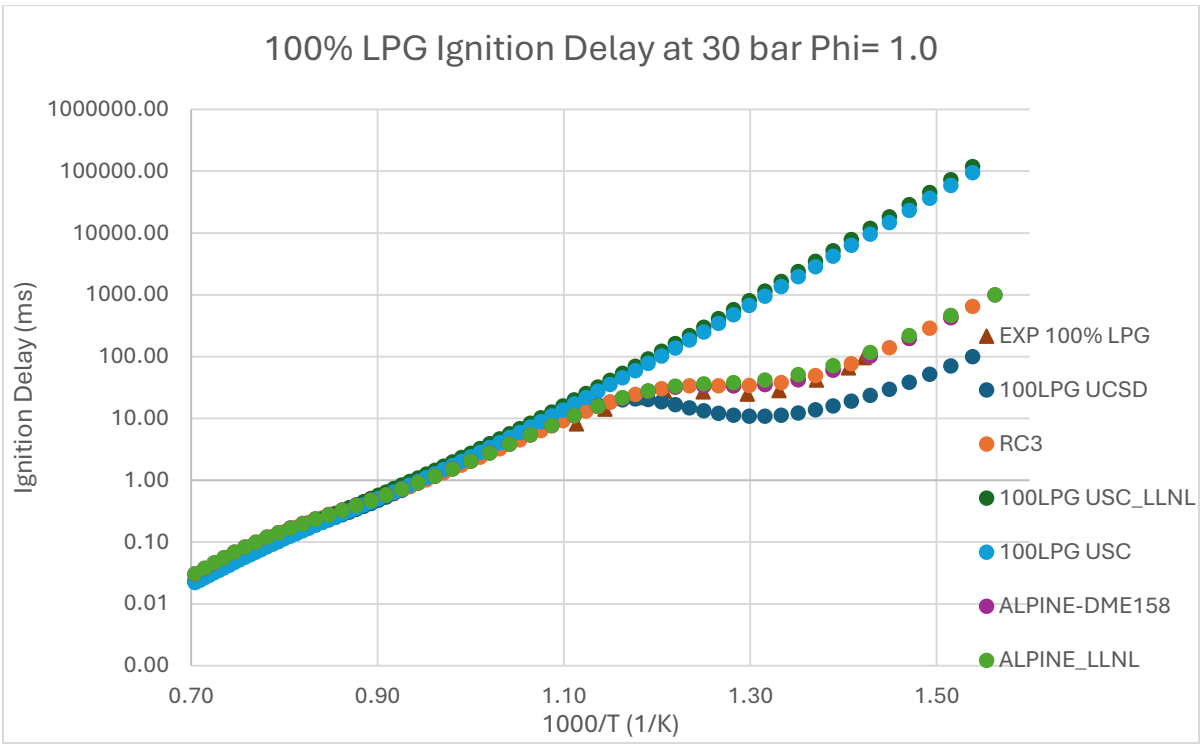

Figure 6.7. 0D Ignition delay simulations with Chemkin and CONVERGE for 100% LPG at the experimental conditions from the work of Dames et al [40].

The ignition delay simulations for the RC3 mechanism were conducted in CONVERGE, utilizing its specialized solver to significantly reduce computational time, while the remaining mechanisms were evaluated using Chemkin. As illustrated in Figure 6.7, both the USC base and blended USC_LLNL mechanisms failed to capture the Negative Temperature Coefficient (NTC) behavior of pure propane. This is a characteristic limitation of the USC mechanism's architecture, as it was primarily tuned using shock tube data at higher temperature ranges where NTC behavior is not present. The base UCSD mechanism predicted a faster ignition delay than observed experimentally, falling outside the bounds of accepted experimental uncertainty. This discrepancy is likely attributable to the size limitations of the UCSD framework; with only 59 species and 271 reactions, it lacks the intermediate chemical pathways necessary to resolve complex autoignition

trends. In contrast, the RC3, ALPINE_LLNL, and ALPINE-DME158 mechanisms all accurately predicted ignition delays that captured the NTC behavior and aligned with the experimental data. The newly developed ALPINE-DME158 demonstrated the highest fidelity, accurately resolving the transition into the NTC zone. Within this validated range, the mechanism demonstrates an average error of only 7.2%, with all calculated values falling within the experimental standard error bounds.

Figure 6.8 presents the ignition delay simulations for 100% DME. As noted by Dames et al. [40], experimental data for this fuel is notably scarce; only four RCM data points were published for the temperature range of 610 K to 655 K. This limited range presents a significant challenge for model validation, as there are no other published RCM experiments for DME at these specific conditions, highlighting a critical gap in the current combustion literature. Despite the limited experimental benchmarks, the simulation results reveal distinct differences in mechanism performance. The USC_LLNL mechanism again fails to capture the fundamental NTC behavior of DME. This suggests that the mechanism tuning cannot resolve the low-temperature radical growth required to predict DME's unique autoignition pathways. While the LLNL base mechanism also struggled to capture this behavior within the USC blend, the ALPINE_LLNL simulations demonstrated a more accurate trend, predicting the expected autoignition behavior with performance similar to the original LLNL base model. The RC3, UCSD, and ALPINE-DME158 mechanisms all successfully captured the qualitative trend of DME ignition. Notably, the ALPINE-DME158 mechanism maintained the strong performance baseline established by the UCSD mechanism while offering superior agreement with the existing experimental data points. While validating the pure fuel endpoints (100% LPG and 100% DME) is a necessary first step, the true capability of a kinetic mechanism lies in its ability to resolve the complex chemical interactions of

blended fuels. To demonstrate this, the following figures examine the ignition delay of 10%, 25%, and 50% DME blends. These simulations will show how the ALPINE-DME158 mechanism captures the non-linear shift in reactivity and NTC behavior as DME begins to dominate the combustion chemistry of the LPG base.

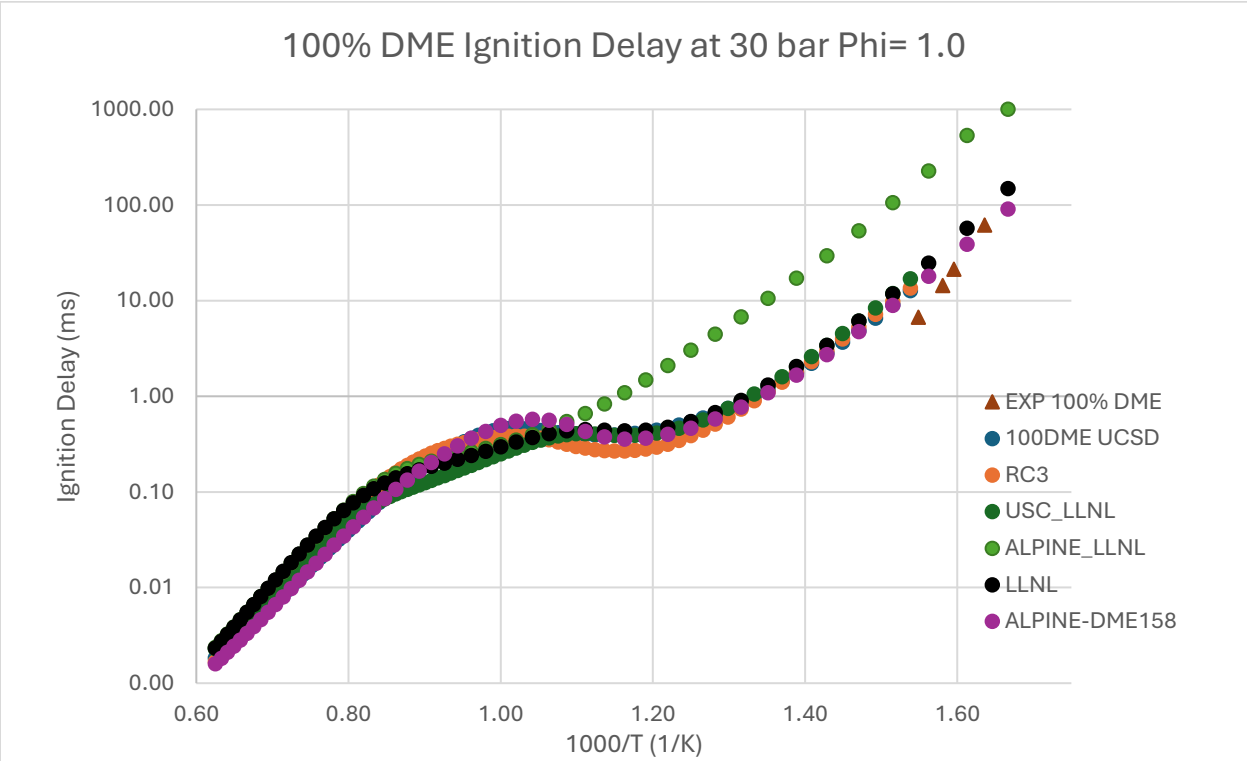

Figure 6.8. 0D Ignition delay simulations with Chemkin and CONVERGE for 100% DME at the experimental conditions from the work of Dames et al [40].

Figure 6.9 displays the simulation results for the 10% DME / 90% LPG blend. The RC3, UCSD, USC_LLNL, and ALPINE-DME158 chemical kinetic mechanisms are compared against the RCM experimental data. The USC_LLNL mechanism continues to fail in capturing the characteristic NTC behavior. Across all tested fuels—100% LPG, 100% DME, and the 10% blend the USC_LLNL results appear as a linear progression, where ignition delay simply decreases with increasing temperature. This indicates a significant failure to resolve the low temperature peroxy

radical chemistry required to predict the kinetic behavior of the NTC region. Furthermore, the UCSD mechanism predicted significantly faster ignition delay times across the entire temperature range, failing to match the experimental trend.

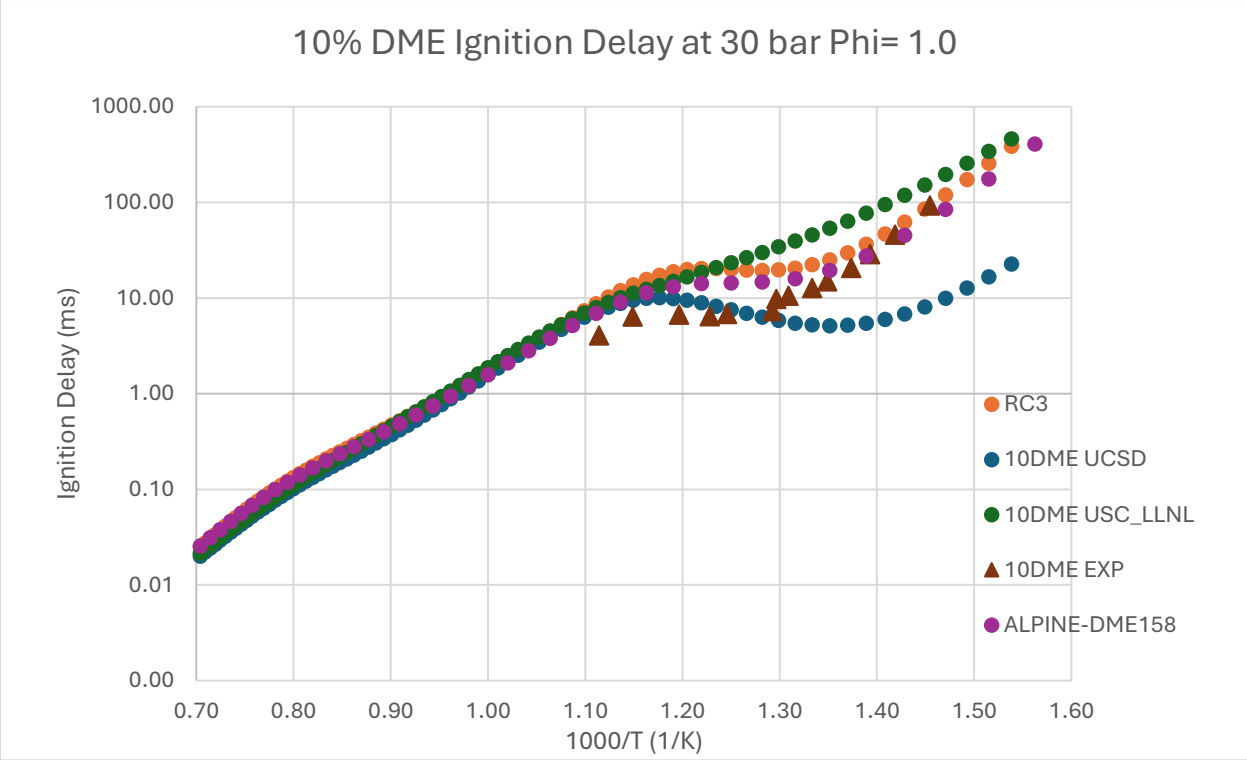

Figure 6.9. 0D Ignition delay simulations with Chemkin and CONVERGE for 10% DME at the experimental conditions from the work of Dames et al [40].

The UCSD model also predicted a lower-temperature shift of the NTC region compared to the experimental measurements, suggesting that its reduced species set cannot properly handle the effects of the propane-DME interaction. In contrast, the RC3 and ALPINE-DME 158 mechanisms both resolved the experimental ignition delay characteristics. The ALPINE-DME 158 followed the experimental trend most closely, matching the experimental uncertainty at lower temperatures before slightly diverging from the experimental measurements near the peak of the NTC region. Despite this slight divergence in the NTC region, the ALPINE-DME 158 mechanism performed

better than all existing chemical mechanisms tested. This superior performance demonstrates that its expanded chemical framework is better optimized for the specific radical pool interactions such as the OH radical branching and RO_2 isomerization present in these LPG/DME blends.

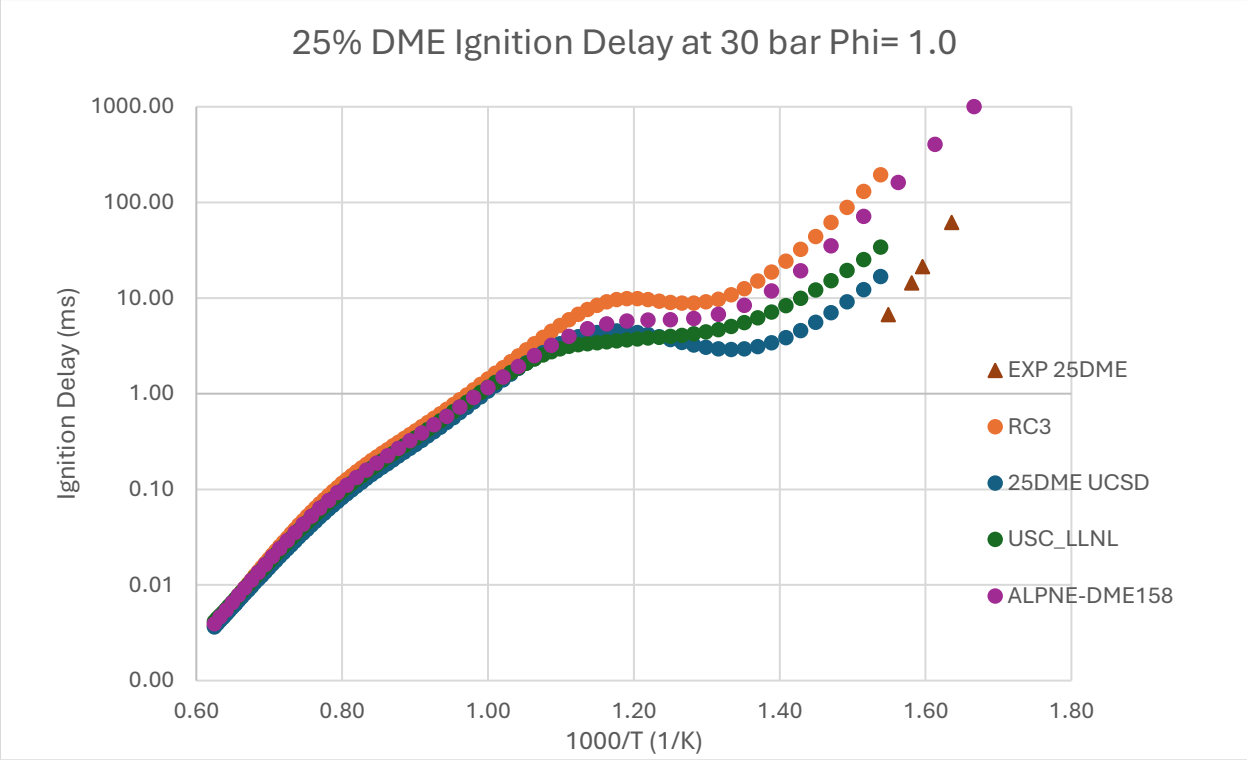

Figure 6.10. 0D Ignition delay simulations with Chemkin and CONVERGE for 25% DME at the experimental conditions from the work of Dames et al [40].

Figure 6.10 illustrates the simulated ignition delay for the 25% DME / 75% LPG fuel blend. Similar to the 100% DME baseline, experimental representation of this specific blend's autoignition properties is severely limited in the current literature. Only four experimental data points are available for comparison, restricted to a narrow low-temperature window between 610 K and 655 K. Interestingly, at this 25% DME blending ratio, the USC_LLNL mechanism demonstrates its first manifestation of NTC behavior, a kinetic feature it failed to capture in the pure LPG, pure DME, and 10% DME cases. When comparing the predicted reactivity across the

evaluated models, the UCSD mechanism calculated the fastest ignition delay times, followed sequentially by USC_LLNL, ALPINE-DME158, and finally the RC3 mechanism. A notable observation from Figure 6.10 is a systematic deviation: none of the evaluated kinetic mechanisms calculate ignition delay values that fall within the reported experimental uncertainty bounds. However, given the extreme paucity of experimental data in this specific low-temperature regime, it remains unclear whether this discrepancy stems from fundamental deficiencies shared across all kinetic models, or if the experimental measurements themselves lack robust validation. Because these specific RCM experiments have not been independently reproduced or verified in subsequent literature, drawing absolute conclusions regarding mechanism fidelity solely from these four isolated points is challenging.

Figure 6.11 exhibits the results for the 50% DME ignition delay 0D simulations. This mixture represents a critical midpoint in the study, where the high-reactivity characteristics of DME and the stability of propane exert equal influence on the radical pool. As with the 100% DME and 25% blend cases, experimental data remains scarce, with only five RCM points available between 655 K and 710 K.

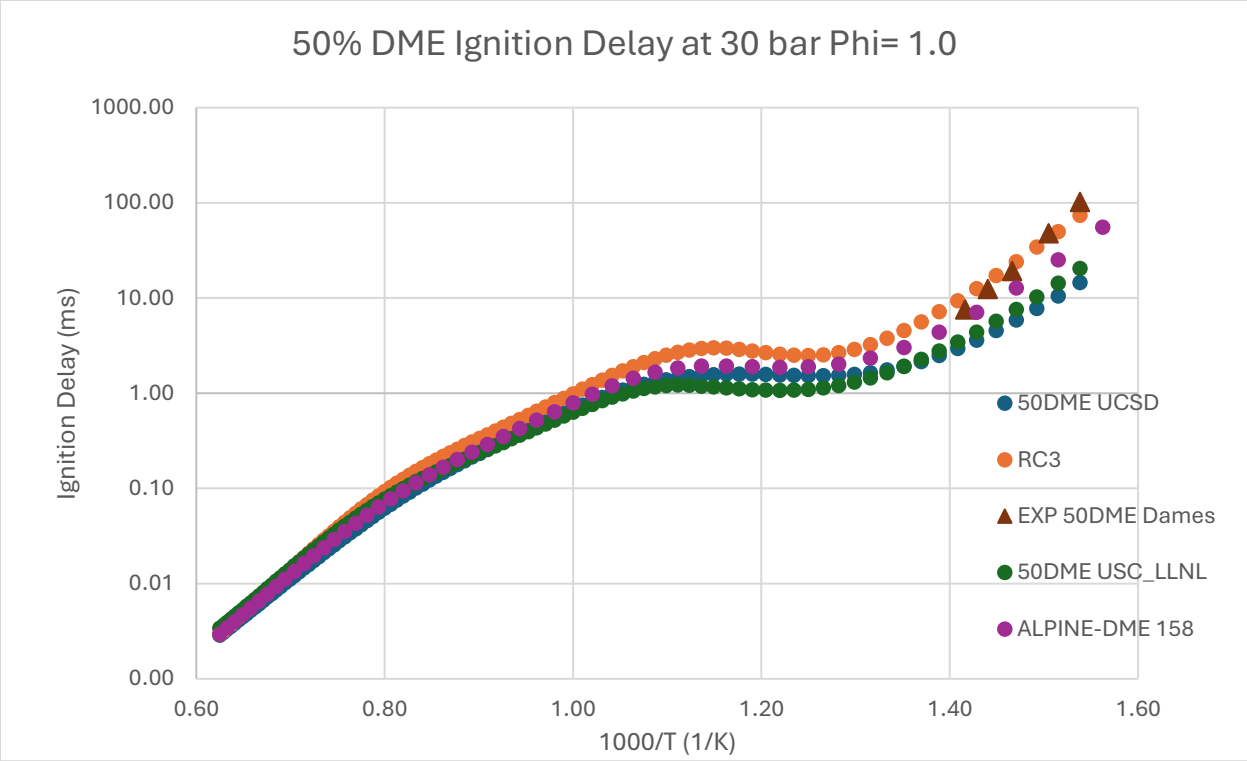

Figure 6.11. 0D Ignition delay simulations with Chemkin and CONVERGE for 50% DME at the experimental conditions from the work of Dames et al [40].

Unlike the 25% blend case where all models showed a systematic deviation, the simulation results for the 50% blend demonstrate a notable convergence toward the experimental data. Both the RC3 and ALPINE-DME 158 mechanisms successfully captured experimental ignition delay times, falling within the reported uncertainty bounds for this narrow temperature range. This alignment is a strong validation of the ALPINE-DME 158's expanded framework, as it successfully resolves the complex cross-reactions between propane and DME radicals at high concentrations. The fact that the ALPINE-DME 158 consistently matches the experimental data at the 0%, 10%, and 50% DME intervals—despite the literature's limited temperature range solidifies its status as the most robust mechanism for predicting the autoignition characteristics of these blends. However, to fully verify the validity of the ALPINE-DME158's capabilities and ensure it

can resolve the complete combustion process, it is necessary to move beyond temporal ignition data. The following section examines 1D laminar flame speed simulations, comparing the mechanism's predicted flame propagation rates against experimental data. This dual-validation approach, encompassing both autoignition timing and flame front reactivity, is essential to confirm that the mechanism is truly optimized for the multi-dimensional environment of a boosted SI LPG/DME engine.

6.2.2 Ignition Delay Sensitivity Analysis

After the ignition delay simulations were completed, to gain further insight into why the UCSD base mechanism predicts faster ignitions for all of the simulations, a sensitivity analysis on the ignition delay was conducted utilizing Chemkin.

To quantify the underlying chemical drivers of the induction period, a species-specific sensitivity analysis was performed examining the how the individual species reaction rates of production and consumption differ between mechanisms. Due to the significant discrepancy in the predicted first-stage ignition temperatures between the mechanisms (950K for UCSD vs. 730K for ALPINE-DME 158), a temperature-based normalization was discarded. Instead, a 0.5% temporal offset from each inflection point was utilized to capture the induction state unique to each mechanism. This approach reveals how the differing thermal foundations predicted in the first stage directly influence the radical pool available for the main ignition event. To facilitate a direct kinetic comparison, reaction rates for each species were normalized by the maximum absolute rate-of-production (ROP) observed from the highest producing reaction for that specific species across both mechanisms.

While the normalized plots visualize the relative importance of specific chemical pathways, they do not account for the massive disparity in absolute kinetic intensity between the two models. To bridge this gap, a magnitude ratio was calculated for each species, defined as the ratio of the UCSD ROP_max to the ALPINE-DME ROP_max. This ratio serves as a scaling factor that contextualizes the visual data; it reveals that while two mechanisms may appear to share similar primary pathways on a normalized scale, the physical speed and aggressiveness of these pathways can differ by several orders of magnitude. This provides a quantitative explanation for the divergence in predicted ignition delay and temperature gradients.

Table 6.3 Maximum Rate of Production and Magnitude Ratios for 100% LPG at 690K.

100% LPG at 690K			
Species	UCSD Max Rate of Production (mol/cm³·s)	ALPINE-DME 158 Max Rate of Production (mol/cm³·s)	Magnitude Ratio (UCSD ROP/ ALPINE-DME ROP)
OH	-1.33E-02	-5.63E-05	237
HO2	-1.04E-02	-5.85E-05	178
H2O2	5.21E-03	2.93E-05	178
H	-4.29E-04	-7.70E-06	56
H2	2.01E-05	2.39E-07	84
CH3	1.33E-04	-2.69E-05	5
C3H8	-1.33E-02	-5.63E-05	237
CH2O	1.09E-02	2.72E-05	400
CO	9.25E-03	3.03E-05	306

The most significant kinetic disparities are observed in the carbon oxidation pathways and the primary radical pool. Formaldehyde and Carbon Monoxide exhibit magnitude Ratios of 400

and 306, respectively. This indicates that the UCSD mechanism accelerates the transition from intermediate fuel fragments to final oxidation products at nearly 300 to 400 times the rate of the detailed mechanism.

Similarly, the primary chain branching agents, OH and HO2, show ratios of 237 and 178. These values suggest that the radicals driving the ignition in the UCSD model is vastly inflated. This over-pressurization effectively erodes the induction plateau, leading to the near-instantaneous temperature rises observed in the UCSD global simulations. Interestingly, the CH3 radical exhibits a negative ratio (-4.95), indicating a fundamental difference in the direction of net methyl flux between the two mechanisms at this specific induction point as the ALPINE-DME 158 mechanism is calculating consumption of CH3 while UCSD differs and calculates that CH3 is being produced

The normalized reaction pathways for the primary radical pool (Figure 6.12) illustrate a fundamental bypassing of the low-temperature chain in the UCSD mechanism compared to the multi-stage progression of the ALPINE-DME 158 model. In the ALPINE-DME mechanism, OH production is dominated by the decomposition of complex keto-hydroperoxides, such as C3KET13, which represents the physical induction where the fuel must undergo several stages of structural rearrangement before branching occurs. Conversely, the UCSD mechanism bypasses these intermediate species by favoring direct OH attack on the propane backbone (C3H8 + OH) and simpler fragments like CH2O. This directness allows the UCSD model to transition almost immediately into a high-energy state once a thermal threshold is met.

The absolute physical impact of these differences is quantified by the magnitude ratios established in Table 6.3. While both mechanisms identify the 2HO2<=>H2O2+O2 recombination as a primary sink for hydroperoxyl radicals, the 178x higher intensity in the UCSD model reveals

a vast over calculation of the radical pool. This extreme kinetic aggression means that the peroxide burns hundreds of times more violently in the global model than in the detailed mechanism.

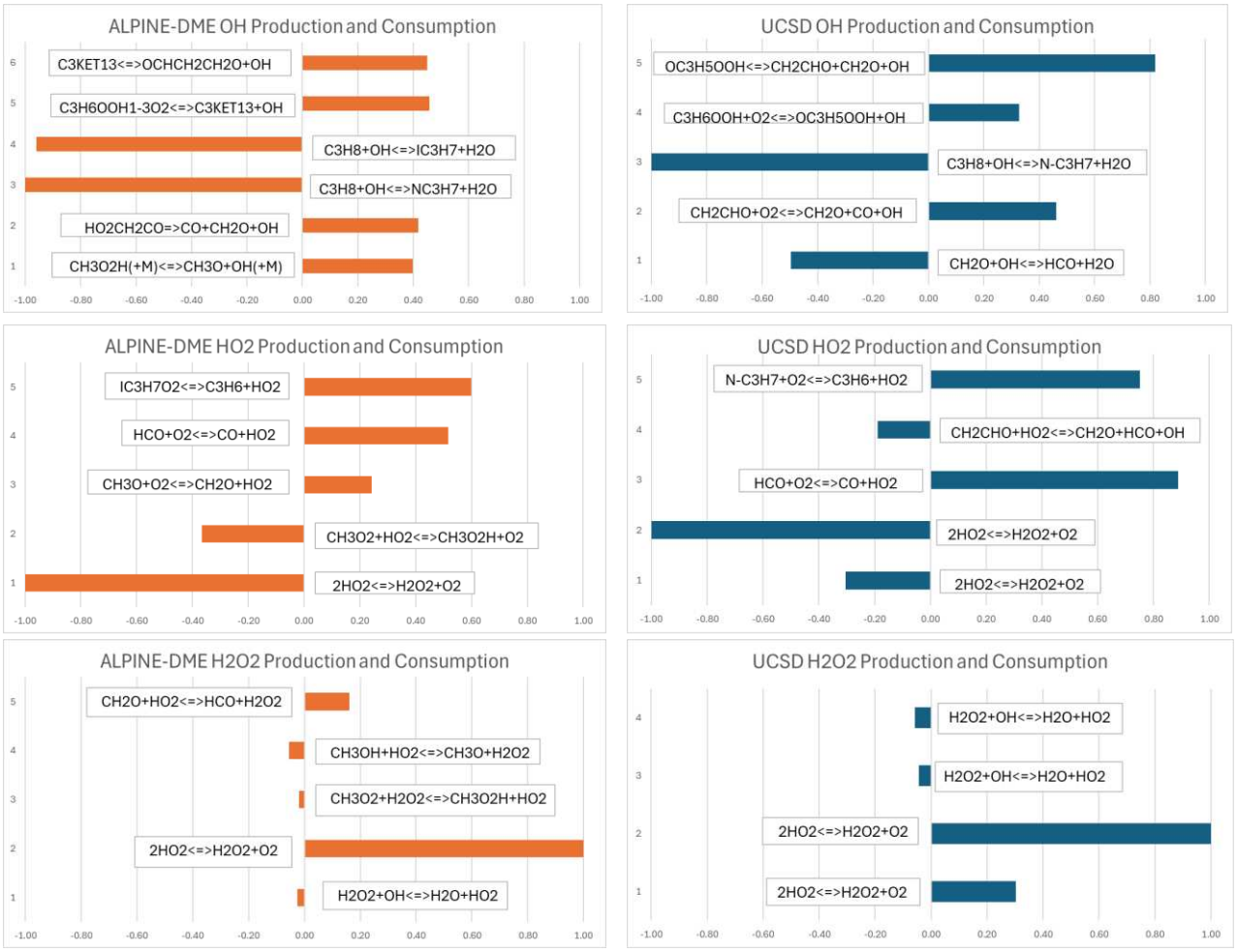

Figure 6.12 Ignition delay species sensitivity analysis normalized ROP for OH, HO2, and H2O2 at 0.5% induction offset for 100% Propane at 690K and 30 bar between two chemical kinetic mechanisms UCSD and ALPINE-DME 158.

The normalized reaction pathways for the smaller fragments seen in Figure 6.13 (H, H2, and CH3) reveal a shift from the complex radical-branching control seen in the primary pool toward a more generalized small-molecule breakdown. For atomic hydrogen (H) and H2, both mechanisms qualitatively agree on the dominance of the H+O2(+M)<=>HO2(+M) sink and fuel abstraction steps, yet the 55x and 84x magnitude ratios confirm that these steps are still occurring at an unphysically accelerated pace in the UCSD model. The most significant topological

divergence appears in the CH3 methyl radical; while ALPINE-DME 158 exhibits a controlled production through large-molecule fragmentation (e.g., IC3H7O), the UCSD mechanism shows a much more aggressive oxidation cycle through formaldehyde and HO2 reactions.

Figure 6.13 Ignition delay species sensitivity analysis normalized ROP for H, H2, and CH3 at 0.5% induction offset for 100% Propane at 690K and 30 bar between two chemical kinetic mechanisms UCSD and ALPINE-DME 158.

Figure 6.14 indicates that for propane consumption, both mechanisms rely heavily on OH attack, yet the UCSD model couples this directly to an inflated radical pool, resulting in a consumption rate 236x higher than the detailed mechanism. This accelerated breakdown feeds

directly into the formaldehyde CH2O) and carbon monoxide (CO) pathways, which exhibit the highest magnitude ratios of the entire set at 400x and 306x, respectively. The UCSD mechanism simplifies the transition from intermediate fragments to final products through their global reaction approach, whereas the ALPINE-DME 158 mechanism demonstrates a more regulated carbon flux distributed across several complex oxygenated intermediates like HO2CH2CO. This structural simplification in the global model creates a kinetic accumulation that, once breached, releases the chemical energy of the fuel charge almost instantaneously.

Figure 6.14 Ignition delay species sensitivity analysis normalized ROP for C3H8, CH2O, and CO at 0.5% induction offset for 100% Propane at 690K and 30 bar between two chemical kinetic mechanisms UCSD and ALPINE-DME 158.

The addition of 25% DME to the fuel blend significantly alters the kinetic disparity between the UCSD and ALPINE-DME 158 mechanisms. A comparison of the magnitude ratios in Table 6.4 against the previous 100% LPG case reveals a profound shift toward kinetic alignment indicating that the presence of an oxygenated accelerant partially masks the globalized model's structural simplifications. However, a persistent kinetic over-prediction remains across nearly all species. At higher concentrations of DME, this leads to vastly divergent chemical performance as the increased reactivity of the overall mixture amplifies the UCSD mechanism's underlying instability.

Table 6.4 Maximum Rate of Production and Magnitude Ratios for 25% DME at 690K.

25% DME at 690K			
Species	UCSD Max Rate of Production (mol/cm³·s)	ALPINE-DME 158 Max Rate of Production (mol/cm³·s)	Magnitude Ratio (UCSD ROP/ ALPINE-DME ROP)
OH	2.36E-02	3.49E-03	6.75
HO2	1.44E-02	3.86E-03	3.72
H2O2	-1.18E-02	-1.75E-03	6.75
H	1.15E-03	1.20E-03	0.95
H2	2.83E-04	1.75E-04	1.62
CH3	2.86E-03	7.26E-03	0.39
C3H8	-7.85E-03	-1.54E-03	5.09
CH2O	-1.13E-02	-1.74E-03	6.49
CO	1.44E-02	3.86E-03	3.72
CO2	2.80E-04	1.27E-04	2.20
CH3OCH3	-2.94E-03	-9.47E-04	3.10
CH3OCH2	3.60E-03	1.08E-03	3.34
CH3OCH2O2	-3.60E-03	-1.08E-03	3.34
CH2OCH2O2H	8.23E-04	6.48E-04	1.27
HO2CH2OCHO	-4.30E-05	-6.97E-05	0.62

The addition of 25% DME initiates better species convergence in the primary radical pool, as evidenced by the OH and H2O2 magnitude ratios falling from triple digits in the pure LPG case to 6.75 and 3.72, respectively. Figure 6.15 illustrates that with the oxygenated accelerant present, the reaction pathways for both mechanisms show significantly more alignment than the 100% LPG case. Notably, both models now identify the H2O2(+M)<=>2OH(+M) peroxide dissociation as a dominant production pathway for OH. This shift indicates that the DME oxidation chain effectively forces the global UCSD mechanism to operate within a physical regime that more closely follows the multi-stage induction process of the detailed ALPINE-DME 158 kinetics. However, even with this relative convergence in the reaction pathways, the persistent 3x to 7x over-prediction of absolute radical flux remains a critical differentiator between the two models. While the HO2 and H2O2 plots show qualitative agreement in the dominance of recombination and dissociation steps, the UCSD mechanism still maintains a higher kinetic intensity. This remaining disparity suggests that the globalized model still lacks the full suite of intermediate species to slow down combustion present in the detailed mechanism, which likely contributes to the accelerated ignition timings observed in the 1D simulations even when the primary pathways appear synchronized.

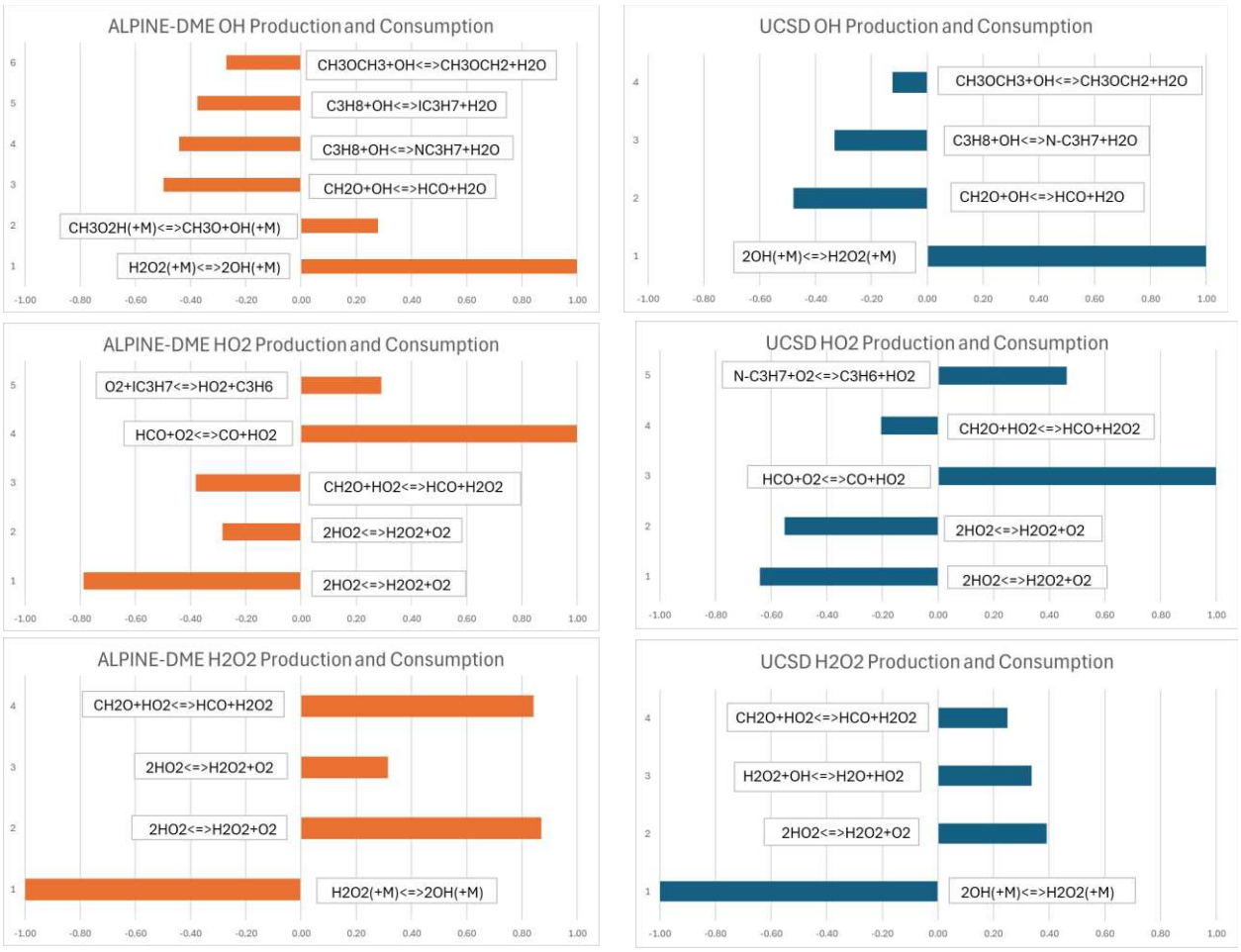

Figure 6.15 Ignition delay species sensitivity analysis normalized ROP for OH, HO2, and H2O2 at 0.5% induction offset for 75% Propane and 25% DME at 690K and 30 bar between two chemical kinetic mechanisms UCSD and ALPINE-DME 158.

As shown in Figure 6.16, the magnitude ratios for atomic and molecular hydrogen into near parity, with H and H2 dropping to 0.95 and 1.62, respectively. This alignment is reflected in the reaction pathways, where both mechanisms consistently identify H+O2(+M)<=>HO2(+M) as the primary sink for atomic hydrogen. However, the CH3 radical remains a significant outlier with a magnitude ratio of 0.39. While the ALPINE-DME 158 mechanism shows methyl production primarily through the abstraction and addition cycles of C2 species, the UCSD mechanism relies heavily on the direct decomposition of ether-specific fragments like CH3OCH2. This confirms that even when the gross kinetic intensity appears synchronized, the globalized model still

bypasses the multi-stage carbon-chain chemistry that regulates methyl flux in the detailed mechanism.

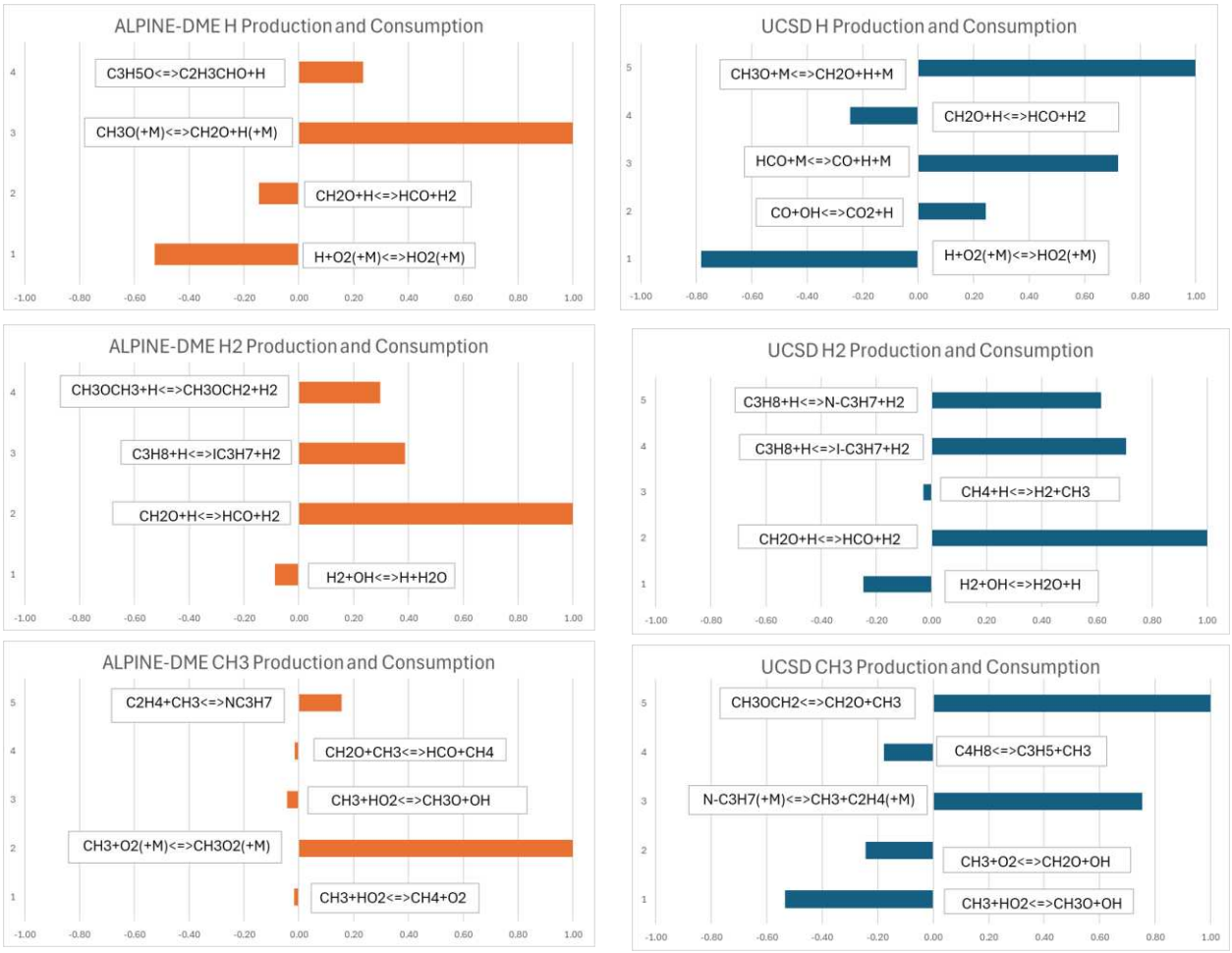

Figure 6.16 Ignition delay species sensitivity analysis normalized ROP for H, H, and CH3 at 0.5% induction offset for 75% Propane and 25% DME at 690K and 30 bar between two chemical kinetic mechanisms UCSD and ALPINE-DME 158.

The final stage of the 25% DME kinetic analysis focuses on the transition from primary fuel species to intermediate fragments. As shown in Figure 6.17, the consumption of propane and DME exhibits strong stoichiometric agreement between mechanisms, with both models identifying OH abstraction as the primary driver for fuel breakdown. The magnitude ratios of 2.33 for C3H8 and 1.27 for CH3OCH3 confirm that the global UCSD mechanism is well-aligned with the detailed kinetics regarding the gross rate of fuel consumption.

Figure 6.17 Ignition delay species sensitivity analysis normalized ROP for C3H8, CH2O, and CH3OCH3 at 0.5% induction offset for 75% Propane and 25% DME at 690K and 30 bar between two chemical kinetic mechanisms UCSD and ALPINE-DME 158.

Furthermore, the formaldehyde pathways continue to highlight the structural differences in how the mechanisms handle intermediate accumulation. While the reaction pathways in Figure 6.17 appear synchronized emphasizing OH and HO2 attack, the persistent magnitude ratio of 4.64 for CH2O indicates that the UCSD model still processes these fragments nearly five times faster than the detailed ALPINE-DME 158 mechanism. This suggests that while the addition of DME helps the global model calculate a more accurate induction timeline, the UCSD mechanism still maintains an unphysically high throughput for carbon oxidation. This accelerated fragment

processing remains a key differentiator in how each model predicts the final transition from the induction period to the main ignition event.

The reaction pathways for the specialized DME intermediates including the methoxymethyl and CH3OCH2O2 radicals demonstrate the highest degree of kinetic synchronization between the two models. As shown in Figure 6.18, both the UCSD and ALPINE-DME 158 mechanisms are in nearly perfect agreement regarding the primary oxidation sequence: O2 addition to the methoxymethyl radical followed by isomerization to the hydroperoxymethyl species. The magnitude ratios for these steps, as established in Table 6.4, hover between 1.14 and 1.25, confirming that the global model's representation of the early cool flame chemistry is physically grounded when an oxygenated trigger is present.

However, a subtle but critical divergence occurs at the terminal stage of the low temperature chemistry chain. For the keto-hydroperoxide species (HO2CH2OCHO), the magnitude ratio drops to 0.62, indicating that the detailed ALPINE-DME 158 mechanism predicts a higher rate of production for these branching agents than the global model. This suggests that the UCSD mechanism, while generally more aggressive in high-temperature oxidation, may under-predict the complexity and intensity of the specific chemical species that regulate the end of the induction period. This finding underscores that even when magnitude ratios approach unity, the structural differences in how each mechanism terminates the low-temperature chain can still lead to the varying ignition sensitivities observed in the 1D and experimental data.

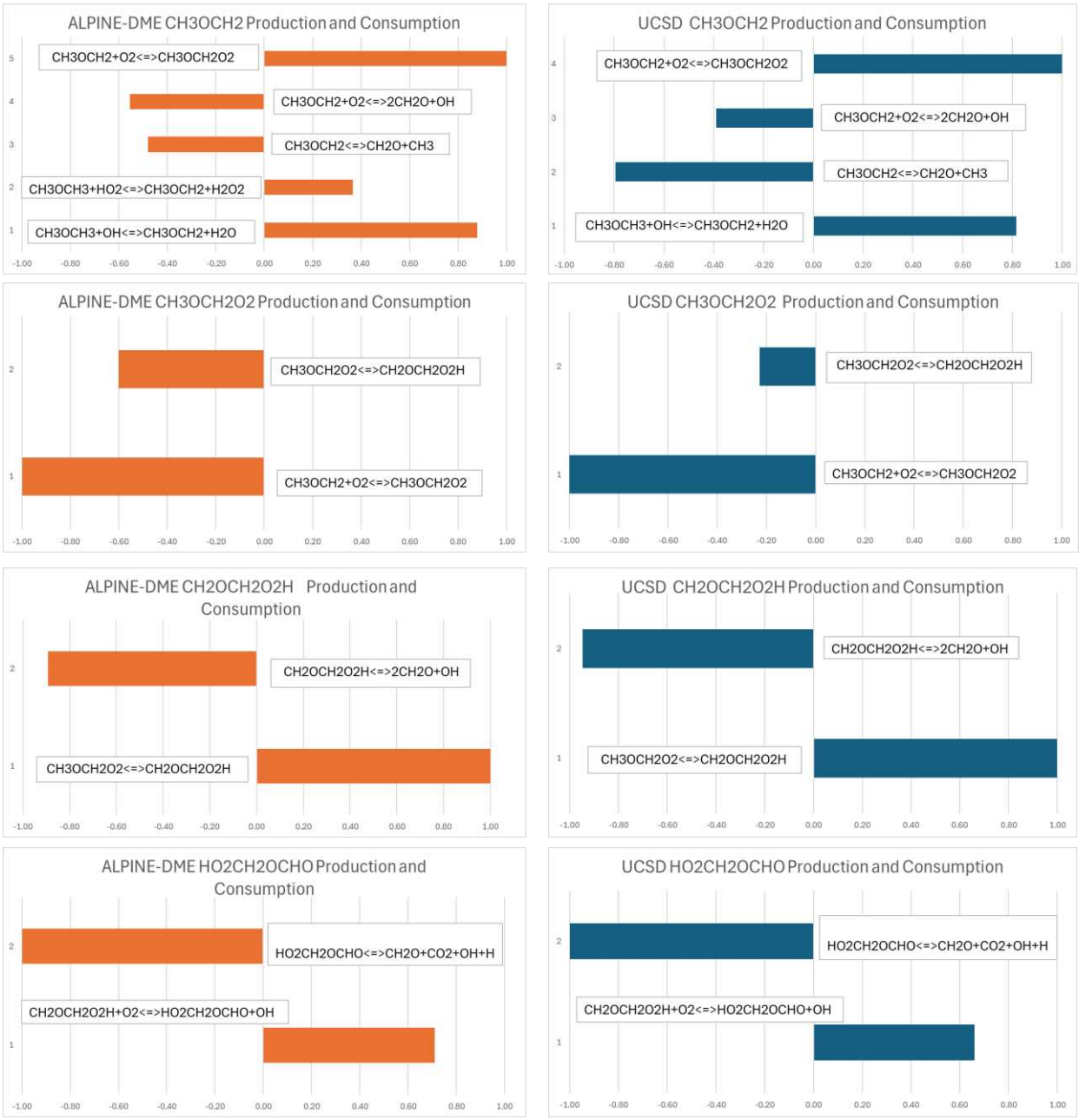

Figure 6.18 Ignition delay species sensitivity analysis normalized ROP for CH3OCH2, CH3OCH2O2, CH2OCH2O2H, and HO2CH2OCHO at 0.5% induction offset for 75% Propane and 25% DME at 690K and 30 bar between two chemical kinetic mechanisms UCSD and ALPINE-DME 158.

The comparative sensitivity analysis between the UCSD and ALPINE-DME 158 mechanisms reveals that the systemic over-prediction of ignition timing in the global model is a direct result of its simplified reaction architecture. In the 100% LPG case, the UCSD mechanism

lacks the intermediate species and multi-stage carbon oxidation pathways that are radical dispersion reactions that are contained in the detailed ALPINE-DME 158 model. By bypassing these intermediate stages, the global model allows for an unregulated acceleration of radical flux, with species-specific rates of production exceeding those of the detailed mechanism by over two orders of magnitude. This results in an unphysical accumulation of the radical pool (OH, HO2) that erodes the induction plateau and leads to the near-instantaneous temperature rise observed in the 1D simulations.

The addition of 25% DME significantly alters this behavior by introducing a dominant low-temperature combustion chain that forces a degree of synchronization between the two models. This leads to a marked convergence in the rates of production for primary ether fragments, with a few magnitude ratios approaching unity. Even with the primary pathways for fuel breakdown aligned, a persistent 3x to 7x over-prediction of the absolute radical flux remains in the UCSD model. This indicates that while the oxygenated trigger can align the initial timing of fuel decomposition, the globalized model still fails to provide the necessary kinetic regulation to capture the smooth transition to main ignition. These fundamental differences in how each mechanism handles radical accumulation and carbon oxidation provide the chemical basis for the disparities seen in ignition delay and temperature gradients. To investigate how this accelerated chemistry influences the physical movement of the flame through the combustion chamber, the following section examines the laminar flame speed characteristics of these fuel blends.

6.2.3 Flame Speed 1D Simulations

To complement the autoignition validation, this section continues the validation effort of the created the ALPINE-DME 158 mechanism, where the mechanism is evaluated for its ability to predict laminar flame speeds. This parameter is critical for engine simulations as it directly influences the rate of heat release and the propagation of the flame front across the combustion chamber. An equivalence ratio sweep from phi 0.75 to 1.6 was conducted across five LPG/DME blend ratios: 100% LPG, 25% DME, 50% DME, 75% DME, and 100% DME. The experimental work of Vasu et al. [71] serves as the foundation for this validation, as it provides consistent datasets for both the pure constituents and each blended condition. For this 1D study, all simulations were performed in Chemkin. To demonstrate the evolution of the mechanism, the newly created blended mechanisms are compared against their respective base models for pure constituents. For the blended fuel cases, the ALPINE-DME 158 is benchmarked against the UCSD and USC_LLNL mechanisms to highlight improvements in predicting mixed-fuel reactivity. Figure 6.19 displays the laminar flame speed for pure propane at varying equivalence ratios. The simulation results from ALPINE-DME 158 are compared against its base UCSD mechanism, while the USC_LLNL is compared against its base USC mechanism.

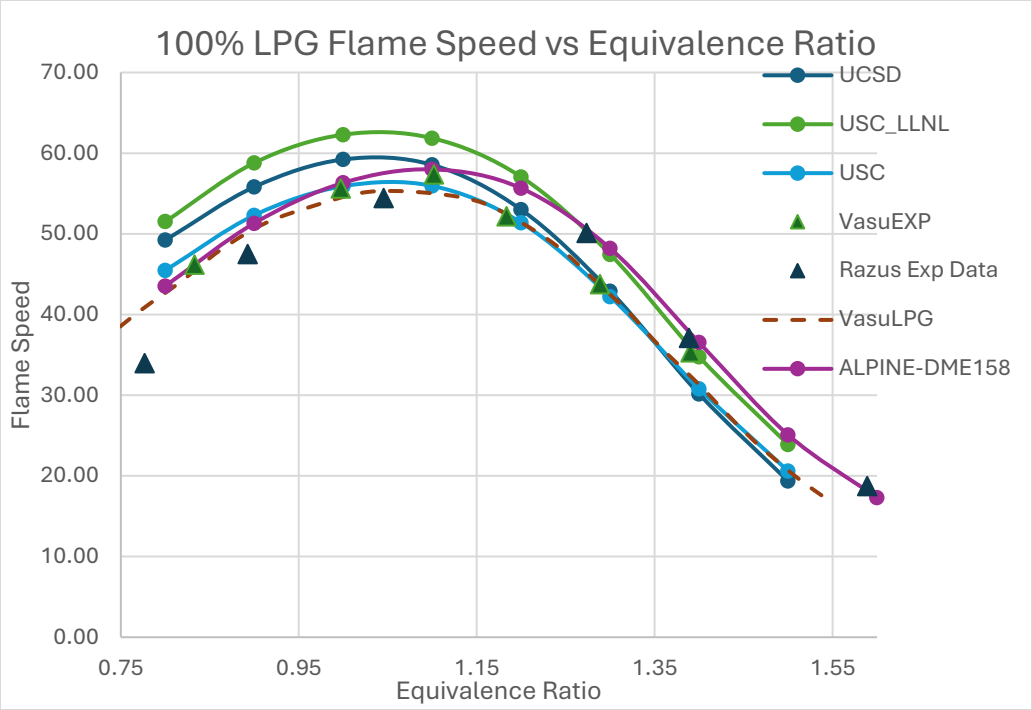

Figure 6.19. 1-D Chemkin flame speed simulations for the various chemical kinetic mechanisms compared to 100% LPG experimental data.

Vasu et al. [71] conducted independent measurements while also incorporating legacy experimental data from Razus to provide a comprehensive baseline. The results for pure propane, as shown in Figure 6.19, indicate that across the entire equivalence ratio sweep, the ALPINE-DME158 mechanism predicts laminar flame speeds that fall within the 5% error bounds of the experimental data. Notably, the newly developed mechanism outperforms its base UCSD framework, as well as the USC and USC_LLNL mechanisms. Furthermore, the ALPINE-DME 158 demonstrates superior predictive accuracy compared to the Aramco 3.0 mechanism, which was the primary benchmark utilized by Vasu et al. in their original study. This high degree of accuracy for the pure LPG constituent ensures that the underlying C3 chemistry foundation is robust before evaluating the added complexity of DME blending. The laminar flame speed results for the 25% DME / 75% LPG blend are presented in Figure 6.20. This blend ratio represents the

first introduction of DME's high-reactivity oxygenated species into the propane base. A detailed examination of the mechanism performance reveals a consistent trend of over-predicting the mixture reactivity across several models. Both the USC_LLNL and UCSD mechanisms fail to capture the experimental flame speeds under lean conditions (phi < 1.0), predicting flame speeds significantly faster than those measured experimentally. As the mixture moves toward stoichiometry, the UCSD mechanism begins to converge toward the experimental data, showing improved agreement just before the peak flame speed at phi = 1.1. However, the USC_LLNL mechanism remains excessively reactive through the peak, only aligning with the experimental values in the highly rich regime at phi = 1.3 and above. Throughout this entire sweep, the ALPINE-DME 158 mechanism consistently outperforms the alternative models. The only deviation from the 5% error of the experimental data is seen at excessively rich conditions of phi=1.5 where the model overpredicts flame speed as the experiments define a vast decrease at this equivalence ratio. By effectively moderating the radical pool interactions, it avoids the over-prediction of flame speeds seen in the other mechanisms, maintaining high fidelity in the lean and stoichiometric regions. This accuracy is essential for 3D engine simulations, as over-predicting the flame speed would lead to an artificially high rate of pressure rise and incorrect heat release timing.

Figure 6.21 highlights the results for the Chemkin flame speed simulations for the 50% DME blend. The ALPINE-DME 158 mechanism demonstrates exceptional predictive fidelity in this case, remaining within the 5% error margin of the experimental data across the entire equivalence ratio sweep. In contrast, the alternative mechanisms exhibit inconsistent trends. The UCSD mechanism over-predicts the flame speed in the lean regime before converging with experimental data at phi = 1.10; however, it immediately begins to under-predict flame speeds as the mixture becomes richer.

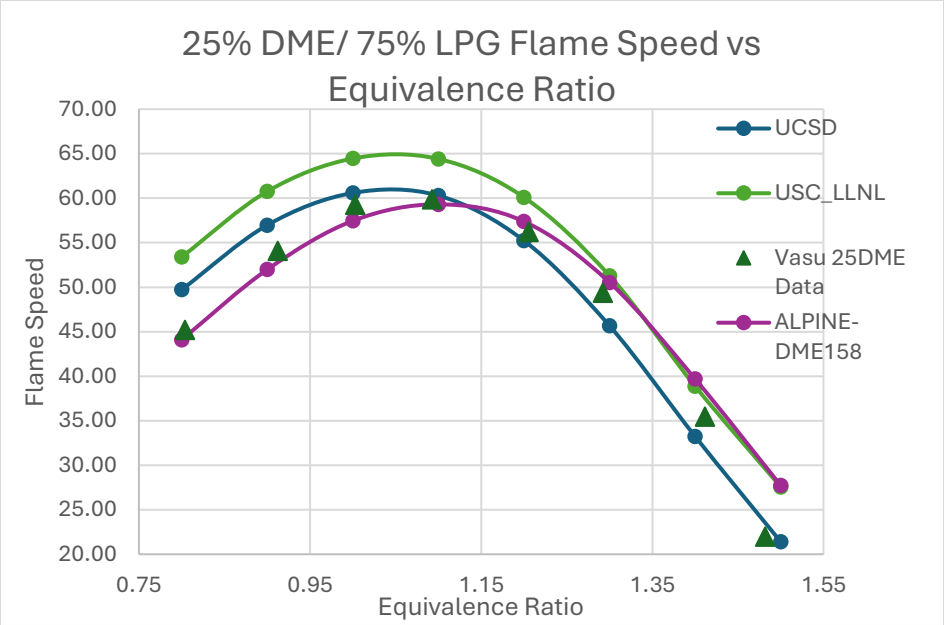

Figure 6.20. 1-D Chemkin flame speed simulations for the various chemical kinetic mechanisms compared to 25% DME experimental data.

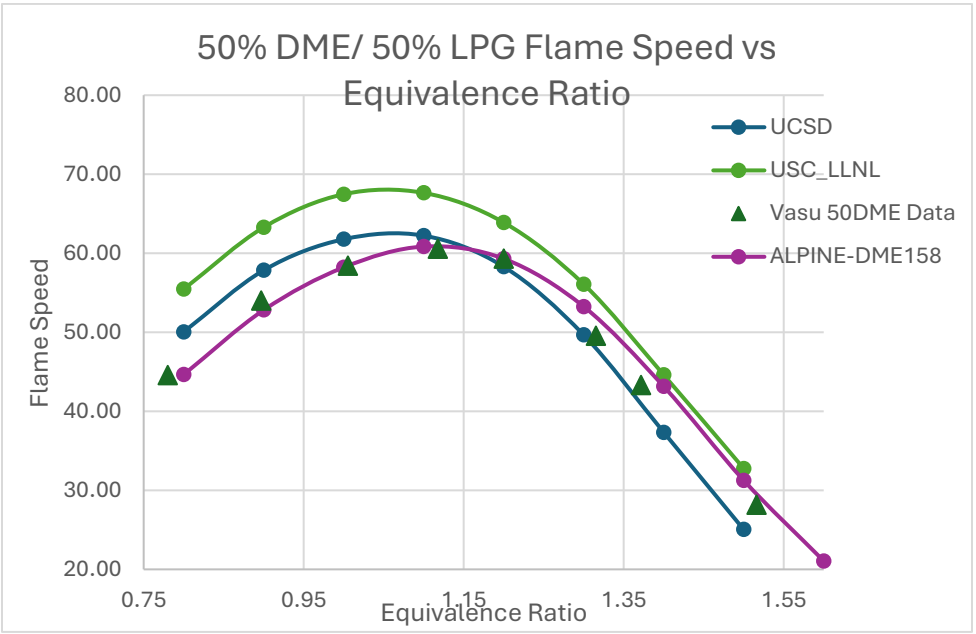

Figure 6.21. 1-D Chemkin flame speed simulations for the various chemical kinetic mechanisms compared to 50% DME experimental data.

The USC_LLNL mechanism maintains a consistent trend of over-prediction through the majority of the sweep. It only enters the 5% experimental error margin at the highly rich condition of phi = 1.35, though it continues to sit at the upper limit of the uncertainty bounds. These results suggest that while the legacy mechanisms can be tuned to match specific points, the ALPINE-DME 158 is the only model capable of resolving the full range of chemical kinetics for this complex blend without requiring localized adjustments.

The results for the 75% DME / 25% LPG simulation run are exhibited in Figure 6.22. At this high concentration of DME, the mixture reactivity is significantly elevated, and the ALPINE-DME 158 mechanism continues to demonstrate superior predictive capability compared to both the base UCSD and USC_LLNL chemical mechanisms. The ALPINE-DME158 initially matches the experimental flame speeds with high precision under very lean conditions.

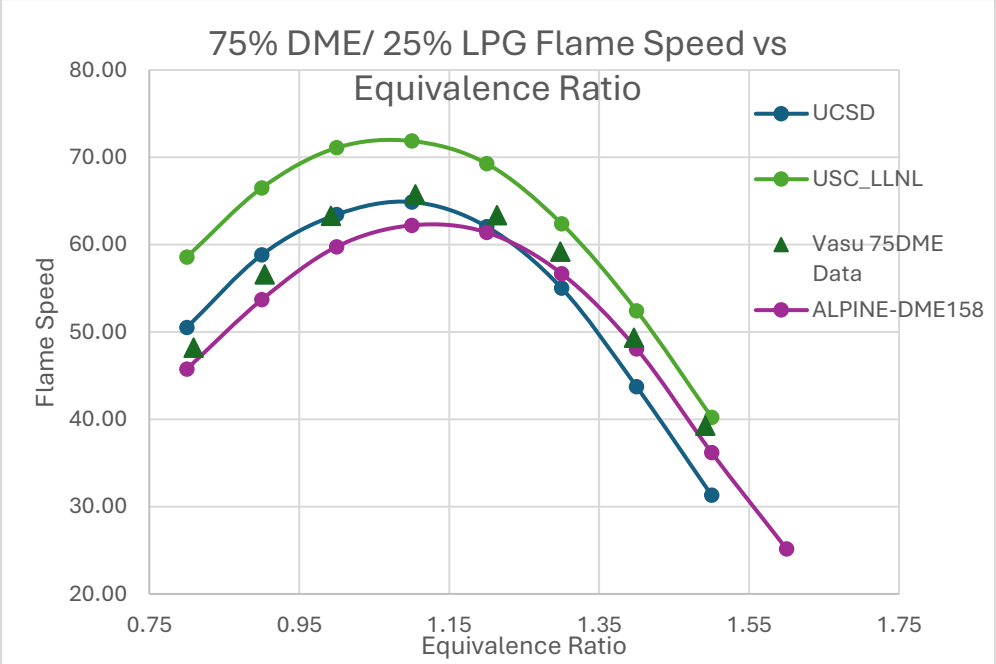

Figure 6.22. 1-D Chemkin flame speed simulations for the various chemical kinetic mechanisms compared to 75% DME experimental data.

However, as the equivalence ratio progresses toward stoichiometric, the mechanism begins to slightly under-predict the flame speeds, falling into the lower bounds of the 5% experimental error margin. In comparison, the UCSD mechanism follows a distinct trend: it over-predicts flame speeds in the lean regime but converges exactly with the experimental values at stoichiometry. However, once it passes the observed peak flame speed and enters rich conditions, the mechanism immediately begins to under-predict the flame speed, falling toward the lower limits of the 5% error. This inconsistent behavior suggests that the UCSD mechanism has an exaggerated sensitivity to the thermal effects associated with equivalence ratio changes. Finally, the USC_LLNL mechanism maintains its previous trend of consistent over-prediction across the entire sweep. Its predicted flame speeds only enter the upper limits of the 5% error margin at highly rich conditions (phi > 1.3). These results further reinforce that while legacy mechanisms may cross the experimental data at isolated points, only the ALPINE-DME 158 provides a stable and reliable trend across the full range of engine-relevant conditions.

The 100% DME simulations, presented in Figure 6.23, reveal the performance limits of the evaluated mechanisms under pure oxygenated fuel conditions. For this specific case, the ALPINE-DME 158 mechanism exhibits a consistent under-prediction of the laminar flame speed in the lean and stoichiometric regimes. This is the only simulation case where the newly developed mechanism does not match or exceed the performance of the base UCSD mechanism. This discrepancy indicates that the 5 species and 14 reactions comprising the UCSD DME sub-mechanism do not interact with the broader ALPINE framework with sufficient kinetic sensitivity to resolve the peak propagation rates of pure DME. The ALPINE-DME 158 performance recovers in the rich regime, where it accurately predicts experimental behavior and falls within the 5% error bounds for phi= 1.20. The base UCSD mechanism performs well across the entire sweep,

remaining within the 5% error bounds. Conversely, the USC_LLNL mechanism shows a divided performance: the base version captures lean flame speeds but fails under rich conditions (phi > 1.1), while the blended USC_LLNL consistently over-predicts the flame speed across the entire sweep, never reaching experimental agreement. The experimental data provided by Vasu et al. [71] and Varghese show close agreement, except at the peak flame speed (phi = 1.1), where Varghese reports a higher value of 73.3 cm/s compared to Vasu's 69.5 cm/s.

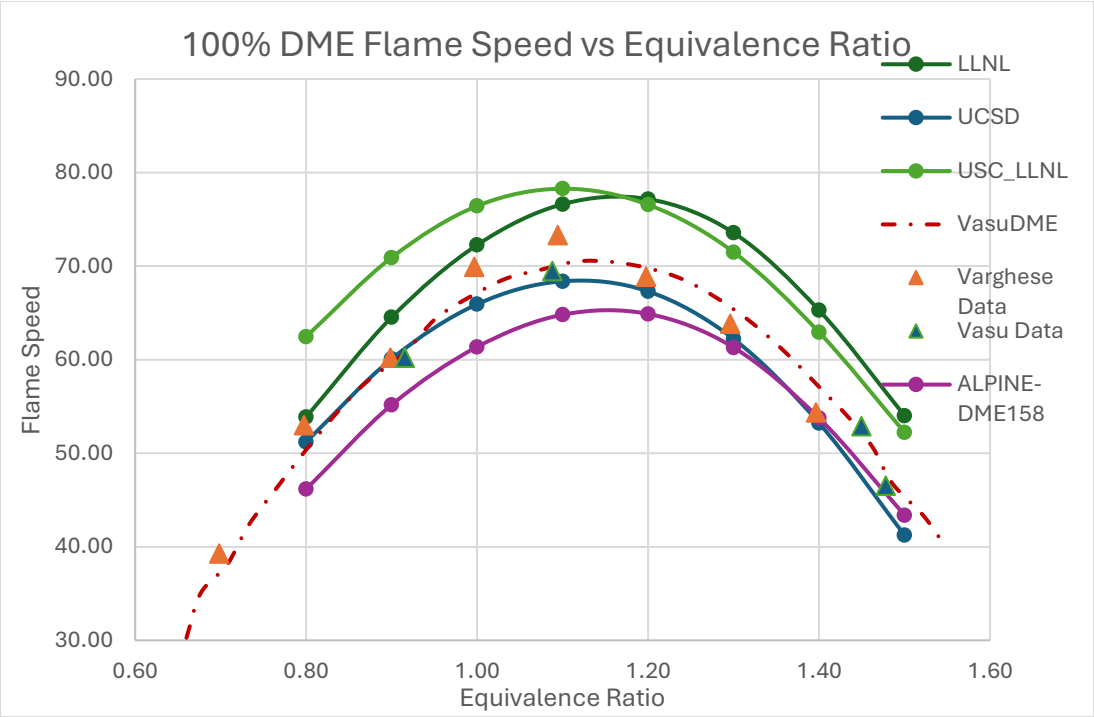

Figure 6.23. 1-D Chemkin flame speed simulations for the various chemical kinetic mechanism compared to 100% DME experimental data.

The ALPINE-DME 158 predicts a peak of 65 cm/s, representing a 7% error relative to Vasu's data. The maximum error occurs at the leanest point (phi = 0.8) at 13%, which steadily decreases as the mixture richens. While the Aramco 3.0 mechanism utilized by Vasu remains the most accurate for the 100% DME case, the ALPINE-DME158 remains the preferred choice for

this study due to its superior performance in the 0% to 75% DME blending range, which constitutes the primary scope of the engine simulations.

The comprehensive validation of the newly developed ALPINE-DME 158 mechanism across both autoignition and laminar flame speed regimes confirms its superior predictive capabilities for LPG/DME blends. By successfully capturing the Negative Temperature Coefficient (NTC) behavior during ignition delay simulations and maintaining a consistent 5% error margin across the majority of laminar flame speed conditions, the mechanism has demonstrated a level of multi-regime accuracy that legacy models such as the UCSD and newly created USC_LLNL could not replicate. While alternative mechanisms exhibited localized accuracy, they often suffered from exaggerated thermal sensitivities or excessive reactivity that would lead to artificial pressure spikes and incorrect knock prediction in a 3D environment. The ALPINE-DME 158, however, maintains a balanced radical pool interaction across the entire 0-75% DME blending range. This dual verification of both temporal and spatial combustion characteristics provides the necessary high-fidelity foundation for the following 3D CFD simulations. In the subsequent chapter, this optimized kinetic framework is deployed within the engine's geometry to analyze the complex interactions of turbulence, spray dynamics, and chemical heat release under boosted SI conditions.

6.3 3D CONVERGE Simulations

With the ALPINE-DME 158 mechanism's chemical fidelity established through 0D autoignition and 1D flame speed validation, the study moves to its primary objective: the simulation of these fuel blends within a multi-dimensional engine environment. While the previous sections confirmed that the mechanism correctly predicts ignition and propagation when the fuel reacts in isolation, the 3D CFD simulations in this section account for the complex interplay of in-

cylinder turbulence, fuel-air mixing, and heat transfer. This transition represents the final step in the validation process, applying the optimized chemical kinetic mechanism to a boosted SI engine geometry to evaluate performance and knock characteristics under real world operating conditions.

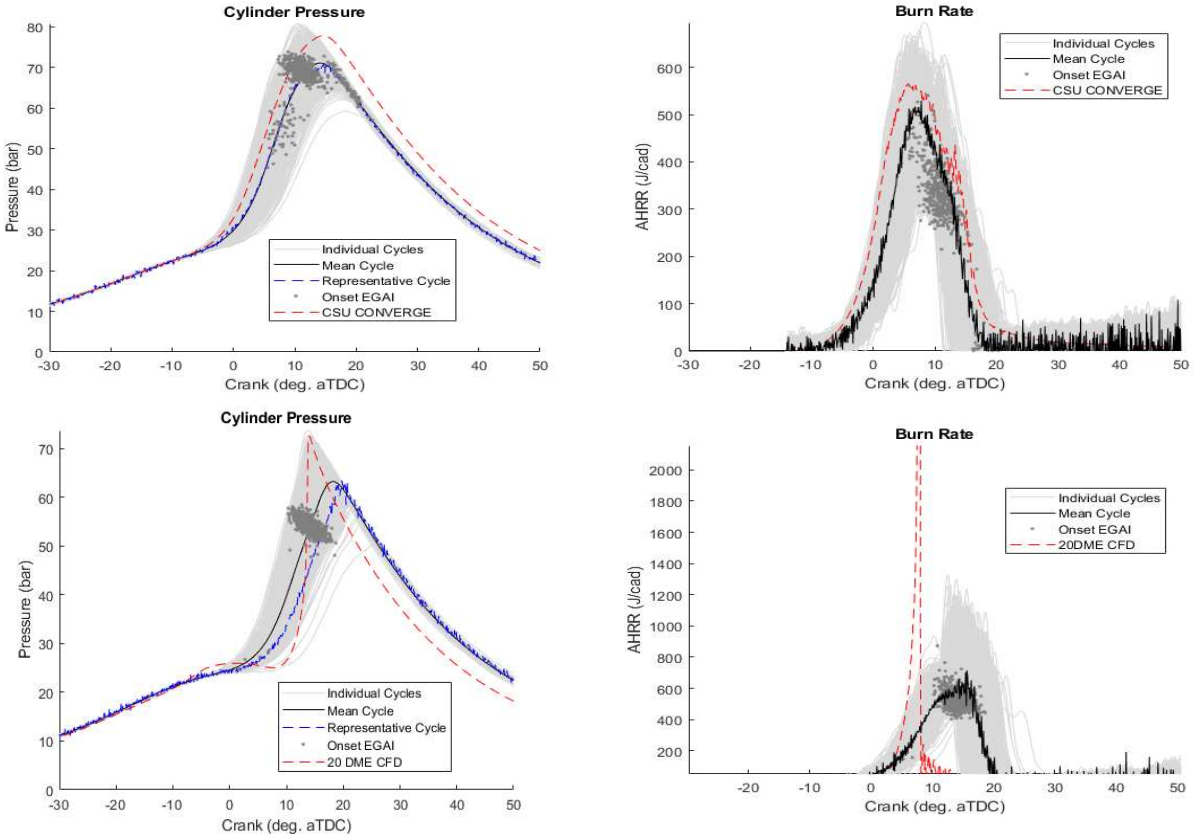

Figure 6.24. USCD mechanism vs Experimental In-cylinder pressure, apparent heat release rate, and knock onset crank angle for 100% LPG and 20% DME

Figure 6.24 shows the initial 3D CONVERGE simulation results for 100% LPG and 20% DME using the UCSD mechanism to create a baseline for comparisons against the new ALPINE-DME 158. The methods for the LPG/DME blend CONVERGE simulations are described in section 2.6. For the 100% LPG case, the UCSD mechanism accurately captured the intake, compression, and exhaust strokes, while the simulated case spark timing was chosen to match the experimental CA50 value near 7.5° aTDC resulting in a CA50 of 6.2 for the UCSD simulations.

However, the in-cylinder pressure was overestimated during the power stroke. This overestimation is likely due to a late heat release, seen in the AHRR plot between 10-20 deg aTDC where the CFD AHRR (shown in red) exhibits an EGAI event that may cause the CONVERGE model to underestimate the true heat transfer which was seen experimentally. Importantly, the UCSD mechanism accurately predicted the KOCA within experimental values. The KOCA for 1000 experimental cycles is displayed on both the pressure trace and the AHRR plot for each test fuel. For the 100% LPG case, the secondary heat release event matches perfectly with the calculated KOCA locations.

The performance of the UCSD mechanism significantly deteriorated when applied to the 20% DME blend. Initial simulations utilized the experimental spark timing, but this resulted in an exponential pressure rise rate, yielding a peak in-cylinder pressure of 95 bar and a peak AHRR exceeding 20,000 J/deg. While the engine does experience increased reactivity with DME, these specific magnitudes are physically unrealistic for this configuration and highlight the failure of the UCSD mechanism to properly resolve the blended fuel chemistry under boosted conditions. Even when the spark timing was retarded past TDC (to 2–4° aTDC) to mitigate this reactivity, the model continued to deviate, failing to capture the experimental compression and expansion curves. With the AHRR still reaching 14,000 J/deg, it is evident that the UCSD mechanism cannot adequately calculate the combustion characteristics of the 20% DME blend, necessitating the transition to the more robust ALPINE-DME 158 framework.

Figure 6.25 presents the 3D CONVERGE simulation results utilizing the newly developed ALPINE-DME 158 mechanism. In stark contrast to the legacy models, the ALPINE-DME 158 demonstrates exceptional agreement with both the experimental pressure traces and the AHRR for both the 100% LPG and 20% DME test cases. This alignment highlights the mechanism's robust

capability to accurately predict the chemical and physical effects of DME addition to LPG across 0D, 1D, and 3D simulation scales.

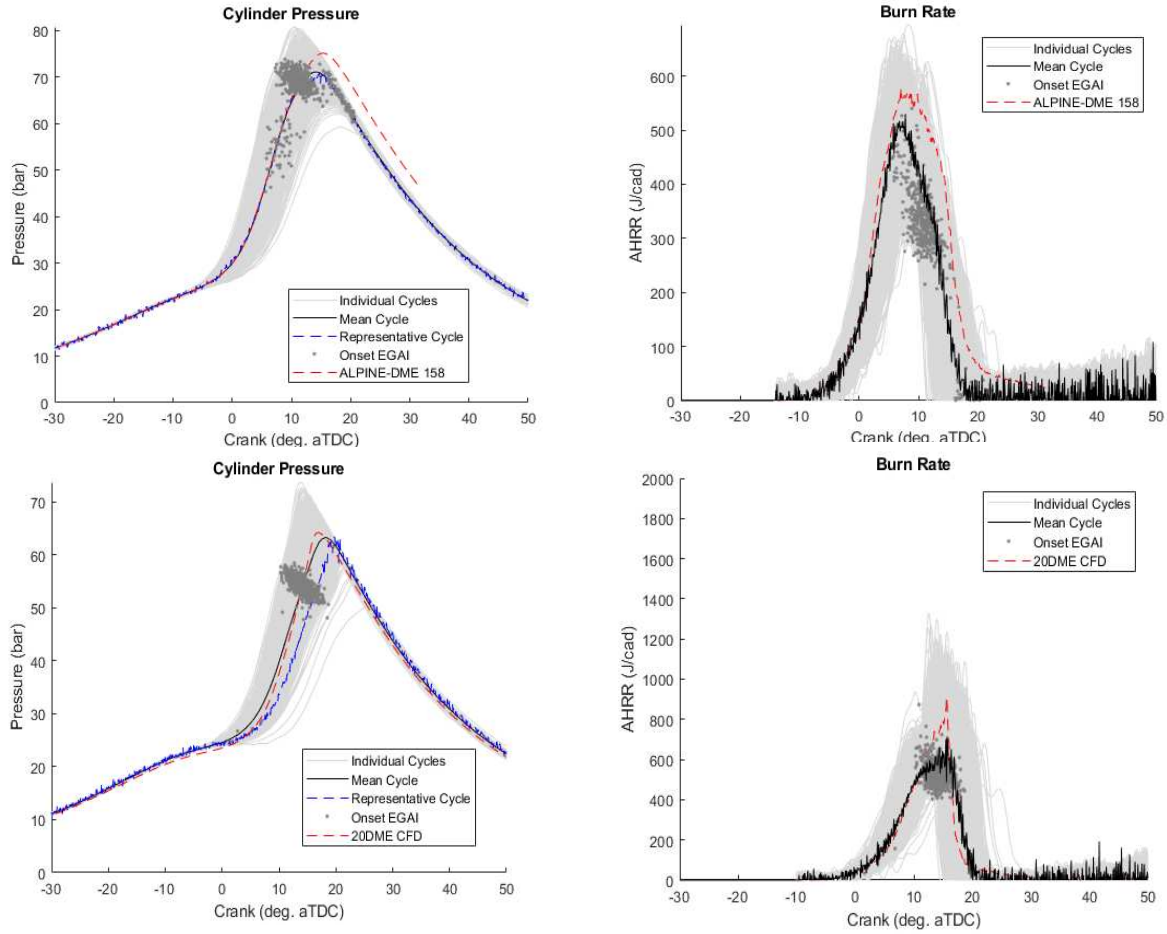

Figure 6.25. Experimental In-cylinder pressure, apparent heat release rate, and knock onset crank angle for 100% LPG and 20% DME graphed against the ALPINE-DME 158 CONVERGE 3D engine simulations.

For the 100% LPG case, the ALPINE-DME 158 simulations successfully captured the AHRR profile, with the simulated curve falling directly within the 1000-cycle experimental envelope. However, a slight over-pressurization remains visible during the power stroke. Because this specific pressure deviation was observed in both the UCSD and ALPINE simulations despite

the AHRR matching the experiments, it suggests that the discrepancy is not rooted in the chemical kinetics. Instead, this behavior indicates that the CONVERGE model parameters, such as the wall heat transfer coefficients or specific boundary conditions (e.g., liner temperatures or crevice volume effects), may require further optimization to fully replicate the expansion stroke thermodynamics seen in the experimental test cell. Critically, the ALPINE-DME 158 successfully resolved the 20% DME case without the unphysical reactivity spikes observed in the baseline models. The mechanism effectively balanced the increased radical activity of the DME blend, providing a pressure trace and heat release rate that consistently follows the experimental data. This success confirms that the ALPINE-DME 158 is the most reliable framework for exploring the performance limits of high-reactivity LPG/DME blends in heavy-duty SI engines.

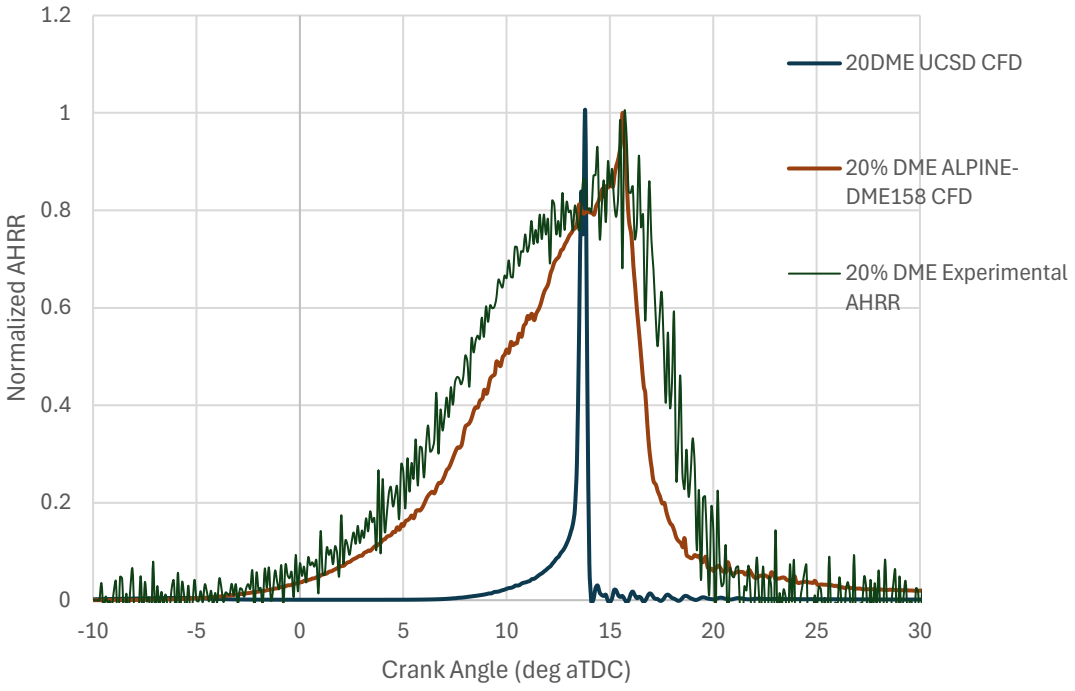

Figure 6.26. Normalized Apparent Heat Release Rate (AHRR) for the 20% DME experimental test point compared to the two simulated mechanisms, UCSD and ALPINE-DME 158.

Figure 6.26 displays a comparison of the normalized AHRR traces, benchmarking the experimental results against the simulated curves from both the UCSD and ALPINE-DME 158 mechanisms. The normalization of these traces is essential for developing a deeper insight into the kinetic failures of the legacy models when applied to the 20% DME blend. A review of the ALPINE-DME 158 trace reveals that it directly follows the experimental behavior, accurately resolving the total duration of the heat release event. Furthermore, the mechanism successfully captures the secondary End-Gas Autoignition (EGAI) event observed in the experiments, demonstrating its ability to simultaneously resolve both flame propagation and autoignition chemistry within the same cylinder volume. Conversely, the UCSD mechanism exhibits drastic deviations from the experimental data. While the experimental heat release duration spans approximately 30° crank angle, the UCSD mechanism releases nearly all of its chemical energy within a extremely narrow window of 1–2°, essentially acting like a constant-volume explosion rather than a propagating flame. This confirms that it lacks the necessary intermediate species or reaction pathways to buffer the heat release in a blended fuel environment. This unphysical step-function behavior indicates that the UCSD mechanism cannot accurately calculate the progressive breakdown of the blended fuel into the radical pool. Instead of a controlled combustion event, the mechanism triggers an instantaneous global reaction, releasing the entire energy budget at once. This comparison confirms that the ALPINE-DME 158 is uniquely capable of capturing the complex, multi-stage oxidation pathways required for reliable 3D engine simulations of LPG/DME mixtures.

To isolate the chemical drivers behind the heat release discrepancies observed in Figure 6.26, a comparative analysis of key intermediate species was performed. Figure 6.27 and 6.28 illustrates the evolution of OH, H2O2, CH2O, and HO2 concentrations leading up to the point of

ignition for both the UCSD and ALPINE-DME 158 mechanisms. The species traces provide a definitive chemical justification for the UCSD mechanism's failure in 3D simulations. In the UCSD model (solid lines), there is an excessive and premature accumulation of CH2O and H2O2 beginning as early as -15° CAD. This indicates that while the mechanism initiates the fuel breakdown, it lacks the intermediate consumption reactions required to transition these species into the final radical pool. This results in a chemical bottleneck where energy is stored in these intermediates until approximately 13° CAD, where they are consumed instantaneously. This triggers the unphysical, 1–2° CAD constant-volume explosion observed in the previous AHRR traces. This explosion is substantiated by the instantaneous rise in OH production for the UCSD mechanism.

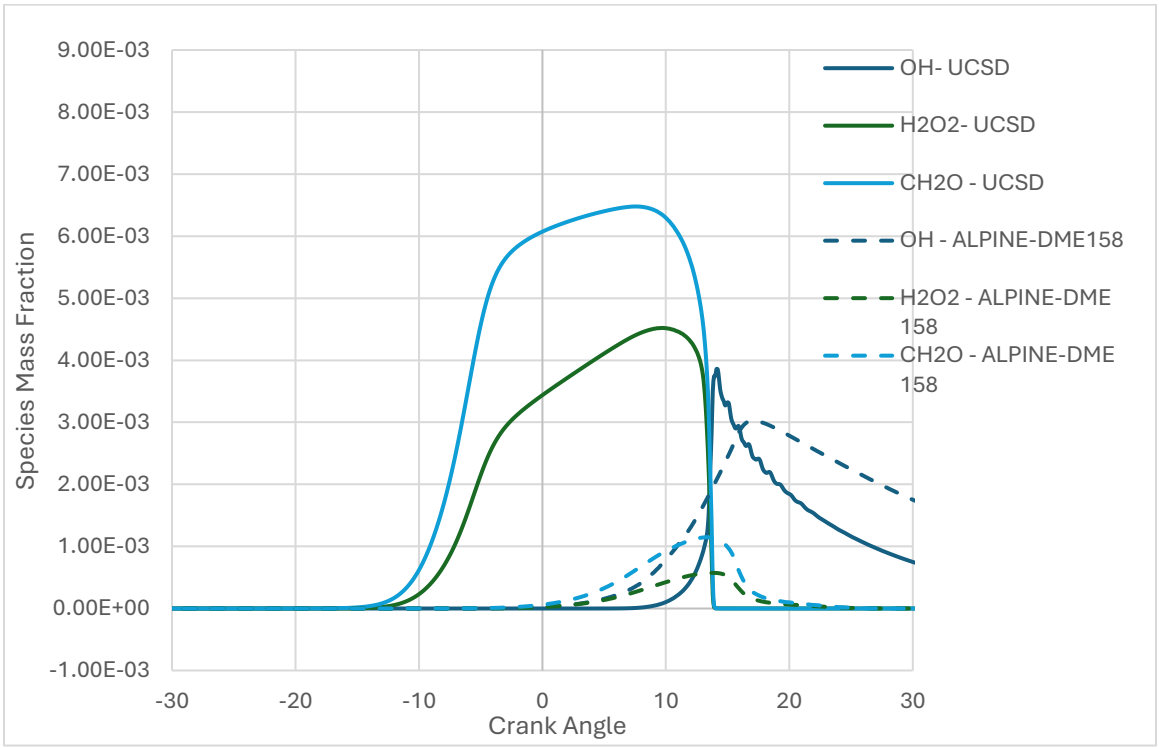

Figure 6.27. H2O2, CH2O, and OH species mass fraction vs Crank angle for the UCSD and ALPINE-DME158 mechanisms

In contrast, the ALPINE-DME 158 (dashed lines) displays a significantly more controlled and physically accurate rise in radical species. The mass fractions of CH2O and H2O2 are maintained at a much lower, realistic magnitude, peaking closer to the actual point of ignition. This demonstrates that the mechanism is correctly balancing the production and consumption of intermediates. Furthermore, the OH radical trace for the ALPINE-DME 158 mechanism shows a gradual, sustained rise that persists through the expansion stroke, mirroring the 30° CAD heat release duration seen experimentally. By correctly resolving this kinetic buffering, the ALPINE-DME 158 proves its ability to capture the complex, multi-stage oxidation physics required for heavy-duty SI engine modeling.

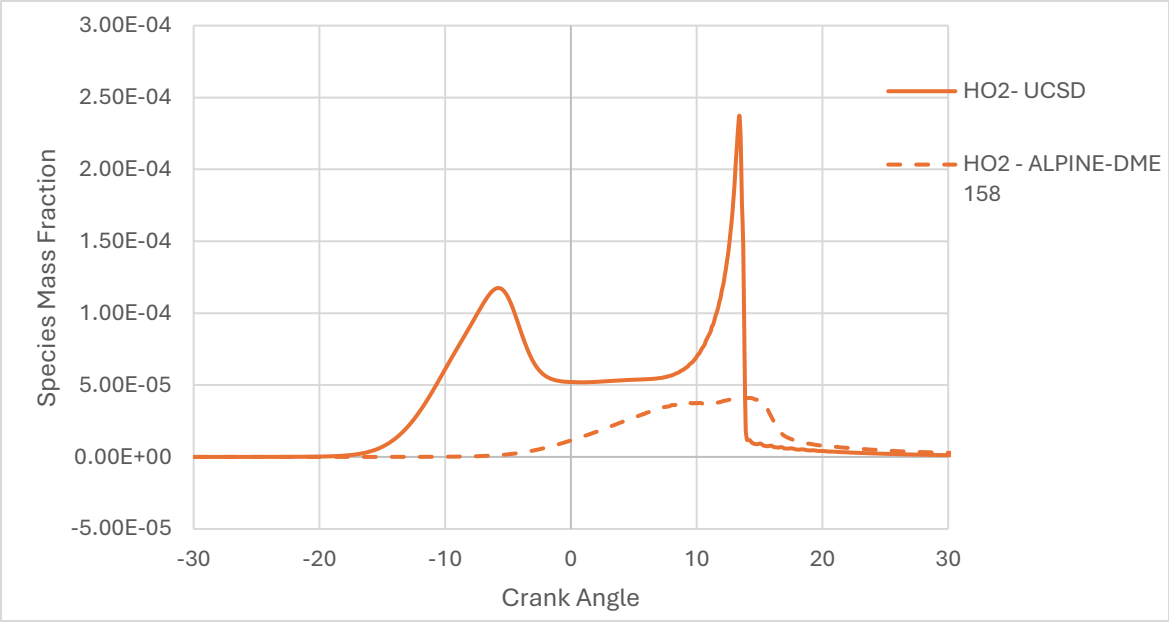

Figure 6.28. HO2 species mass fraction vs Crank angle for the UCSD and ALPINE-DME158 mechanisms

To further investigate the root cause of the radical bottlenecking observed in the previous figures, Figure 6.28 isolates the mass fraction of the HO2 for both mechanisms. The HO2 evolution

provides critical insight into the low-temperature heat release (LTHR) behavior that precedes the main ignition event. As seen in the figure, the UCSD mechanism (solid line) exhibits a prominent and premature HO2 peak near -5° aTDC. This indicates an over-sensitivity to the low-temperature kinetic pathways, where the mechanism aggressively initiates the first-stage oxidation of the DME/LPG blend. This early surge in HO2 acts as a catalyst for the excessive production of H2O2 and CH2O seen in Figure 6.27. Effectively, the UCSD mechanism pre-loads the cylinder with high concentrations of these intermediates, which, lacking sufficient consumption pathways, remain stagnant until they trigger the sudden, explosive energy release at the point of ignition. In contrast, the ALPINE-DME 158 (dashed line) displays a significantly suppressed HO2 profile during the compression stroke. It avoids the premature first-stage peak, instead showing a gradual rise that peaks concurrently with the main combustion event. This behavior aligns with experimental pressure traces, which do not show evidence of significant early-stage heat release. By accurately moderating the HO2 production, the ALPINE-DME 158 prevents the unphysical accumulation of radicals and provides a chemically stable transition into high-temperature combustion. This comparison confirms that the improved performance of the ALPINE mechanism is rooted in its superior handling of the specific chain-branching kinetics of oxygenated fuel blends.

The implementation of the ALPINE-DME 158 mechanism into the 3D CONVERGE environment marks the final stage of the tiered validation process. By successfully resolving the complex interaction between turbulent flame propagation and end-gas autoignition in the 20% DME blend, a case where the UCSD mechanism predicted a non-physical constant-volume explosion, the new mechanism has proven its reliability for high-pressure, boosted engine simulations. While minor deviations in expansion stroke pressure suggest that the CFD boundary conditions and heat transfer models could benefit from further localized tuning, the chemical

accuracy of the heat release rate is now firmly established. The ALPINE-DME 158 correctly identifies the timing and magnitude of energy release across the 0–20% DME range, providing a high-fidelity computational tool for the subsequent analysis of engine performance, efficiency, and knock-limited operation.

6.4 Conclusions

The experimental evaluation of LPG/DME blends on the Cummins X15 platform demonstrates a clear departure from the performance limits of a standard NG baseline. Across both high and low load regimes, the introduction of DME provides chemical pathways that fundamentally restructure the combustion process.

At high-load conditions, transitioning from NG to LPG-based fuels reduced the CA10-90 burn duration by 3–5° CAD, providing an immediate thermodynamic advantage through faster energy release. While the LPG/DME blends exhibited significant reactivity, the Brake Thermal Efficiency (BTE) for all these fuels did not vastly deviate from the 100% LPG baseline; in fact, the blends often performed better at more delayed timings. This behavior highlights the critical need for CA50 optimization to balance the faster burn rates with mechanical constraints. Furthermore, the f-EGAI increased for all DME/LPG blends relative to the baseline fuels, which directly explains the substantial efficiency gains observed compared to the NG operation. This intensified autoignition peaked at 28.8% for the 20% DME concentration, signaling a transition from Type 1 to Type 2 EGAI. Despite high knock intensity (MAPO) levels nearing 5.87 bar at the 20% DME limit, the engine maintained exceptional stability with a COV of IMEP less than 3%, averaging approximately 1.25%.

At lower loads, the high reactivity of the blends enabled a massive efficiency recovery, where the 30% DME blend achieved a peak of 41.1% BTE, representing a significant jump from the 34.6% observed with the NG baseline. Unlike high-load conditions where EGAI poses a knock risk, the low-load regime allowed for constructive autoignition; a 30% DME blend reached an f-EGAI of 17.3% while maintaining a MAPO of only 3.1 bar, which is comparable to standard NG operation. This addition of DME increased peak in-cylinder pressure by 5–10 bar relative to NG, and analysis of 1,000-cycle pressure overlays confirms that this increased pressure does not compromise stability, as COV IMEP values remained between 0.9% and 1.3%.

The research presented in this chapter successfully developed and validated the ALPINE-DME 158 chemical kinetic mechanism through a tiered computational approach, spanning from fundamental 0D and 1D reactor models to high-fidelity 3D internal combustion engine simulations. By benchmarking this new mechanism against industry standards like the UCSD, newly created USC_LLNL, and Aramco 3.0 models, a clear understanding of the unique kinetic requirements for LPG/DME blends was established. The initial 0D autoignition studies revealed that the ALPINE-DME 158 mechanism provides superior accuracy in the Negative Temperature Coefficient (NTC) regime, specifically at the high-pressure conditions (up to 30 bar) relevant to modern heavy-duty engines. While legacy mechanisms often over-predicted reactivity in the low-temperature range, the current model correctly resolved the ignition delay times across the 0–100% DME spectrum. Similarly, 1D laminar flame speed simulations across a wide range of equivalence ratios confirmed that the mechanism accurately captures the spatial propagation characteristics of the fuel blends, providing the foundational physics necessary for the subsequent 3D engine analysis. The implementation of the mechanisms into a 3D CONVERGE model of the Cummins X15 engine highlighted the catastrophic failures of legacy kinetics when coupled with real-world

fluid dynamics. The UCSD mechanism failed to resolve the 20% DME blend, predicting a non-physical constant-volume explosion with pressure peaks of 95 bar and heat release durations of only 1–2° CAD. In contrast, the ALPINE-DME 158 demonstrated excellent agreement with experimental data, accurately capturing the 30° CAD heat release duration and the specific End-Gas Autoignition (EGAI) events observed in the test cell.

Detailed species analysis provided the chemical smoking gun for these observations. It was determined that the UCSD mechanism suffers from a radical bottleneck, characterized by:

- Premature HO2 Production: A significant first-stage peak at -5° aTDC that over sensitizes the mixture.
- Intermediate Accumulation: An unphysical buildup of CH2O and H2O2 mass fractions, which are not consumed at a rate consistent with experimental energy release.
- Instantaneous Radical Discharge: The sudden consumption of this built-up radical reservoir, leading to the explosive pressure rise rates that deviate from physical reality.

The ALPINE-DME 158 mechanism resolves these discrepancies by correctly balancing the production and consumption of intermediate species. By maintaining realistic radical concentrations and resolving the kinetic buffering required for oxygenated fuels, this mechanism provides a robust, validated framework for the design of LPG/DME SI engines. This work confirms that accurate low-to-intermediate temperature kinetics are the primary requirement for extending the knock-limited operating range of high-reactivity alternative fuels in heavy-duty applications.

CHAPTER 7 CONCLUSIONS AND FUTURE WORK RECOMMENDATIONS

7.1 Conclusions

This dissertation presented a multi-scale investigation into the development of high-efficiency combustion strategies for heavy-duty SI engines utilizing LPG and LPG/DME blends. By integrating 3D CFD modeling, fundamental chemical kinetic development, and experimental validation on a Cummins X15 platform, this work successfully identified the pathways required to predict performance directly influencing efficiency gains.

This research begins by establishing a rigorous validation framework for the underlying physics of LPG combustion before proceeding to complex fuel blending. Initial 3D CONVERGE simulations utilized an extreme flash KH-RT spray model, which was validated against High-Pressure Schlieren and Mie-scattering data from a High-Pressure Spray Chamber (HPSC). The model successfully captured the rapid phase-change and high-velocity expansion characteristic of LPG flash-boiling, resolving the distinctive gaseous plume development and liquid penetration lengths observed experimentally. This fundamental validation ensured that the macroscopic mixture formation, specifically the transition between liquid and vapor phases was physically grounded before being applied to the dynamic environment of the engine cylinder.

The robustness of this coupled spray and chemical kinetic framework of the CSU ALPINE 153 mechanism was further demonstrated through 3D engine simulations benchmarking both Port Fuel Injection (PFI) and Direct Injection (DI) strategies. The numerical results for baseline LPG operation achieved excellent agreement with experimental data, with in-cylinder pressure traces falling consistently within the 1000-cycle experimental pressure envelope. A critical diagnostic discovery during this phase was the sensitivity of engine performance to atomization sub-models;

while early injection timings were largely insensitive to spray parameters due to extended residence time, late-injection strategies (-150° bTDC) proved to be a stress test for the physics. The failure of standard non-extreme KH-RT spray models to achieve ignition due to predicted liquid impingement and wall wetting contrasted with the success of the validated extreme flash model which justified the selection of the latter for the remainder of the study. This sequence established that the simulation framework could accurately resolve the high-pressure spray dynamics and radical interaction limits of LPG, providing a validated foundation for the subsequent investigation into LPG DI and PFI behavior.

Initial investigations into fluid dynamic drivers revealed that Direct Injection (DI) LPG operation is exclusively sensitive to Start of Injection (SOI) timing due to in-cylinder charge cooling and turbulent decay. It was determined that Turbulent Kinetic Energy (TKE) serves as a more critical driver for fuel preparation than residence time. Specifically, while intermediate timings suffered from a significant TKE decline after SOI 300°, the late-cycle timing of SOI 120° bTDC achieved a performance recovery by generating a TKE spike of approximately 15.5 m^2/s^2. This late-cycle TKE recovery reached values similar to those seen during the intake valve opening, providing the necessary aerodynamic shear to overcome the reduced residence time and effectively transfer fuel out of the piston bowl. This established the piston top velocity profile as a universal design parameter for optimizing DI timing across varying compression ratios.

To understand the effect of DME addition on a LPG base for concentrations up to 30%, further octane characterization on a CFR engine was required; revealed a non-linear promoting effect of rDME on LPG autoignition. A critical conclusion of this phase was that understanding the Motor Octane Number (MON) and Research Octane Number (RON) is essential, as these metrics directly translate to the chemical reactivity changes driven by DME addition. These values

define the operational boundaries of the fuel, determining whether a blend will achieve superior performance or be mechanically limited by excessive reactivity. Furthermore, the calculated Anti-Knock Index (AKI = (RON+MON)/2) demonstrated that a 30% DME blend provides a viable drop-in replacement for standard 89-octane gasoline. Morphological analysis confirmed that the addition of up to 30% rDME does not fundamentally alter the LPG spray structure or penetration lengths, providing the conclusion that existing DI hardware optimized for LPG can serve as a drop-in platform for LPG/DME blends without modification.

With the chemistry defined for LPG/DME blends, the work sought to explore if these blends are a viable option for heavy-duty SI operation. Experimental testing on the Cummins X15 platform demonstrated a significant departure from Natural Gas (NG) performance limits. At low loads, the 30% DME blend achieved a peak Brake Thermal Efficiency (BTE) of 41.1%, representing a 6.5% absolute gain over the NG baseline. At high-load conditions, the 20% DME blend achieved the greatest overall efficiency, reaching a peak BTE of 42.9% and surpassing the 100% LPG baseline at delayed timings. The 20% DME blend achieved an absolute gain of 3.9% over the highest BTE observed with the NG baseline. These gains were facilitated by leveraging constructive Type 1 End Gas Autoignition (EGAI). Although intensified reactivity of the 20% DME test fuel triggered Type 2 EGAI at high loads, stable operation was maintained through CA50 optimization, achieving a COV of IMEP below 1.25% despite an increase in knock intensities.

Finally, the research successfully developed and validated the ALPINE-DME 158 mechanism. A key strength of this mechanism is its capability to accurately calculate both autoignition delay times and laminar flame speeds for the full range of LPG/DME blends (100% LPG to 100% DME). Where both IDT and LFS were rigorously validated against experimental data from literature. Crucially, the implementation of this mechanism into 3D CONVERGE

simulations of the Cummins X15 platform demonstrated its high-fidelity predictive capabilities in real-world engine environments. Unlike legacy kinetics which predicted non-physical, explosive pressure rises when coupled with 3D fluid dynamics, the ALPINE-DME 158 accurately captured both the in-cylinder pressure, the heat release duration and specific end gas autoignition events observed in the test cell for 100% LPG and 20% DME test fuels. By resolving radical bottlenecks specifically premature HO2 production and unphysical H2O2 accumulation seen in legacy models, the ALPINE-DME 158 correctly balanced intermediate species consumption. This provides a robust framework for resolving the kinetic buffering required for oxygenated fuels in 3D CFD environments, effectively narrowing the efficiency gap between SI and diesel architectures.

7.2 Recommendations for Future Work

Characterizing the combustion properties and process of LPG/DME blends has opened several possible pathways for future work. The following recommendations build upon the current findings. Although the ALPINE-DME 158 mechanism was successfully validated against experimental benchmarks, future work should extend the 3D CFD validation campaign to encompass the full range of investigated intermediate blends, specifically 5%, 10%, 15%, and 30% DME. This will ensure that the chemical kinetic mechanism maintains predictive accuracy across the non-linear autoignition landscape. The current study highlighted a significant limitation in the availability of Rapid Compression Machine (RCM) data for LPG/DME blends at engine-relevant pressures. Future experimental campaigns should prioritize generating high pressure ignition delay data over an entire temperature sweep. Filling this data void is essential for further refining the pressure dependent reactions within the ALPINE-DME 158 mechanism and reducing the uncertainty in end-gas autoignition predictions. A critical research opportunity lies in evaluating the Exhaust Gas Recirculation (EGR) tolerance of LPG/DME blends. Historically, the transition

from natural gas to LPG allowed for tighter combustion control; it is hypothesized that the increased reactivity of DME may allow for even higher EGR rates compared to base LPG. Future work should systematically map the trade-off between DME-induced reactivity and dilution-induced stability. Establishing these EGR limits will be vital to determining the maximum brake thermal efficiency (BTE) achievable while maintaining low NOx emissions, mirroring the historical optimization trends observed in the shift from natural gas to LPG combustion architectures. Finally, this work has provided the fundamental spray and kinetic validation required for heavy-duty deployment. The natural progression is to extend these findings into full-load, heavy-duty Direct Injection (DI) operational maps. Investigating the hardware durability and combustion stability under transient, multi-load, and multi-speed regimes while utilizing the high-reactivity blends will provide the commercial validation necessary to position LPG/DME as a viable drop-in strategy for existing heavy-duty platforms.

References

[1] U.S. Energy Information Administration, “U. S. energy facts explained,” August 16,2023, https://www.eia.gov/energyexplained/us-energy-facts/#:~:text=In%202022%2C%20production%20was%20102.92,primary%20energy%20production%20in%202022.

[2] Werpy, Marcy & Burnham, Andrew & Bertram, Kenneth. (2010). White Paper on Propane Vehicles: Status, Challenges, and Opportunities. 10.2172/982693.

[3] Walls, M., Joo, M., and Ross, M., "Impact of the Direct Injection of Liquid Propane on the Efficiency of a Light-Duty, Spark-Ignited Engine," SAE Technical Paper 2017-01-0865, 2017, doi:10.4271/2017-01-0865.

[4] “Alternative Fuels Data Center: Fuel Properties Comparison,” accessed December 2024, https://afdc.energy. gov/fuels/properties.

[5] McLean, L. and El-Sayed, M., "Commercial Viability Study for LPG as Alternative Mass Transportation Fuel," SAE Technical Paper 2015-01-1679, 2015, doi:10.4271/2015-01-1679.

[6] U.S. Department of Energy, “Alternative Fuels Data Center, Propane basics,” https://afdc.energy.gov/fuels/propane_benefits.html#:~:text=Also%20known%20as%20liquefied%20petroleum,the%20environmental%20impacts%20of%20vehicles

[7] U.S. Energy Information Administration, “Short-Term Energy Outlook Data Browser,” Available at https://www.eia.gov/outlooks/steo/data/browser/#/?v=27&f=M&s=0&start=199701&end=202512&linechart=PRFPPUS~&maptype=0&ctype=linechart&map=&id=

[8] U.S. Energy Information Administration, “U.S. propane exports established a new record in December 2023,” Available at https://www.eia.gov/todayinenergy/detail.php?id=61564

[9] Tanmay Kar, Toluwalase Fosudo, Anthony Marchese, Bret Windom, Daniel Olsen, Effect of fuel composition and EGR on spark-ignited engine combustion with LPG fueling: Experimental and numerical investigation, Fuel, Volume 327, 2022, 125221, ISSN 0016-2361, https://doi.org/10.1016/j.fuel.2022.125221.

[10] U.S. Department of Energy, “Alternative Fuels Data Center, Propane basics,” Available at https://afdc.energy.gov/fuels/propane_benefits.html#:~:text=Also%20known%20as%20liquefied%20petroleum,the%20environmental%20impacts%20of%20vehicles

[11] Fosudo, T., Kar, T., Windom, B., Schlagel, J. et al., “Performance, Combustion and Emissions Evaluation of Liquid Phase Port Injected LPG on a Single Cylinder Heavy-Duty Spark Ignited Engine,” SAE Technical Paper 2023-01-0245, 2023, doi:10.4271/2023-01- 0245.

[12] Fosudo, T., Kar, T., Marchese, A., Windom, B. et al., “The Impact of LPG Composition on Performance, Emissions, and Combustion Characteristics of a Pre-mixed Spark-Ignited CFR Engine,” SAE Technical Paper 2022-01-0476, 2022, doi:10.4271/2022-01-0476

[13] Dube, A., Vivekanand, M., and Ramesh, A., "Experimental Studies on Liquid Phase LPG Direct Injection on a Two-Stroke SI Engine," SAE Int. J. Engines 12(3):341-356, 2019, https://doi.org/10.4271/03-12-03-0023

[14] Elana M. Chapman, André L. Boehman, Pilot ignited premixed combustion of dimethyl ether in a turbodiesel engine, Fuel Processing Technology, Volume 89, Issue 12, 2008, Pages 1262-1271, ISSN 0378-3820, https://doi.org/10.1016/j.fuproc.2008.08.010.

[15] Eirich, J., Chapman, E., Glunt, H., Klinikowski, D., Boehman, A. L., Hansel, J. G., & Heydorn, E. C. (2003). Development of a Dimethyl Ether (DME)-Fueled Shuttle Bus. *SAE Transactions*, *112*, 348–360. http://www.jstor.org/stable/44742268

[16] Prabhakar, B., Jayaraman, S., Vander Wal, R., and Boehman, A. (April 1, 2015). "Experimental Studies of High Efficiency Combustion with Fumigation of Dimethyl Ether and Propane Into Diesel Engine Intake Air." ASME. *J. Eng. Gas Turbines Power*. April 2015; 137(4): 041505. https://doi.org/10.1115/1.4028616

[17] "Emissions and Performance Benchmarking of a Prototype Dimethyl Ether-FueledHeavy-Duty Truck" https://afdc.energy.gov/files/u/publication/ornl_dme_tm-2014-59.pdf

[18] U.S. Department of Energy, "Alternative Fuels Data Center, Dimethyl Ether,"

https://afdc.energy.gov/fuels/emerging_dme.html#:~:text=The%20energy%20efficiency%20and%20power,for%20costly%20diesel%20particulate%20filters.\

[19] Patrik Soltic, Thomas Hilfiker, Yuri Wright, Gilles Hardy, Benjamin Fröhlich, Daniel Klein, "The potential of dimethyl ether (DME) to meet current and future emissions standards in heavy-duty compression-ignition engines", Fuel, Volume 355, 2024, 129357, ISSN 0016-2361, https://doi.org/10.1016/j.fuel.2023.129357.

[20] Cristina Peinado, Dalia Liuzzi, Soraya N. Sluijter, Galina Skorikova, Jurriaan Boon, Simone Guffanti, Gianpiero Groppi, Sergio Rojas, "Review and perspective: Next generation DME

synthesis technologies for the energy transition", Chemical Engineering Journal, Volume 479, 2024, 147494, ISSN 1385-8947, https://doi.org/10.1016/j.cej.2023.147494.

[21] P. Styring, P.W. Sanderson, I. Gell, G. Skorikova, C. S´ anchez-Martínez, G. Garcia-Garcia, S.N. Sluijter, Carbon footprint of Power-to-X derived dimethyl ether using the sorption enhanced DME synthesis process, Front. Sustain. 3 (2022), https:// doi.org/10.3389/frsus.2022.1057190.

[22] De Falco, M. *Dimethyl ether (DME) production*. Dimethyl Ether (DME) Production-Oil & Gas Portal. https://www.oil-gasportal.com/dimethyl-ether-dme-production-2/?print-fdp&print=print#_ftn8

[23] Oberon Fuels, Low CI LPG, https://www.oberonfuels.com/low-ci-lpg [accessed November 2024].

[24] Oil and Energy Online, "https://oilandenergyonline.com/articles/all/possibilities-renewable-propane/#:~:text=Renewable%20propane%20is%20chemically%20identical,diesel%20and%20sustainable%20aviation%20fuel."

[25] Biopropane Production Methods (2010), https://www.alkcon.com/documents/biopropane_production_methods.pdf

[26] The Engineering ToolBox (2003). *Fuels - Higher and Lower Calorific Values*. [online] Available at: https://www.engineeringtoolbox.com/fuels-higher-calorific-values-d_169.html.

[27] Zheng Chen, Xiao Qin, Yiguang Ju, Zhenwei Zhao, Marcos Chaos, Frederick L. Dryer, *High temperature ignition and combustion enhancement by dimethyl ether addition to methane–air mixtures*, Proceedings of the Combustion Institute, Volume 31, Issue 1, 2007, Pages 1215-1222, ISSN 1540-7489, https://doi.org/10.1016/j.proci.2006.07.177

[28] Yingjia Zhang, Kieran P. Somers, Marco Mehl, William J. Pitz, Roger F. Cracknell, Henry J. Curran, Probing the antagonistic effect of toluene as a component in surrogate fuel models at low temperatures and high pressures. A case study of toluene/dimethyl ether mixtures, Proceedings of the Combustion Institute, Volume 36, Issue 1, 2017, Pages 413-421, ISSN 1540-7489, https://doi.org/10.1016/j.proci.2016.06.190.

[29] Soto, L., Han, T., and Boehman, A., "Effects of Dimethyl Ether and Propane Blends on Knocking Behavior in a Boosted SI Engine," SAE Int. J. Engines 17(7):2024, doi:10.4271/03-17-07-005

[30] T. Fosudo, Development of Advanced Combustion Strategies For Heavy Duty LPG Engines To Achieve Near-Diesel Efficiency, PhD thesis, Colorado State University, Fort Collins, CO, United States, 2024.

[31] Dong S, Wagnon SW, Pratali Maffei L, Kukkadapu G, Nobili A, Mao Q, Pelucchi M, Cai L, Zhang K, Raju M, Chatterjee T, Pitz WJ, Faravelli T,Pitsch H, Senecal PK, Curran HJ.A new detailed kinetic model for surrogate fuels: C3MechV3.3. Applications in Energy and Combustion Science 2022.

[32] C-W. Zhou, Y. Li, U. Burke, C. Banyon, K.P. Somers, S. Khan, J.W. Hargis, T. Sikes, E.L. Petersen, M. AlAbbad, A. Farooq, Y. Pan, Y. Zhang, Z. Huang, J. Lopez, Z. Loparo, S.S. Vasu, H.J. Curran "An experimental and chemical kinetic modeling study of 1,3-butadiene combustion: Ignition delay time and laminar flame speed measurements" Combustion and Flame 197 (2018) 423–438.

[33] Erjiang Hu, Zihang Zhang, Lun Pan, Jiaxiang Zhang, and Zuohua Huang, “Experimental and Modeling Study on Ignition Delay Times of Dimethyl Ether/Propane/Oxygen/Argon Mixtures at 20 bar,” Energy & Fuels 2013 27 (7), 4007-4013 DOI: 10.1021/ef4009967

[34] Z. Zhao, M. Chaos, A. Kazakov, and F. L. Dryer, “Thermal decomposition reaction and a comprehensive kinetic model of dimethyl ether,” *Int J of Chemical Kinetics*, vol. 40, no. 1, pp. 1–18, Jan. 2008, doi: 10.1002/kin.20285.

[35] Wang, H.; You, X. Q.; Joshi, A. V.; Davis S. G.; Laskin, A.;Egolfopoulos, F.; Law, C. K. USC Mech Version II. High-Temperature Combustion Reaction Model of H 2 /CO/C1−C4 Compounds; http://ignis.usc.edu/USC_Mech_II.htm

[36] Fischer, S. L., F. L. Dryer, and H. J. Curran, "The Reaction Kinetics of Dimethyl Ether. I: High-Temperature Pyrolysis and Oxidation in Flow Reactors," *Int. J. Chem. Kinet.* **32**: 713–740, 2000. Lawrence Livermore National Laboratory, Livermore, CA, *UCRL-JC-239461*.

[37] Curran, H. J., S. L. Fischer, and F. L. Dryer, "The Reaction Kinetics of Dimethyl Ether. II: Low-Temperature Pyrolysis and Oxidation in Flow Reactors," *Int. J. Chem. Kinet.* **32**: 741–759, 2000. Lawrence Livermore National Laboratory, Livermore, CA, *UCRL-JC-239496*.

[38] Kaiser, E. W., T. J. Wallington, M. D. Hurley, J. Platz, H. J. Curran, W. J. Pitz, and C. K. Westbrook, “Experimental and Modeling Study of Premixed Atmospheric-Pressure Dimethyl Ether-Air Flames,” *Journal of Physical Chemistry A* **104**, No. 35, 8194-8206 (2000), Lawrence Livermore National Laboratory, Livermore, CA, *UCRL-JC-136123*.

[39] "Chemical-Kinetic Mechanisms for Combustion Applications", San Diego Mechanism web page, Mechanical and Aerospace Engineering (Combustion Research), University of California at San Diego (http://combustion.ucsd.edu).

[40] Enoch E. Dames, Andrew S. Rosen, Bryan W. Weber, Connie W. Gao, Chih-Jen Sung, William H. Green, *A detailed combined experimental and theoretical study on dimethyl ether/propane blended oxidation*, Combustion and Flame, Volume 168, 2016, Pages 310-330, ISSN 0010-2180, https://doi.org/10.1016/j.combustflame.2016.02.021.

[41] Felipe, J., Rueda, R., Olsen, D. B., Windom, B., Baker, D., & Quinn, J. (2023). Expanding The Knock/Emissions Limits for The Realization of Ultra-Low Emissions, High-Efficiency Heavy-Duty Natural Gas Engines. Colorado State University, PhD Dissertation.

[42] Rodriguez, J.F., Xu, H., Hampson, G., Windom, B., Marchese, A. and Olsen, D.B. (2022) Heavy Duty Natural Gas Single Cylinder Research Engine Installation, Commissioning, and Baseline Testing. Energy and Power Engineering, 14, 217-232. https://doi.org/10.4236/epe.2022.146012

[43] Rodriguez, J.F., Xu, H., Hampson, G., Bestel, D. et al., “Innovative Piston Design Performance for High Efficiency Stoichiometric Heavy Duty Natural Gas Engine,” SAE Technical Paper 2023-01-0288, 2023, doi:10.4271/2023-01-0288.

[44] T. Kar, T. Fosudo, B. Windom, D. Olsen, J. Hoke, J. Rogers, Development of a liquid-phase LPG delivery system for direct injection, spark-ignited engines, in: Internal Combustion Engine Division Fall Technical Conference, Vol. 86540, American Society of Mechanical Engineers, 2022, p. V001T07A005

[45] Fosudo, T., Windom, B., and Olsen, D., “Experimental Evaluation of Direct and Port Fuel Injection Strategies on a Heavy-Duty Liquefied Petroleum Gas Engine,” SAE Int. J. Engines 18(3):403-421, 2025, doi:10.4271/03-18-03-0022.

[46] Heywood, J.B., Internal Combustion Engine Fundamentals (New York, USA: McGraw-Hill, 1988)

[47] J. Wheeler, A. R. A. R. Ganji, Introduction to engineering experimentation / Anthony J. Wheeler, Ahmad R. Ganji; with contributions by V. V. Krishnan, Brian S. Thurow, 3rd Edition, Pearson Higher Education, Upper Saddle River, N.J., 2010.

[48] Richards, K.J., Senecal, P.K., and Pomraning, E., CONVERGE 4.1.2, 2024.

[49] Han Z, Reitz RD. Turbulence Modeling of Internal Combustion Engines Using RNG κ - ε Models Turbulence Modeling of Internal Combustion Engines Using RNG k-E Models 2007;2202. https://doi.org/10.1080/00102209508907782.

[50] Han, Z. and Reitz, R.D. (1997) A Temperature Wall Function Formulation for Variable Density Turbulent Flows with Application to Engine Convective Heat Transfer Modeling. International Journal of Heat and Mass Transfer, 40, 613-625. http://dx.doi.org/10.1016/0017-9310(96)00117-2

[51] Slunecka, C., Zdanowicz, A., Bhoite, S., Vaughan, S., Olsen, D., and Marchese, A.J., “Autoignition of Premixed Liquefied Petroleum Gas in a Rapid Compression Machine: Experimental Results and Chemical Kinetic Mechanism Reduction,” in 12th U.S. National Combustion Meeting by the Central States Section of the Combustion Institute, 1-10, 2021.

[52] C. Slunecka. (2023). Autoignition and flame speed of premixed liquefied petroleum gas in a rapid compression machine: Experimental results and reduced chemical kinetic mechanism. Master's thesis, Colorado State University.

[53] Dukowicz, J.K., "A Particle-Fluid Numerical Model for Liquid Sprays," Journal of Computational Physics 35, no. 2 (1980): 229-253, doi:10.1016/0021-9991(80)90087-X

[54] Reitz, R.D. and Beale, J.C., "Modeling Spray Atomization with the Kelvin Helmholtz/Rayleigh-Taylor Hybrid Model," Atomization and Sprays 9, no. 6 (1999): 623-650,

[55] Amsden, A., O'Rourke, P., and Butler, T., "KIVA-II: A Computer Program for Chemically Reactive Flows with Sprays, Los Alamos - National Laboratory, Report LA-11560MS," May, Los Alamos Natl. Lab., LA-11560-MS, 1989.

[56] Schmidt, D.P. and Rutland, C.J., "A New Droplet Collision Algorithm," Journal of Computational Physics 164, no. 1 (2000): 62-80, doi:10.1006/jcph.2000.6568.

[57] Adachi, M., McDonell, V.G., Tanaka, D., Senda, J. et al., "Characterization of Fuel Vapor Concentration Inside a Flash Boiling Spray," SAE Technical Paper 970871 (Feb. 1997), doi:10.4271/970871.

[58] Windell, B., Sharma, M., Nocivelli, L., Asztalos, K. et al., "Bulk Spray and Individual Plume Characterization of LPG and IsoOctane Sprays at Engine-Like Conditions," SAE Technical Paper 2022-01-0497, 2022, doi:10.4271/2022-01-0497.

[59] “Spray G Parametric Variation - Engine Combustion Network,” Engine Combustion Network, accessed December 2021, https://ecn.sandia.gov/gasoline-spray-combustion/ target-condition/spray-g-parametric-variation/.

[60] B. Y. Xu, X. C. Zhang, J. Xu, Y. L. Qi, and S. L. Cai, “Numerical analysis of homogeneous mixture formation for a direct injection liquid LPG engine,” *Int.J Automot. Technol.*, vol. 14, no. 6, pp. 857–865, Dec. 2013, doi: 10.1007/s12239-013-0094-z.

[61] X. Boyan, J. Longlong, S. Chaodong, and L. Yingchun, “Numerical Analysis of the Mixture Formation in a Two-Stroke Wall-Guided LPG DI Engine for Extended-Range Electric Vehicle,” *Int.J Automot. Technol.*, vol. 19, no. 2, pp. 313–321, Apr. 2018, doi: 10.1007/s12239-018-0030-3.

[62] B. Y. Xu, Y. L. Qi, C. D. Sun, and J. Z. Ma, “Numerical Investigation on Mixture Formation of Two-Stroke LPG Direct Injection Engine Used as Range Extender for Electric Car,” in *ASME 2016 Internal Combustion Engine Division Fall Technical Conference*, Greenville, South Carolina, USA: American Society of Mechanical Engineers, Oct. 2016. doi: 10.1115/icef2016-9334.

[63] ASTM International. Standard test method for Motor octane number of spark ignition engine fuel, designation D2700 2019.

[64] ASTM International. Standard test method for Research octane number of spark-ignition engine fuel, designation D2699 2019.

[65] Bayliff, M.S., *Evaluation of Controlled End Gas Auto-Ignition with Exhaust Gas Recirculation in a Stoichiometric, Spark Ignited, Natural Gas Engine* (Colorado State University, Mechanical Engineering, Thesis, 2020)

[66] Bayliff, S, Windom, B, Marchese, A, Hampson, G, Carlson, J, Chiera, D, & Olsen, D. "Controlled End Gas Auto Ignition With Exhaust Gas Recirculation on a Stoichiometric, Spark Ignited, Natural Gas Engine." *Proceedings of the ASME 2020 Internal Combustion Engine Division Fall Technical Conference*. *ASME 2020 Internal Combustion Engine Division Fall Technical Conference*. Virtual, Online. November 4–6, 2020. V001T03A011. ASME. https://doi.org/10.1115/ICEF2020-2979

[67] Wise, M.D., Olsen, B.D. and Kim, M., "Development of A Lean Burn Methane Number Measurement Technique for Alternative Gaseous Fuel Evaluation," in *Proc. ASME.ICEF2013, 2: Fuels; Numerical Simulation; Engine Design, Lubrication, and Applications*, V002T02A014, 2014, doi:10.1115/ICEF2013-19220.

[68] Hoth, A., Manchiraju, R., Andretti, C., Sinur, R. et al., "Towards Developing an Unleaded High Octane Test Procedure (RON>100) Using Toluene Standardization Fuels (TSF)," SAE Technical Paper 2020-01-2040, 2020, doi:10.4271/2020-01-2040

[69] Sharma, M., Windom, B., Yalin, A., and Yost, D., "Diagnostics and Characterization of Direct Injection of Liquified Petroleum Gas for Development of Spray Models at Engine-Like Conditions," Masters' Thesis, Colorado State University, Fort Collins, CO, United States, 2023.

[70] Ansys® Chemkin-Pro, Release 2023 R1, ANSYS Chemkin-Pro Model Fuel Library Getting Started Guide, 2.1. MFL Full Mechanisms, ANSYS, Inc.

[71] Vasu, S., Weiner, J., Kim, G., and Ghorpade, R., "Laminar Flame Speed Measurements of Propane/Dimethyl-Ether/Air Mixtures," SAE Technical Paper 2022-01-0510, 2022, doi:10.4271/2022-01-0510

[72] Nocivelli, L., Sforzo, B., Tekawade, A., Yan, J. et al., “Analysis of the Spray Numerical Injection Modeling for Gasoline Applications,” SAE Technical Paper 2020-01-0330 (2020). https://doi.org/10.4271/2020-01-0330.

[73] Nocivelli, L., Zhang, A., Sforzo, B.A., Tekawade, A., et al., “Comparison Between a Center-Mounted and a SideMounted Injector for Gasoline Applications: A Computational Study,” in ASME 2020 Internal Combustion Engine Division Fall Technical Conference, ICEF 2020, December 2020, doi: 10.1115/ICEF2020-2991.

[74] Guo, H., Nocivelli, L., and Torelli, R., “Numerical Study on Spray Collapse Process of ECN Spray G Injector Under Flash Boiling Conditions,” Fuel 290 (2021): 119961, doi:10.1016/j.fuel.2020.119961.

[75] Nocivelli, L., Yan, J., Saha, K., Magnotti, G.M., et al., “Effect of Ambient Pressure on the Behavior of Single-Component Fuels in a Gasoline Multi-Hole Injector,” in ASME 2019 Internal Combustion Engine Division Fall Technical Conference, ICEF 2019, December 2019, doi: 10.1115/ICEF2019-7258.

[76] Morganti KJ, Foong TM, Brear MJ, Da Silva G, Yang Y, Dryer FL. The Research and Motor octane numbers of Liquefied Petroleum Gas (LPG). Fuel 2013; 108:797–811. https://doi.org/10.1016/j.fuel.2013.01.072.

[77] Boldt, K., "Motor (LP) Knock Test Method Development," SAE Technical Paper 670055, 1967, https://doi.org/10.4271/670055

[78] Lee, T.S., Sung, J.Y., and Park, D.J., "Experimental Investigations on the Deflagration Explosion Characteristics of Different DME-LPG Mixtures," *Fire Safety Journal* 49 (2012): 62-66. https://doi.org/10.1016/j.firesaf.2011.12.003.

[79] Mittal, V., Heywood, J. B., & Green, W. H. (2010). The Underlying Physics and Chemistry behind Fuel Sensitivity. *SAE International Journal of Fuels and Lubricants*, *3*(1) ,256–265. http://www.jstor.org/stable/26272655

[80] Arunabha Basu, Christopher Mccarthy, Theo Fleisch, Carl Udovich. AMOCO Coporation. *Process and Fuel for Spark Ignition Engines*. International Patent Classification. PCT/US96/13331. 20 March 1997.

[81] Kar, T., Fosudo, T., Slunecka, C., Marchese, A. et al., "A Study of Propane Combustion in a Spark-Ignited Cooperative Fuel Research (CFR) Engine," SAE Technical Paper 2022-01-0404, 2022, doi:10.4271/2022-01-0404

[82] Rockstroh, T., Kolodziej, C., Goldsborough, S., Wallner, T. et al., "Insights into Engine Knock: Comparison of Knock Metrics across Ranges of Intake Temperature and Pressure in the CFR Engine," SAE Int. J. Fuels Lubr. 11(4):545–561, 2018, doi:10.4271/2018-01-0210.

[83] Bernardi Bestel, D., Rodriguez, J., Marchese, A., Olsen, D. et al., "Detection and Onset Determination of End-Gas Autoignition on Spark-Ignited Natural Gas Engines Based on the Apparent Heat Release Rate," SAE Technical Paper 2022-01-0474, 2022, doi:10.4271/2022-01-0474

[84] Shamel S. Merchant, C. Franklin Goldsmith, Aäron G. Vandeputte, Michael P. Burke, Stephen J. Klippenstein, William H. Green, Understanding low-temperature first-stage ignition

delay: Propane, Combustion and Flame, Volume 162, Issue 10, 2015, Pages 3658-3673, ISSN 0010-2180, https://doi.org/10.1016/j.combustflame.2015.07.005.

[85] Mehl M., W.J. Pitz, C.K. Westbrook, H.J. Curran, "Kinetic modeling of gasoline surrogate components and mixtures under engine conditions," Proceedings of the Combustion Institute 33:193-200 (2011). Pages 193-200, ISSN 1540-7489, https://doi.org/10.1016/j.proci.2010.05.027.

[86] https://webbook.nist.gov/cgi/cbook.cgi?ID=C115106&Mask=4

[87] https://webbook.nist.gov/cgi/cbook.cgi?ID=C74986&Mask=4

[88] Zdanowicz, A., Mohr, J., Tryner, J., Gustafson, K. et al., “End-Gas Autoignition Fraction and Flame Propagation Rate in Laser-Ignited Primary Reference Fuel Mixtures at Elevated Temperature and Pressure,” Combustion and Flame 234 (2021): 111661.

[89] Reece Churchill, Manav Sharma, Daniel Olsen, Bret Windom, Suitability of DME/LPG blends for SI engines: Reactivity and spray characterization through research and motor octane number measurements coupled with optical imaging techniques, Fuel, Volume 402, 2025, 135976, ISSN 0016-2361, https://doi.org/10.1016/j.fuel.2025.135976.